1-1-2007

Modeling and simulation for a PEM fuel cell with catalyst layers in finite thickness

Jianghui Yin
Ryerson University

MODELING AND SIMULATION FOR A PEM FUEL CELL WITH CATALYST LAYERS IN FINITE THICKNESS

by

Jianghui Yin

B.Eng., Nanjiang University of Aeronautics and Astronautics, Nanjing, China, 1991

A Thesis

presented to Ryerson University

in partially fulfillment of the

requirements for the degree of

Master of Applied Science

in

Mechanical Engineering

Toronto, Ontario, Canada, 2007

I hereby declare that I am the sole author of this thesis.

I authorize Ryerson University to lend this thesis to other institutions or individuals for the purpose of scholarly research.

I further authorize Ryerson University to reproduce this thesis by photocopying or by other means, in total or in part, at the request of other institutions or individuals for the purpose of scholarly research.

Ryerson University requires the signatures of all persons using or photocopying this thesis.

Please sign below, and give address and date.

Modeling and Simulation for a PEM Fuel Cell with Catalyst Layers in Finite Thickness

A thesis for the degree of Master of Applied Science, 2007
by
Jianghui Yin
Department of Mechanical and Industrial Engineering
Ryerson University

Abstract

A detailed non-isothermal computational fluid dynamics (CFD) model for proton electrolyte membrane (PEM) fuel cells is developed in this thesis. This model consists of the equations of continuity, momentum, energy, species concentrations, and electric potentials in different regions of a PEM fuel cell. In particular, the fairly thin catalyst layers of the fuel cell are assigned a finite thickness instead of being treated as nil thickness interfaces in other PEM fuel cell models. Various source/sink terms are presented to associate the conservation equations with the electrochemical reaction kinetics. The water balance in the membrane is modeled by coupling diffusion of water, pressure variation, and the electro-osmotic drag. The membrane swelling effect is explicitly considered the newly derived model, leading to a set of novel water and proton transport equations for a membrane under the partial hydration condition. The electron transport in the catalyst layers, gas diffusion layers and bipolar plates are also described. The PEM fuel cell model developed has been implemented into a commercial CFD software package for simulating various flow and transport phenomena arising in operational PEM fuel cells, analyzing the impact of design and operating parameters on the cell performance, and optimizing the PEM fuel cell design.

Acknowledgements

The computational model presented in this thesis is based mainly on Dr. Jun Cao's previous work. I am very grateful to Dr. Jun Cao for giving me the opportunity to work on such an exciting project and for his constant encouragement and valuable guidance throughout this study.

This work is funded by the National Science and Engineering Research Council of Canada.

Table of Contents

List of Tables

List of Figures

Nomenclature

A_{MEA}	Full active MEA area	m^2
a	Catalyst surface area per unit volume	$m^2 \cdot m^{-3}$ -
C	Electric charge	Coulomb
c	Concentration	$mol \cdot m^{-3}$
c_p	Specific heat capacity at constant pressure	$J \cdot kg^{-1} \cdot K^{-1}$
D	Diffusion coefficient	$m^2 \cdot s^{-1}$
E	Potential	$Volt$
EW_m	Equivalent molecular weight of the membrane	$kg \cdot mol^{-1}$
e	Membrane constant	$mol \cdot m^{-3}$
F	Faraday's constant	96487 $C \cdot mol^{-1}$
f	Swelling coefficient of membrane	-
I	Current	A
i	Current density	$A \cdot m^{-2}$
j_0^{ref}	Exchange current density	$A \cdot m^{-2}$
k	Thermal conductivity	$W \cdot m^{-1} \cdot K^{-1}$
k_ϕ	Electro-kinetic permeability	m^2
k_h	Hydraulic permeability	m^2
k_p	Permeability of electrode/membrane	m^2
M	Molecular weight	$kg \cdot mol^{-1}$
N	Molar flux	$mol \cdot m^{-2} \cdot s^{-1}$
n	Molar number of electrons transferred	-
n_d	Electro-osmotic drag coefficient	-

P	Pressure	Pa
R	Universal gas constant	$8.3145\, J \cdot mol^{-1} \cdot K^{-1}$
RH	Relative humidity	-
S	Mass source/sink	$kg \cdot m^{-3} \cdot s^{-1}$
T	Temperature	K
V	Cell potential (voltage)	$Volt$
$\vec{V}$	Velocity vector	$m \cdot s^{-1}$
W	Power	Watt
x	Molar fraction	$mol \cdot m^{-3}$
x	x axis	m
y	y axis	m
Z	Charge number	-
z	z axis	m

Greek Symbols

α	Transfer coefficient	-
ε	Porosity	-
ε_w^m	Volume fraction of water	-
η	Overpotential	*Volt*
λ	Membrane water content	-
μ	Viscosity	$kg \cdot m^{-1} \cdot s^{-1}$
ρ	Density	$kg \cdot m^{-3}$
ω	Mass fraction	-
ϕ	Electric potential	*Volt*
θ	Volume fraction of membrane in the catalyst layer	-
χ	Cell efficiency	-
σ	Electrical or ionic conductivity	$\Omega^{-1} m^{-1}$

Subscripts/Superscripts

$()_a$	Anode
$()_{act}$	Activation
$()_c$	Cathode
$()_e$	Equilibrium state
$()_f$	Fixed charge
$()_g$	Gas phase
$()_i$	*i). Internal, ii).* species *i;*
$()_{ij}$	Gas pair *i, j* in a mixture
$()_{mem}$	Membrane
$()_l$	Liquid phase
$()_{ohm}$	Ohmic
$()_m$	Membrane phase
$()_{rev}$	Reversible
$()_s$	Solid phase
$()_w$	Water
$()_0$	Reference conditions
$()^{eff}$	Effective value of parameter
$()^{ref}$	Reference value
$()^{sat}$	Saturation state
$()^T$	Thermal
$()^0$	Standard state

Chapter 1. Introduction

1.1. Background

The proton electrolyte membrane (PEM) fuel cell uses a solid polymer membrane as its electrolyte to electrically and mechanically isolate the anode and cathode while allowing for ion migration [1]. The use of a solid polymer electrolyte results in a cell that is able to operate at lower temperatures without causing many reliability issues that occur with liquid electrolytes. PEM fuel cells emit no pollutants and have high power density. The low operating temperature along with quick startup of power generation makes the PEM fuel cell a very attractive power source, especially for transportation applications. In addition, this type of fuel cell has many important advantages, such as high efficiency, simplicity in design, as well as clean and quiet operation.

Among the components of a PEM fuel cell, the polymer membrane is an electronic insulator, but an excellent conductor of hydrogen ions. The membrane, which acts as the electrolyte, is squeezed between the two porous and electrically conductive electrodes, also called gas diffusion layers (GDLs). These two electrodes are typically made of carbon cloth or carbon fiber paper. Between each porous electrode and the polymer membrane is a layer with catalyst particles, typically platinum supported on carbon. The configuration of a cell, along with the basic PEM fuel cell operating principle, is illustrated in Figure 1.1 [2].

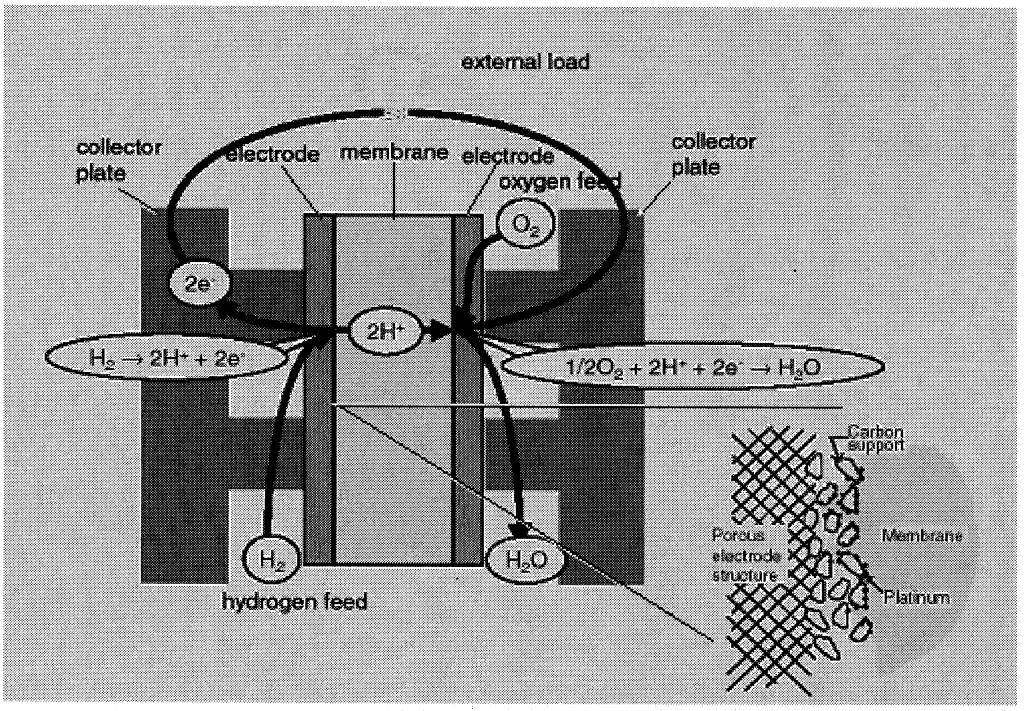

Figure 1.1 The principle of operation of a PEM fuel cell [2]

1.2. Electrochemistry in a PEM Fuel Cell

1.2.1. Electrochemical Reactions

Electrochemical reactions take place simultaneously on the anode and the cathode sides, precisely, on the surfaces of the catalyst layers, which are the interfaces between the gas diffusion layers and the membrane.

At the anode, hydrogen, which is the reactant gas, is fed and diffuses through the porous gas diffusion layer towards the platinum catalyst, where hydrogen molecules split into

protons and electrons:

$$H_2 \rightarrow 2H^+ + 2e^- \tag{1.1}$$

Protons migrate through the membrane, whereas the electrons travel through electrically conductive gas diffusion layers, followed by the current collector plats, towards the outside circuit where they perform useful work and come back to the other side of the membrane.

At the cathode side, oxygen is supplied and diffuses through the diffusion layer towards the catalyst site to react with the protons and electrons, which generates water and heat:

$$O_2 + 4H^+ + 4e^- \rightarrow 2H_2O \ \ (+heat) \tag{1.2}$$

In general, these electrochemical reactions in a PEM fuel cell can be summarized to be the hydrogen oxidation reaction (HOR) in the anode catalyst layer combined with the oxygen reduction reaction (ORR) in the cathode catalyst layer. The desired result of these two simultaneous reactions is the current of electrons through an external circuit.

1.2.2. Electrochemical Cell Potential

The fuel cell electrochemical reactions convert the chemical energy of the reactants into electrical energy directly. The driving force in an electrochemical system is the electrochemical potential, which is comprised of chemical potential and electrostatic potential. For the PEM fuel cell, the theoretical (reversible) cell potential of the hydrogen/oxygen chemical reaction can be obtained from the Nernst equation:

$$E_{rev} = E_0 - \frac{RT}{nF}\ln\left(\frac{a_{H_2O(g)}}{a_{H_2}a_{O_2}^{1/2}}\right) \tag{1.3}$$

where E_0 is the reversible potential in the standard state, R is the gas constant ($8.314 J \cdot mol^{-1} \cdot K^{-1}$), and a_i is the activity coefficients of the products and reactants. Each mole of electrons has a charge of 1 *Faraday* (*1 Faraday*= $96487 Coulombs \cdot mol^{-1}$) and n moles of electrons have the charge in an amount of nF.

1.2.3. Potential Losses in Fuel Cell

The cell potential predicted by the Nernst equation corresponds to an equilibrium (open circuit) state. In practice, the cell potential under operating conditions is significantly lower than the theoretical potential. This suggests that there are some losses in the operational fuel cell as shown through a polarization curve in Figure 1.2.

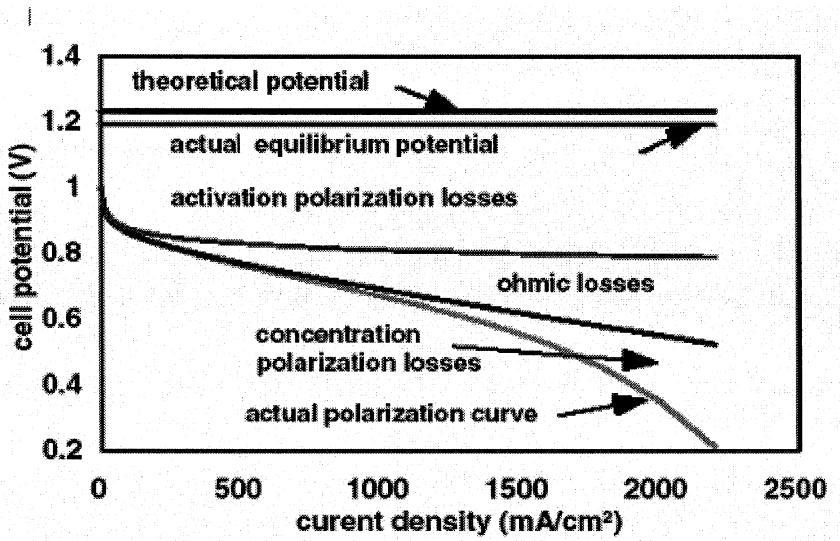

Figure 1.2 Typical polarization curve and predominant loss mechanisms of a PEMFC

When the current starts flowing through the cell, the cell potential drops below the reversible potential due to several typical electrochemical overpotentials, such as activation overpotential, ohimic overpotential, concentration overpotential, along with the internal currents and fuel crossover which arises in the case of open circuit. The details of these potential losses are described below:

1. **Internal current and fuel crossover** occur when the outer circuit is disconnected. Fuel crossover is the amount of fuel that crosses the membrane from the anode to the cathode without being oxidized at the anodic catalyst layer, which results in a loss of fuel. Internal current is the flow of electron from the anode to the cathode through the membrane instead of going through external circuit. The combination of these two losses is typically small compared to other types of losses.
2. **Ohimic overpotential** consisting of two types of ohimic losses occur in fuel cells: (1) the solid-phase potential loss due to electron transport through electrodes, bipolar plates, and collector plates; and (2) the membrane-phase potential loss due to proton transport through the membrane. The magnitudes of these two potential losses depend on the material used in the construction of the fuel cells and the operating conditions of the cell. For instance, the membrane conductivity increases with membrane water content, which helps reduce the membrane-phase potential loss.

3. **Activation overpotential** is caused by the slowness of the reactions taking place on the surfaces of the gas diffusion layers. In the PEM fuel cell, the activation overpotential at the anode is negligible compared to that of the cathode. The activation overpotential depends on factors such as the material property of the electrode, ion-ion interactions, ion-solvent interactions, and characteristics of the electric double layer at the electrode-electrolyte interface.
4. **Mass transport overpotential**, which is also called "concentration overpotential", becomes significant when the fuel cell is operated at high current density. This potential loss is created by the concentration gradient due to the consumption of oxygen or fuel at the gas diffusion layers. The mass transport loss at the anode can be negligible compared at the cathode. At the limiting current density, oxygen at the catalyst layer is depleted and no more current can be increased from the fuel cell, which is reflected in Fig. 1.4 as a sharp decline in cell voltage at high current densities.

1.2.4. Fuel Cell Efficiency

The fuel cell efficiency is defined as the ratio of the electricity produced to the hydrogen consumed:

$$\chi = \frac{W_{el}}{W_{H_2}} \tag{1.4}$$

Electricity produced W_{el} is simply a product between voltage and current:

$$W_{el} = I \cdot V \tag{1.5}$$

where I is the current in Amperes and V is the cell potential in Volts. According to Faraday's law, the hydrogen consumed is directly proportional to the current:

$$\hat{N}_{H_2} = \frac{I}{nF} \tag{1.6}$$

where $\hat{N}_{H_2}$ is in $mol \cdot s^{-1}$.

The energy index W_{H_2} of the hydrogen consumed in Joules per second (Watts) is:

$$W_{H_2} = \Delta H \frac{I}{nF} \tag{1.7}$$

where $\Delta H = 286 kJmol^{-1}$ is the hydrogen's heating value (HV).

By combining Eq. (1.4) through Eq.(1.7), the fuel cell efficiency is simply directly proportional to cell potential:

$$\chi = \frac{V}{1.482} \tag{1.8}$$

1.3. Fuel Cell Components

1.3.1. Polymer Electrolyte Membrane (PEM)

For an operational PEM fuel cell, the desired characteristics are high proton conductivity, good electronic insulation, good separation of the fuel in the anode side from the oxygen in the cathode side, high chemical and thermal stability [3], such that the membrane can efficiently conduct protons while repelling the electrons. Typically, Nafion, made by Dupont, meets most of these requirements and is most commonly used and investigated.

The Nafion membrane is made of poly-perfluoro-sulfonic acids (PSA) ionmer which is essentially a copolymer of hydrophobic tetrafluoroethylene (TFE) and a sulfonyl viny ether with a molecular formula as show in Figure 1.3 [4]. The sulfonyl fluoride group is easily hydrolyzed to form the strongly acidic sulfonic acid ion exchange site.

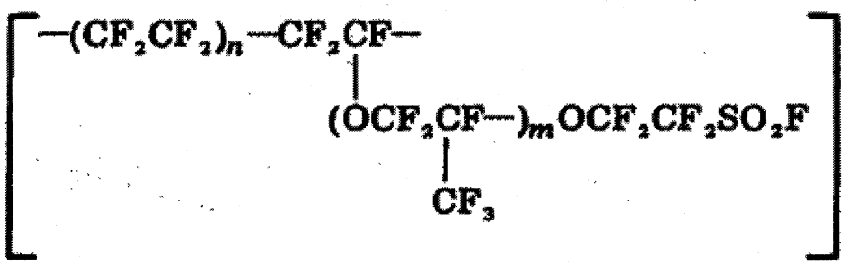

Figure 1.3 Molecular structure of a tetra-fluoro-ethylene and sulfonyl vinyl ether monomer [4]

The proton conductivity of a polymer membrane is strongly dependent on the membrane structure and its water content. In this sense, for optimum fuel cell performance, it is crucial to keep the membrane fully humidified at all times. On the other hand, it should be also noticed that excess water can lead to flooding on the cathode side, which plugs the pores and stops reactants from diffusing towards the reactions sites, thereby starving the fuel cell. Hence, water management schemes are essentially demanded in order for PEM fuel cells to operate properly.

1.3.2. Catalyst Layer (CL)

The electrochemical reactions take place on the catalyst surface, where reactant gases,

electrons, and protons have access. Electrons travel through electrically conductive solids, including the catalyst itself, while protons travel through the membrane only. Therefore the catalyst particles must be electrically connected to the substrates of the electrodes and in intimate contact with the membrane. Also, the catalyst layer must be porous to allow the reactant gases to travel to the reaction sites. At the same time, the product water must be effectively removed; otherwise, the cathode would flood and disconnect the oxygen access.

The most common catalyst used in PEM fuel cells for both oxygen reduction and hydrogen oxidation reactions is platinum. Since the catalytic activity occurs on the surface of the platinum particles, it is desirable to maximize the surface area of the platinum particles. A common procedure for surface maximization is to deposit the platinum particles on larger carbon black particles [5]. The optimum thickness of the catalyst layer is found to be around $10\,\mu m$ since it was observed in [6] that almost all of the reactions occur within a $10\,\mu m$ thick layer. Such a combination of a membrane sandwiched between two catalyzed porous electrodes is called a membrane electrode assembly (MEA).

1.3.3. Gas Diffusion Layer (GDL)

The gas diffusion layer (GDL) is made of carbon fiber-based porous materials such as carbon fiber papers, woven carbon fabrics or cloths, with typical thicknesses of 100 -300 μm [7]. Although it does not directly participate in the electrochemical reactions, a gas diffusion layer in PEM fuel cells has several important functions:

- to provide a mechanical support to the MEA;
- to provide a porous pathway for reactant gases to reach the catalyst layer and transport water to or from the catalyst layer via the momentum transport as well as the concentration and pressure gradients;
- to conduct electrons between the catalyst layers and the current collector plates to complete the electrical circuit;
- to remove the heat generated during electrochemical reactions.

1.3.4. Bipolar Plate (BP)

The bipolar plates (BPs) employed in the PEM fuel cell stack occupy about 80% of the total weight and account for 45% of the stack cost [8]. They are designed to accomplish many functions, such as distributing reactant gases uniformly over the active areas, removing heat from the active areas, carrying current from cell to cell, and preventing leakage of reactant gases and coolant. Desirable material of bipolar current plates must be electrically conductive, impermeable to gases, thermally well conductive, highly corrosion resistant, and easy to manufacture. In general, two families of materials have been used for fuel cell bipolar plates, namely graphite-composite and metallic [8].

1.4. PEM Fuel Cell Modeling Literature Review

During the PEMFC operation, critical properties, such as the fluid flow pattern, species

concentration variation, temperature distribution, and local current densities, are often fairly difficult to achieve by *in-situ* measurements. Fortunately, the development of digital computers enables fuel cell researchers to investigate, through numerical solution of mathematical modeling equations, sophisticated flow features and complex transport mechanisms that might be experimentally unobservable. Research efforts through modeling and simulation may greatly help obtain insight for the PEMFC design and performance optimization.

In the early 1990s, the most prominent earlier work presented by Barnardi and Verbrugge [10,11] developed a one-dimensional isothermal PEM fuel cell model for water management assuming a constant for water content in the membrane. On the other hand, Springer et al. [12] presented empirical relations for such parameters as water diffusion coefficient, electro-osmotic drag coefficient, water adsorption isotherms, and membrane conductivities, etc. These one-dimensional models provided good fundamental bases for further PEM fuel cell modeling but cannot take into account the effects of reactants consumption and products generation.

Fuller and Newman [13], Nguyen and White [14] developed pseudo-two-dimensional models, which assumed diffusion is the only mechanism for oxygen transport and did not consider the interaction of the flow with the species field in the gas channel and GDLs. Instead, they prescribed concentration boundary conditions either at the gas channel/GDL interfaces, or at the catalyst layer/GDL interfaces. As extension, the subsequent model of Yi

and Nguyen [15, 16] included the convective water transport across the membrane by a pressure gradient, the temperature distribution in the solid phase along the injected flow direction, and the heat removal by natural convection. By using a mechanistic approach, a thermal model for the Ballard Mark IV PEM fuel cell stack was developed by Amphlett et al. [17], and a number of parameters were identified to fit the empirical data measured from a single Ballard Mark IV cell. This thermal model was coupled to a previously developed electrochemical model that relates the power produced by the stack and the stack temperature to the amount of heat removed from the stack. Similarly, Kim et al. [18] presented an empirical equation to describe the PEM fuel cell performance data over a complete operating range. The inclusion of an exponential term with an adjustable coefficient in their empirical equation was found to better approach the performance curves and meanwhile reflect the mass transport limited region at high current densities.

Because the flow in the gas channel has a great influence on the gas transport in the GDLs, it is inevitable to consider the convection effects in the PEMFC modeling. Gurau et al [19] developed the first complex PEMFC model in which a *Computational Fluid Dynamics* (CFD) framework is involved to obtain the solution. In their two-dimensional steady-state model, the standard momentum, energy transport, continuity, and species concentration equations were solved in the anode/cathode gas channels and the MEA, while the porous medium model was used for equations describing transport phenomena in the porous components. This unified approach eliminated the need of prescribing artificial boundary

conditions at the various interfaces between the different components of a fuel cell. They found a nonlinear oxygen distribution along the gas channel direction, which is different from the linear assumption previously employed in pseudo-two-dimensional models [13]. A similar CFD model was proposed by Um et al. [20], which paid special attention to the jump oxygen condition at the GDL/catalyst layer interface by using the Henry's law to account for the difference of oxygen concentration between the liquid and gas phases. Wang et al. [21] studied the distribution of both single-phase and two-phase water within the cathode in a PEM fuel cell using air as oxidant, and presented some interesting two-phase flow and transport results, but did not include the influence of the catalyst layer.

To account for the heat management issue, Berning et al. [22] developed a comprehensive, single-phase, non-isothermal, three-dimensional computational model, which accounts for many important transport phenomena in a complete assembly of gas channels, porous GDLs, and thin catalyst layers. In their model the catalyst layer was treated as a surface without thickness. The same assumption had been made in the modeling approach presented by Dutta et al. [23,24], who obtained results by adding the necessary sources and correction terms to the governing equations within the framework of commercial CFD codes. As such, water transport and ohmic potential drop across MEA were treated using simplified linear relationships as in the early work of Nguyen and White [14]. Um and Wang [25] presented a 3D computational fuel cell dynamics model to elucidate the interactions between mass transport and electrochemical kinetics in PEM fuel cells with both

straight and interdigitated flow field designs.

With a finite thickness of catalyst layer taken into account, a general three-dimensional CFD model is presented by Zhou and Liu [26] using the commercial CFD package CFX. In this model, electrochemical reactions, including hydrogen oxidation reaction in the anode catalyst layer and oxygen reduction reaction in the cathode catalyst layer, are taken into account by adding proper sources/sink terms in the governing equations, while liquid water transport within the membrane was not investigated. In most PEM fuel cell models, the electrical resistance of the GDL is neglected under the assumptions of a sufficiently large electrical conductivity; consequently, a uniform electronic-phase potential distribution in the GDL. Recently, this research group expanded the model by considering the electronic resistance of the GDL and obtained a non-uniform distribution of overpotential in the GDL [27], which differs from the results using the earlier CFD models [25, 26]. In 2005, Cao et al [28] developed a partially hydrated membrane model for PEM fuel cells that featured the inclusion of the membrane swelling effects and provided a physically realistic description of water transport in the membrane.

The aforementioned representative literature clearly revealed that heat management and water management are two key processes in achieving the required performance and lifetime of PEM fuel cell operation. Unfortunately, the majority of the available models concentrated mainly on one aspect related to the two interrelated managements, which more or less constrained their applicability to parametric studies for the real-world PEM fuel cell design

and performance optimization. On the other hand, the main bottleneck faced by the fuel cell modeling community is that some coefficients and relationships required by the models are hard to theoretically characterize or experimentally measure. Consequently, today's models are more or less of empirical nature and involve the aid of some evidently unrealistic assumptions. A typical assumption widely made in available PEM fuel cell models is that the catalyst layers are of nil thickness so that they can be simplified to play only the role of interface between the membrane and the electrodes, for which the realistic effects of the two key electrochemical reactions in an operational PEM fuel cell get more or less veiled. In order to provide the fuel cell models with a more realistic and reliable basis, all the physical and electrochemical processes occurring in an operational PEM fuel cell should be incorporated into a complete non-isothermal model that consists of all components including two catalyst layers with finite thickness and a membrane under partial hydration condition.

1.5. Thesis Goal

The purpose of this work is to develop a comprehensive non-isothermal CFD model of PEM fuel cells, which is capable of investigating electrochemical and transport phenomena in all seven regions of a PEMFC, namely, the anode/cathode gas channels, two GDLs, two catalyst layers in finite thickness, and a membrane allowing for partial hydration. This model is implemented into the finite element CFD commercial software package FEMLAB®, which provides a platform for simulating all important transport phenomena and

electrochemical kinetics through solving the balance equations for transport processes involving the mixture gas flow, multi-component transport, heat transfer, water content, proton, and electron transport, to gain valuable insight and guidance for identifying the PEM fuel cell's possible failure mechanisms and achieving its performance optimization.

The outline of this thesis is as follows: Chapter 2 systematically presents a complete PEM fuel cell non-isothermal model. Chapter 3 is devoted to validate the model against the experimental data, present base case results, and perform a detailed parametric study along the flow channel direction. On the other hand, Chapter 4 focuses on the numerical simulation of the cross section of a PEM fuel cell to investigate the cell performances corresponding to the conventional straight flow channel design and the interdigitated flow field design, respectively. Finally, some concluding and outlooking remarks on this modeling study are made in Chapter 5.

Chapter 2. Two-Dimensional Model of PEM Fuel Cell

A single PEM fuel cell to be modeled, as schematically shown in Figure 2.1, is computationally considered as a configuration consisting of seven subregions (from the bottom to the top on Figure 2.1): the gas channel, gas diffusion layer (GDL) and catalyst layer (CL) on the anode side; the ionomeric membrane; and the catalyst layer, gas diffusion layer and gas channel on the cathode side.

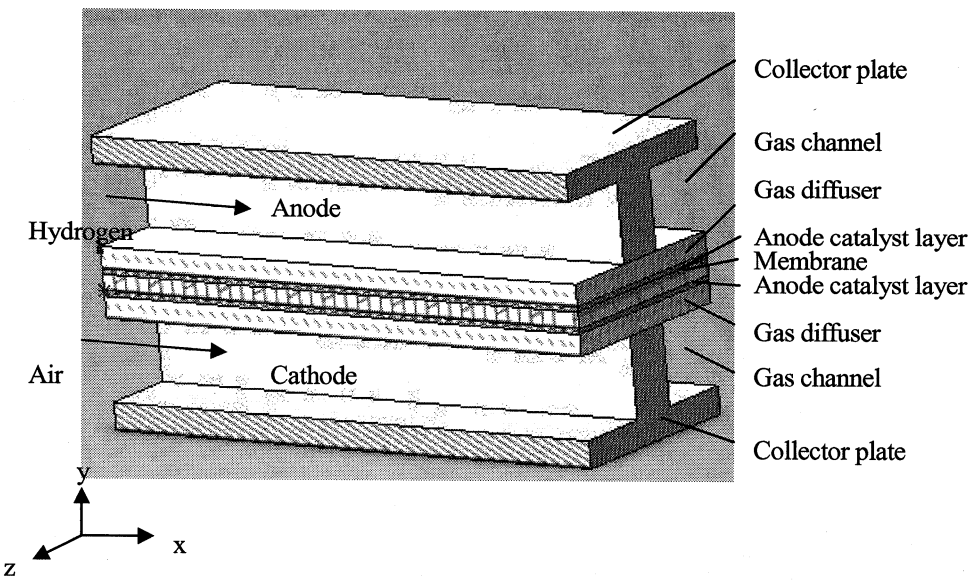

Figure 2.1 Sketch of a PEM fuel cell configuration

In the current model, the anodic channel is supplied by hydrogen (H_2), water vapor ($H_2O_{(g)}$) and carbon dioxide (CO_2), whereas humidified air consisting of oxygen (O_2),

nitrogen (N_2), and water vapor ($H_2O_{(g)}$) is fed into the cathodic channel. The hydrogen oxidation and oxygen reduction reactions are considered to occur only within the active catalyst layers on the anode and cathode sides, respectively.

2.1. Assumptions

The model presented here is established with the following assumptions:

1. the fuel cell operates under steady-state conditions;
2. the gas mixture is incompressible and obeys the ideal gas law;
3. the flow remains laminar everywhere due to low Reynolds number;
4. the gravity effect is negligible;
5. ohmic heating in electrodes is neglected due to their high conductivity;
6. though heat generation due to the electrochemical reaction is considered, the fluid properties are assumed to be independent of temperature;
7. on the anode side, the gas mixture consists of H_2, $H_2O_{(g)}$ and CO_2 (due to incomplete purification of the hydrogen product), while on the cathode side the humidified air consists of O_2, N_2 and $H_2O_{(g)}$;
8. the gas diffusers, the catalyst layers, and the membrane are all considered as isotropic and homogeneous porous media;
9. the membrane is assumed to be impermeable for the gas-phase, for which a fairly small permeability for gases is employed to ensure nil gas concentration in the membrane;

10. within the gas channels, the gas diffusers, and the catalyst layers, water is purely in the form of vapor or over-saturated vapor, while water in the membrane is in the liquid phase only and exhibits a linear variation in its pressure;
11. no water phase change is taken into account within each component except that all water vapor at each interface between the catalyst layer and the membrane is entirely transformed to liquid water.

2.2. Modeling Equations in Gas Channels

In the gas channels, the multi-species transport processes in conjunction with heat transfer can be described using the mixture continuity equation, the Navier-Stokes equations, the energy equations, and the Maxwell-Stefan equations.

2.2.1. Continuity and Momentum Equations

For the gas mixture in the channels, the Navier-Stokes equations are employed to describe the conservation of the mass and momentum

- continuity equation:

$$\vec{\nabla} \cdot \rho \vec{V} = 0 \tag{2.1}$$

- momentum equation:

$$\rho(\vec{V} \cdot \nabla)\vec{V} = -\vec{\nabla} p + \mu \Delta \vec{V} \tag{2.2}$$

where μ, ρ, $\vec{V}$ and p are the dynamic viscosity, density, velocity, and pressure of the gas mixture, respectively. Here, it is noted that the density is assumed to be a constant for the gas mixture since the incompressibility condition is taken into account.

2.2.2. Thermal Model

The thermal model used for the gas channels involves heat conduction and convection only; no additional heat source or sink term is considered since physically no heat is generated or adsorbed in the channels. Hence, the heat transfer equation reads:

$$\rho c_p(\vec{V}\cdot\vec{\nabla}T) = k\Delta T \tag{2.3}$$

where c_p is heat capacity at constant pressure, k the thermal conductivity.

2.2.3. Mass Transport Equations

For multi-gaseous-component diffusion at low density, the Maxwell-Stefan is shown to be a good approximation [32]:

$$\vec{\nabla}x_i = -\sum_{j=1}^{n}\frac{1}{cD_{ij}}(x_j\vec{N}_i - x_i\vec{N}_j),\quad i,j=1,2,3\quad i\neq j \tag{2.4}$$

where the subscripts i and j denote hydrogen (H_2), water vapor ($H_2O_{(g)}$), carbon dioxide (CO_2) on the anode side and oxygen (O_2), water vapor ($H_2O_{(g)}$), nitrogen (N_2) on the cathode side, c represents the concentration, x_i is the mole fraction of the component i, N_i the molar flux of the component i, and D_{ij} is the binary diffusivity of species i and j. Note that here a ternary mixture is dealt with on both cathode and anode sides,

therefore, the three species are practically viewed as existing in three species pairs: O_2 - N_2, N_2 - $H_2O_{(g)}$, and O_2 - $H_2O_{(g)}$ on the cathode side; H_2 - CO_2, CO_2 - $H_2O_{(g)}$, and $H_2O_{(g)}$ - H_2 on the anode side. In practice, the experimentally obtained binary diffusivities, D_{ij}^0, at atmosphere pressure p_{atm} and reference temperature T_0 shown in Table 2.3 will be scaled to the operating temperature and pressure according to [22]:

$$D_{ij} = D_{ij}^0(T_0, p_0)\frac{p_0}{p}\left(\frac{T}{T_0}\right)^{1.5} \tag{2.5}$$

Ultimately, the mass balance for each species in the ternary system obeys the following equation:

$$\vec{\nabla}\cdot\left[-\rho\omega_i\sum_{j=1}^{n}D_{ij}\vec{\nabla}x_j + (x_j-\omega_j)\frac{\vec{\nabla}p}{p}\right] = -\rho\vec{V}\cdot\vec{\nabla}\omega_i \tag{2.6}$$

where the molar fraction x_i can be related to the mass fraction ω_i by [28]:

$$x_i = \frac{\dfrac{\omega_i}{M_i}}{\displaystyle\sum_{j=1}^{n}\frac{\omega_j}{M_j}} \tag{2.7}$$

Eq.(2.8) can also be inverted to:

$$\omega_i = \frac{x_iM_i}{\displaystyle\sum_{j=1}^{n}x_jM_j} = \frac{x_iM_i}{M} \tag{2.9}$$

where M represents the total mole mass of the mixture:, it is a function of molar fraction x_i:

$$M = \sum_{i=1}^{n}M_ix_i \tag{2.10}$$

with M_i denoting the mole mass of the species i. The gas mixture density ρ is calculated

using the ideal gas law:

$$\rho = M\frac{p}{RT} \tag{2.11}$$

Eq. (2.6) can be theoretically applied to each species in the gas mixture. In practice, the mass and molar fractions for CO_2 on the anode side and N_2 on the cathode side are calculated using:

$$\omega_n = 1 - \sum_{i=1}^{n-1} \omega_i \tag{2.12}$$

$$x_n = 1 - \sum_{i=1}^{n-1} x_i \tag{2.13}$$

which ensure the conservation of mass on both sides.

2.3. Modeling Equations in Gas Diffusion Layers

2.3.1. Momentum Equation

In the gas diffusion electrodes, Darcy's law can be used to model the flow in such porous media with the pressure gradient as the driving force. Meanwhile, it is also important to note that the average viscous stress terms have to be taken into account in certain outer boundary of a porous medium where the macroscopic velocity varies rapidly in space [33]. In the PEM fuel cell case, for the boundary of the GDL (electrode) that is adhere to the gas channel, a thin layer of the order of the pore scale is formed where the velocity drops very fast. Darcy's law is not applicable in this layer unless some ad hoc boundary conditions are employed to connect the flow field in the channel described by the Navier-Stokes equations

to the flow in the porous medium described by Darcy's law. To avoid using such case-dependent boundary conditions, the Navier-Stokes equations are solved over the entire gas diffusion layer. Taking the porosity into account, the Navier-Stokes equations are revised to:

The continuity and momentum equations are

$$\vec{\nabla} \cdot \rho \vec{V} = 0 \tag{2.14}$$

and

$$\rho(\vec{V} \cdot \vec{\nabla})\vec{V} = -\vec{\nabla} p + r^{(2)} \mu \Delta \vec{V} - \frac{\varepsilon_g \mu}{k_p} \vec{V} \tag{2.15}$$

in which the last term is standing for the average drag force exerted by the fluid on the solid surface per unit volume of medium, k_p the permeability of the gas mixtures in the porous medium (graphite), and ε_g the porosity of the gas diffusers. Note that $r^{(2)}$ is a coefficient describing the effect of the porosity of the medium to the viscous force. When $r^{(2)} = 1$, Eq. (2.15) turns into the Brinkman's equations. Dagan [33] showed $r^{(2)}$ can be estimated using:

$$r^{(2)} = 2.25 \frac{(1-\varepsilon_g)^2}{\varepsilon_g{}^2} \tag{2.16}$$

2.3.2. Mass Transport Equations

Due to the porous nature of the gas diffusers, the binary diffusivities correction is taken for the porous media, and the species equations become:

$$\vec{\nabla}\cdot\left[-\rho\omega_i\sum_{j=1}^{n}D_{ij}^{eff}\vec{\nabla}x_j+(x_j-\omega_j)\frac{\vec{\nabla}p}{p}\right]=-\rho\vec{V}\cdot\vec{\nabla}\omega_i \tag{2.17}$$

where the binary diffusivities D_{ij} are corrected to account for the porosity using the so-called *Bruggemann* correction [10]:

$$D_{ij}^{eff}=D_{ij}\varepsilon_g^{1.5} \tag{2.18}$$

2.3.3. Energy equation

The energy equation for the gas diffusers can be obtained by ensemble averaging of the microscopic energy equations in both fluid and solid phases. The effective conductivity is a function of the fluid phase and solid matrix conductivities, which is given by:

$$k_{eff}=-2k_{gr}+\frac{1}{\frac{\varepsilon_g}{2k_{gr}+k_{gas}}+\frac{1-\varepsilon_g}{3k_{gr}}} \tag{2.19}$$

where k_{gr} and k_{gas} are the thermal conductivities of the graphite solid matrix and of the gas mixture, respectively. Also, unlike in the gas channel, in the gas diffusers there exists electron current. Therefore, the energy equation for the gas diffusers becomes:

$$\rho c_p(\vec{V}\cdot\vec{\nabla}T)=k_{eff}\Delta T+\frac{i_e^{\,2}}{\sigma_{GDL}^{e}} \tag{2.20}$$

with the last term representing the heat source term generated due to the ohmic heating of electron current i_e.

2.3.4. Solid-Phase Potential Equations

The GDL functions also to provide electron lateral conduction, serving as a bridge between the catalyst layer and the current-collecting land. Since no electron is produced in the GDL, the electron current density i_e in the gas diffusers satisfies:

$$\vec{\nabla} \cdot \vec{i}_e = 0 \tag{2.21}$$

The electron current density i_e is defined as:

$$\vec{i}_e = -\sigma^e_{GDL} \vec{\nabla} \phi_s \tag{2.22}$$

where σ^e_{GDL} is the electrical conductivity of the gas diffuser. Finally, the solid-phase potential satisfies:

$$\vec{\nabla} \cdot (-\sigma^e_{GDL} \vec{\nabla} \phi_s) = 0 \tag{2.23}$$

2.4. Modeling Equations in Catalyst layers

2.4.1. Flow Model: the Darcy's law

The catalyst layers are also porous media. Since the components neighboring the catalyst are the porous electrode and membrane, no steep velocity change might take place at the interfaces within the MEA. Therefore, Darcy's law can be applied to model the flow in the porous catalysts with the pressure gradient as the sole driving force.

Darcy's law states that the velocity vector is determined by the pressure gradient, $\vec{\nabla} p$, the fluid viscosity, μ, and the structure of the porous media, resulting in the following

equation:

$$\vec{V} = -\frac{k_h}{r^{(2)}\mu}\vec{\nabla}p \tag{2.24}$$

where $r^{(2)}$ in the catalyst layer appears in the same form as in Eq. (2.16),

$$r^{(2)} = 2.25\frac{(1-\varepsilon_{ct})^2}{\varepsilon_{ct}^{\ 2}} \tag{2.25}$$

but here the effective porosity of the catalyst layer ε_{ct} is calculated by

$$\varepsilon_{ct} = \varepsilon_m \cdot \theta_{mc} \tag{2.26}$$

with ε_m and θ_{mc} denoting the porosity of the membrane and the volume fraction of membrane in the catalyst layer, respectively.

2.4.2. Electrochemical Modeling Equations

In the catalyst layers, the electrochemical reactions can be modeled by the Butler-Volmer equations [19]:

$$j_a = (aj_0^{ref})_a\left(\frac{c_{H_2}}{c_{H_2,ref}}\right)^{1/2}\left[\exp\left(\frac{\alpha_a^a F}{RT}\eta_a\right) - \exp\left(-\frac{\alpha_c^e F}{RT}\eta_a\right)\right] \tag{2.27}$$

$$j_c = (aj_0^{ref})_c\left(\frac{c_{O_2}}{c_{O_2,ref}}\right)\left[\exp\left(\frac{\alpha_a^c F}{RT}\eta_c\right) - \exp\left(-\frac{\alpha_c^c F}{RT}\eta_c\right)\right] \tag{2.28}$$

where j_a and j_c are the exchange current densities of the anode and cathode, respectively; a the catalyst surface area per unit volume; j_0^{ref} the reference exchange current densities; c_{H_2} and c_{O_2} the hydrogen and oxygen concentrations, respectively; $c_{H_2,ref}$ and $c_{H_2,ref}$ the corresponding reference concentrations, respectively; η_a and η_c the activation

overpotentials at the anode and cathode, respectively; α_a^a and α_a^c the anodic transfer coefficients at the anode and cathode, respectively; α_c^a and α_c^c the cathodic transfer coefficients at the anode and cathode, respectively; and F Faraday's constant.

The kinetic expressions in Eqs. (2.27) and (2.28) represent the hydrogen oxidation reaction (HOR) in the anode catalyst layer and oxygen reduction reaction (ORR) in the cathode catalyst layer, respectively.

The surface overpotential for an electrochemical reaction, η, representing the driving force for an electrochemical reaction, is defined as:

$$\begin{cases} \eta_a = \phi_s - \phi_p & at \quad anode \\ \eta_c = \phi_s - \phi_p - E_0 & at \quad cathode \end{cases} \tag{2.29}$$

where ϕ_s and ϕ_p are the solid-phase and membrane-phase potential, respectively. The last term E_0 is the thermodynamic open circuit potential for overall reaction, which is, in turn, a function of the reactant and product concentrations at the interface as generally expressed by the Nernst equation as [19]:

$$E_0 = 1.23 - 0.9\times10^{-3}(T-298) + 2.3\frac{RT}{4F}\log(p_{H_2}^2 p_{O_2}) \tag{2.30}$$

As alternative, in [1] the empirical results are tabulated for the open circuit potential, which are fitted into a linear function of temperature:

$$E_0 = 0.0025T + 0.2329 \tag{2.31}$$

2.4.3. Mass Transport Equations

Taking into account the exchange current densities over both anodic and cathodic

catalyst layers, the mass transport equation used in the catalyst layers becomes:

$$\vec{\nabla}\cdot\left[-\rho\omega_i\sum_{j=1}^{n}D_{ij}^{eff}\vec{\nabla}x_j+(x_j-\omega_j)\frac{\vec{\nabla}p}{p}\right]=-\rho\vec{V}\cdot\vec{\nabla}\omega_i+S_k \tag{2.32}$$

where S_k is the source/sink term for species k.

The overall reaction in the catalyst layer of a PEM fuel cell, as shown in Eqs.(1.1) and (1.2), indicates that, in order to produce one electron with the charge of one Coulomb, ½ mole of hydrogen from the anode side and ¼ mole oxygen from the cathode side are needed, and ½ mole of water will be produced at the cathode side. Therefore, at the anode side, hydrogen is oxidized with local sink terms for hydrogen and water:

$$S_{H_2}=-\frac{j_a}{2F}M_{H_2} \tag{2.33}$$

$$S_{H_2O}=0 \tag{2.34}$$

where M_{H_2} is the molecular weight of hydrogen, and Eq. (2.34) shows no water is produced or depleted in the anodic catalyst layer; on the other hand, the mass generation source terms at the cathode side are described as:

$$S_{O_2}=\frac{j_c}{4F}M_{O_2} \tag{2.35}$$

$$S_{H_2O}=-\frac{j_c}{2F}M_{H_2O} \tag{2.36}$$

where M_{O_2} and M_{H_2O} are the molecular weights of oxygen and water, respectively. Normally, according to Eqs. (2.27) and (2.28), j_a is positive while j_c is negative.

2.4.4. Energy Equations

The electrochemical reactions shown in Eqs.(1.1) and (1.2) take place simultaneously on

the two catalyst layers, leading to migration of the electrons and protons through the layers. Accordingly, the energy equation can be expressed as:

$$\rho c_p(\vec{V}\cdot\vec{\nabla}T) = k_{ct,eff}\Delta T + \frac{i_p^2}{\sigma_{ct}^m} + \frac{i_e^{\,2}}{\sigma_{ct}^e} + \begin{cases} \eta_a \cdot j_a & at \quad anode \\ \eta_c \cdot j_c & at \quad cathode \end{cases} \tag{2.37}$$

where i_e and i_p are electron and proton current density, respectively, while σ_{ct}^m and σ_{ct}^e are proton and electronic conductivity within catalyst layers, respectively. On the right hand side of Eq.(2.37), the last term represents the heat generation or absorption due to electrochemical reaction at the catalyst; the second and third terms describe the ohmic heating of both electron current i_e and proton current i_p within catalyst layers.

2.4.5. Solid-phase and membrane-phase potential equations

In the anodic catalyst layer, hydrogen is consumed to produce protons and electrons. Electrons pass through an external circuit to the cathode, thus providing electrical power, while the protons transport through the membrane to the cathode. In the cathodic catalyst layer, oxygen combines with protons and electrons to produce water. The transportation paths for protons and electrons form a closed electrical circuit as shown in Figure 2.2.

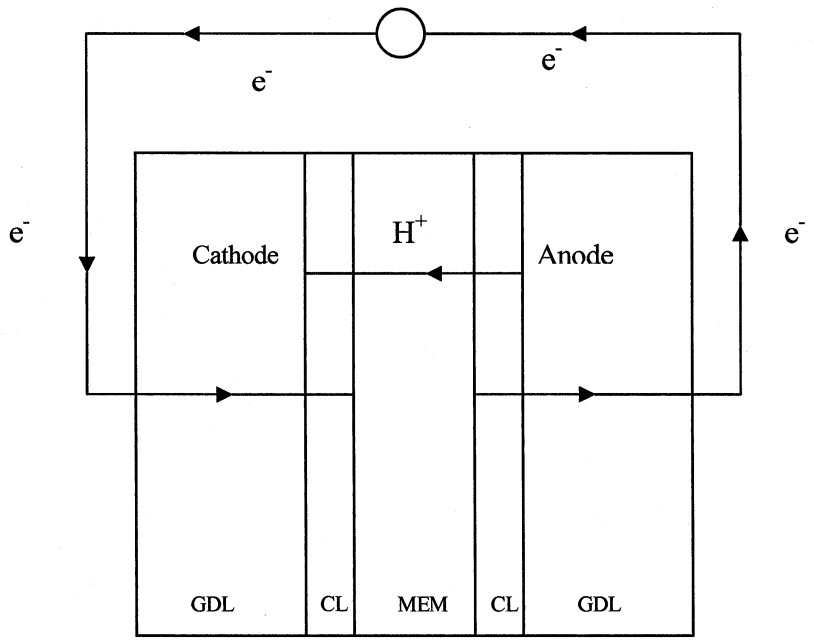

Figure 2.2 Transport paths of protons and electrons within a PEM fuel cell

In the two catalyst layers, the proton current density i_p and the electron current density i_e satisfy:

$$\vec{\nabla} \cdot \vec{i}_p = \begin{cases} j_a & at \quad anode \\ j_c & at \quad cathode \end{cases} \tag{2.38}$$

$$\vec{\nabla} \cdot \vec{i}_e = \begin{cases} -j_a & at \quad anode \\ -j_c & at \quad cathode \end{cases} \tag{2.39}$$

Overall, the current density conservation law follows:

$$\vec{\nabla} \cdot \vec{i}_p + \vec{\nabla} \cdot \vec{i}_e = 0 \tag{2.40}$$

which implies:

$$\vec{i}_p + \vec{i}_e = \text{constant} \tag{2.41}$$

On the other hand, the membrane-phase potential ϕ_p and the proton current density i_p are interrelated by:

$$\vec{i}_p = -\sigma_{ct}^p \vec{\nabla} \cdot \phi_p \tag{2.42}$$

Thus, the membrane-phase potential satisfies:

$$\vec{\nabla} \cdot (-\sigma_{ct}^p \vec{\nabla} \phi_p) = \begin{cases} j_a & at \quad anode \\ j_c & at \quad cathode \end{cases} \tag{2.43}$$

Similarly, the solid-phase potential ϕ_s satisfy:

$$\vec{\nabla} \cdot (-\sigma_{ct}^e \vec{\nabla} \phi_s) = \begin{cases} -j_a & at \quad anode \\ -j_c & at \quad cathode \end{cases} \tag{2.44}$$

where σ_{ct}^p and σ_{ct}^e are the ionic and electrical conductivity of the catalyst layers, respectively.

2.5. Modeling Equations in Membrane

Within the membrane, water is assumed to be present purely in the liquid phase while the reactant gases are considered impermeable. Properties of interests in the membrane are the liquid water flux, the electrical potential distribution, and temperature distribution, which have effects on the ionic conductivity.

2.5.1. Darcy's Law and Energy Equations

The water transport in the porous membrane for liquid water can be described using the Darcy's law again:

$$\vec{V} = -\frac{k_h}{r^{(2)}\mu_l}\vec{\nabla}p_l \tag{2.45}$$

where μ_l is the liquid water viscosity, p_l the pressure for liquid water, k_h the hydraulic permeability of the membrane, and $r^{(2)}$ has the similar expression in Eq. (2.16) but uses ε_m instead of ε_g. The energy equation in the membrane is similar to Eq. (2.20) except that an additional Joule heating source term is added:

$$\rho c_p(\vec{V}\cdot\vec{\nabla}T) = k_{m,eff}\Delta T + \frac{i_p^{\,2}}{\sigma_m^p} \tag{2.46}$$

where σ_m^p appearing in the Joule heating source term represents the ionic conductivity in the membrane; the effective thermal conductivity in the membrane $k_{m,eff}$ given by:

$$k_{m,eff} = -2k_{m,dry} + \frac{1}{\dfrac{\varepsilon_m}{2k_{m,dry}+k_{w,l}} + \dfrac{1-\varepsilon_m}{3k_{m,dry}}} \tag{2.47}$$

where ε_m is the membrane porosity, $k_{m,dry}$ the thermal conductivity of dry membrane, $k_{w,l}$ the thermal conductivity of liquid water.

2.5.2. Water and Proton Transport Model

Two water and proton transport models are compared in this study: one particularly examines the effect of membrane swelling on water content and potential loss within the membrane; the other considers the membrane swelling effects negligible.

2.5.2.1 Model (A): Membrane Swelling Effect Switched on

The permeability of the membrane to hydrogen, oxygen, nitrogen and carbon dioxide are low and can be neglected as in assumption 9. Thus, only water and protons are transported in the membrane, and each obeys the principle of mass conservation.

Although the exact and complete mechanism of water transport behavior in the membrane is still under investigation, an updated model is formulated here to allow quantitative assessment of fuel cell operation with a membrane under the partial hydration condition. Liquid water and protons are considered as the only two mobile species in the membrane. Each of these two species should obey the mass conservation principle, i.e.

$$\vec{\nabla} \cdot \vec{N}_w = 0 \tag{2.48}$$

and

$$\vec{\nabla} \cdot \vec{N}_p = 0 \tag{2.49}$$

where $\vec{N}_w$ and $\vec{N}_p$ are the molar flux of water and that of protons, respectively. As sign conventions, positive values for $\vec{N}_w$ or $\vec{N}_p$ mean net water flux or protons flux from the anode to the cathode and negative values are from the cathode to the anode.

2.5.2.1.1 Water Transport

The molar flux of water is generated by the water diffusion, pressure gradient, and electro-osmotic drag, i.e.:

$$\vec{N}_w = -D_w \vec{\nabla} c_w - c_w \varepsilon_m^w \frac{k_h}{\mu_l} \vec{\nabla} p_l + \frac{n_d \vec{i}_p}{F} \tag{2.50}$$

where c_w denotes the molar concentration of water, D_w the diffusion coefficient, ε_w^m the volume fraction of water in the membrane, k_h the hydraulic permeability of the membrane, μ_l the liquid water viscosity, p_l the water pressure, n_d the elector-osmotic drag coefficient, F the Faraday's constant, and $\vec{i}$ is the local current density in the membrane which is equal to proton current density, $\vec{i}_p$, since there is no electron transport in the membrane. In contrast with other models published in the open literature [21,23], this equation accounts for back diffusion processes induced by the water concentration gradient, which provides the model with improved capability of predicting humidification schemes.

Taking into account the current density conservation:

$$\vec{\nabla} \cdot \vec{i} = 0 \tag{2.51}$$

and the linear profile of pressure:

$$\nabla^2 p_l = 0 \tag{2.52}$$

the divergence of $\vec{N}_w$ can be expressed as:

$$\vec{\nabla} \cdot \vec{N}_w = -D_w \nabla^2 c_w - \varepsilon_w^m \frac{k_h}{\mu_l} (\vec{\nabla} c_w \cdot \vec{\nabla} p_l) + \frac{\vec{\nabla} n_d \cdot \vec{i}}{F} \tag{2.53}$$

Combination of Eq. (2.48) and Eq. (2.54) leads to:

$$-D_w \nabla^2 c_w - \varepsilon_w^m \frac{k_h}{\mu_l} (\vec{\nabla} c_w \cdot \vec{\nabla} p_l) + \frac{\vec{\nabla} n_d \cdot \vec{i}}{F} = 0 \tag{2.55}$$

The electro-osmotic drag coefficient, n_d, can be determined by the work of Springer et al.[12] which proposed a simple linear relationship between this coefficient and membrane water content based on their experiments using Nafion117:

$$n_d = \frac{2.5}{22}\lambda \tag{2.56}$$

where λ is the hydration index, which is defined as the number of moles of water per equivalent sulfonic acid group, SO_3^-, in the membrane; the numeric values 2.5 and 22 correspond to the number of water molecules dragged per migrating H^+ ion and the possible maximum hydration index, respectively.

To account for membrane swelling, dry membrane thickness dimensions are expanded by the factor $(1+f\lambda)$. [12] also presented an empirical formula relating c_w to λ as follows:

$$c_w = \frac{e\lambda}{f\lambda+1} \tag{2.57}$$

where f is the membrane swelling coefficient experimentally determined through the measured thicknesses of the dry and fully hydrated Nafion 117 membranes, and e is a constant ratio for Nafion 117 expressed as:

$$e = \frac{\rho_m^{dry}}{EW_m} \tag{2.58}$$

with the dry membrane density, ρ_m^{dry}, and the equivalent molecular weight of the membrane, EW_m.

The membrane water diffusivity is related to the temperature and water content of the membrane. Its formula of empirical nature reads [12]:

$$D_w = 10^{-6}\exp\left[2416\left(\frac{1}{303}-\frac{1}{T}\right)\right](2.563-0.33\lambda+0.0264\lambda^2-0.000671\lambda^3) \tag{2.59}$$

After re-arranging Eq. (2.57) to:

$$\lambda = \frac{c_w}{e - fc_w} \tag{2.60}$$

the electro-osmotic drag coefficient n_d for Nafion117 expressed in (2.61) can now be re-written as a function of water concentration:

$$n_d = \frac{2.5}{22}\frac{c_w}{e - fc_w} \tag{2.62}$$

Substituting Eq. (2.62) into Eq. (2.55), the water transport equation can be finally obtained as:

$$-D_w \nabla^2 c_w - \varepsilon_w^m \frac{k_h}{\mu_l}(\vec{\nabla} c_w \cdot \vec{\nabla} p_l) + \frac{5}{44}\frac{e}{F(e - fc_w)^2}(\vec{\nabla} c_w \cdot \vec{i}) = 0 \tag{2.63}$$

which is a complete mathematical description of water concentration distribution in membrane. With the known pressure profile p_l and current density $\vec{i}$ in the membrane, Eq. (2.63) can be viewed as an nonlinear partial differential equation of c_w.

2.5.2.1.2 Proton Transport

The flux of protons through the membrane is determined by the *Nernst-Planck* equation, indicating that the migration, diffusion, and convection of the dissolved protons cause the net molar flux of protons:

$$\vec{N}_p = -Z_p \frac{F}{RT} D_p c_p \vec{\nabla} \phi_p - D_p \vec{\nabla} c_p + c_p \vec{V}_l \tag{2.64}$$

where Z_p is the charge number of ion, D_p is the diffusion coefficient, c_p is the molar concentration of protons, ϕ_p is the electric potential, i.e. membrane-phase potential, and V_l is the convective velocity of the liquid water.

The velocity of liquid water in the pores of the membrane can be estimated by the Schliögl equation [53,54]:

$$\vec{V}_l = \varepsilon_w^m \left(\frac{k_\phi}{\mu_l} Z_f c_f F \vec{\nabla}\phi - \frac{k_h}{\mu_l} \vec{\nabla} p_l \right) \tag{2.65}$$

where k_ϕ and k_h are the electric and hydraulic permeabilities of the membrane, respectively, Z_f is the charge number of the fixed charges, and c_f is the fixed-charged concentration.

Since the electric current results from the flux of charge species, the current density in the membrane can be expressed as:

$$\vec{i} = F \sum Z_j \vec{N}_j = F \vec{N}_p \tag{2.66}$$

where Z_j is the charge number of charged mobile ion of species j, and $Z_j = 1$ for the sole mobile ions, which are the hydrogen ions in this situation. $\vec{N}_j$ is the molar flux of ions. Therefore, Eq. (2.66) can reduce to:

$$\vec{N}_p = \frac{\vec{i}}{F} \tag{2.67}$$

The membrane ionic conductivity is generally defined as:

$$\sigma_m^p = \frac{F^2}{RT} \sum Z_j^2 D_j c_j \tag{2.68}$$

The electro-neutrality condition signifies that no net charge should exist in the membrane:

$$Z_f c_f + \sum Z_j c_j = 0 \tag{2.69}$$

Again, the sole charged mobile ion in the membrane is proton, and for H^+, $Z_p = 1$. Hence, Eq. (2.68) can be rewritten as:

$$\sigma_m^p = \frac{F^2}{RT} D_p c_p \tag{2.70}$$

and, Eq. (2.69) becomes:

$$Z_f c_f = -c_p \tag{2.71}$$

Substituting Eq. (2.71) into Eq. (2.64) and (2.65) results in:

$$\vec{N}_p = -\frac{F}{RT} D_p c_p \vec{\nabla}\phi_p - D_p \vec{\nabla} c_p + c_p \vec{V}_l \tag{2.72}$$

and

$$\vec{V}_l = \varepsilon_w^m \left(\frac{k_\phi}{\mu_l} c_p F \vec{\nabla}\phi - \frac{k_h}{\mu_l} \vec{\nabla} p_l \right) \tag{2.73}$$

Combining Eq. (2.72) and (2.73) with the divergence of Eq. (2.49) gives:

$$-\Delta\phi_p = -\frac{1}{\sigma_m^p} [\vec{\nabla}(\ln c_p) \cdot \vec{i}] + \frac{RT}{F} \vec{\nabla} \cdot [\vec{\nabla}(\ln c_p)] c_p \tag{2.74}$$

The membrane swells due to presence of internal liquid water. Therefore, c_p becomes a function of hydration instead of a constant. Since in the membrane the hydration index, λ, is defined as the number of moles of water per equivalent sulfonic acid group, for Nafion 117, the proton concentration can be described as:

$$c_p = \frac{c_w}{\lambda} \tag{2.75}$$

Substituting Eq. (2.57) into (2.75) leads to:

$$c_p = \frac{e}{f\lambda + 1} \tag{2.76}$$

Invoking Eq.(2.60) in Eq. (2.76), the relationship between the two concentrations becomes:

$$c_p = e - fc_w \tag{2.77}$$

Substituting Eq. (2.77) into Eq.(2.74), the electrical membrane-phase potential expression in the membrane in terms of water concentration c_w:

$$\begin{aligned} -\Delta\phi_p = &-\frac{1}{\sigma_m^p}\frac{f}{e-fc_w}\left(\vec{\nabla}c_w\cdot\vec{i}\right)-\frac{RTe}{F}\frac{f}{e-fc_w}\Delta c_w \\ &-\frac{RT}{F}\left(\frac{f}{e-fc_w}\right)^2\left(\vec{\nabla}c_w\cdot\vec{\nabla}c_w\right) \end{aligned} \tag{2.78}$$

In order to eliminate Δc_w, i.e. $\nabla^2 c_w$, Eq. (2.63) is substituted into Eq. (2.78) and the electric potential equation in the membrane accounting for swelling effect is eventually written as:

$$\begin{aligned} -\Delta\phi_p = &-\frac{f}{e-fc_w}\left(\frac{1}{\sigma_m^p}-\frac{5}{44}\frac{RTe}{D_w F^2(e-fc_w)^2}\right)\left(\vec{\nabla}c_w\cdot\vec{i}\right) \\ &+\frac{RT}{F}\frac{f}{e-fc_w}\frac{\varepsilon_w^m}{D_w\mu_l}\left(\vec{\nabla}c_w\cdot\vec{\nabla}p_l\right) \\ &-\frac{RT}{F}\left(\frac{f}{e-fc_w}\right)^2\left(\vec{\nabla}c_w\cdot\vec{\nabla}c_w\right) \end{aligned} \tag{2.79}$$

For the ionic conductivity of a Nafion117 proton exchange membrane, an empirical expression presented in [12] is:

$$\sigma_m^{ref} = 0.5139\lambda - 0.326 \quad \text{if} \quad \lambda \geq 1 \tag{2.80}$$

where σ_m^{ref} is the reference ionic conductivity measured at 303K. For the values of membrane water content, λ, less than 1, the reference ionic conductivity is assumed constant [12] . At other temperatures, it is corrected to be a function of operating temperature T [12]:

$$\sigma_m^p = \sigma_m^{ref}\exp\left[1268\left(\frac{1}{303}-\frac{1}{T}\right)\right] \tag{2.81}$$

2.5.2.2 Model (B): Membrane Swelling Effect Switched off

Unlike the membrane model (A) described in Section 2.5.2.1, the water and proton transport can also be modeled under assumption that the membrane swelling effect is negligible.

2.5.2.2.1 Water Transport

When the effects due to membrane swelling are considered negligible, i.e. the swelling coefficient $f = 0$, Eq. (2.60) relating the water concentration to the water content can be simplified:

$$\lambda = \frac{c_w}{e} \tag{2.82}$$

Re-arrangement of Eq. (2.58), (2.62), and (2.82) leads to:

$$n_d = \frac{2.5}{22}\frac{EW_m}{\rho_m^{dry}} c_w \tag{2.83}$$

Accordingly, the original water transport equation (2.63) becomes:

$$-D_w \nabla^2 c_w - \varepsilon_w^m \frac{k_h}{\mu_l}(\bar{\nabla} c_w \cdot \bar{\nabla} p_l) + \frac{5}{44}\frac{EW_m}{F\rho_m^{dry}}(\bar{\nabla} c_w \cdot \vec{i}) = 0 \tag{2.84}$$

2.5.2.2.2 Proton Transport

Similar to the derivation towards the water transport model without considering the swelling effect, a constant for the proton concentration, c_p, can be obtained through combination of Eqs. (2.82), (2.58) and (2.75):

$$c_p = \frac{c_w}{\lambda} = \frac{\rho_m^{dry}}{EW_m} \tag{2.85}$$

Therefore, the original electric potential equation (2.74) reduces to a Laplace equation:

$$-\sigma_m^p \Delta\phi_p = 0 \tag{2.86}$$

2.6. Boundary Conditions

An entire PEM fuel cell is consisting of a number of subdomains. In practice, some subdomians may be grouped to be subjected to a governing equation. For instance, the hydrogen is transported in the anodic gas channel, GDL, and CL; then, the Maxwell-Stefan equation for the hydrogen transport applies to all these three subdomains. Accordingly, the boundary conditions for the mass fraction of hydrogen are required only at the border of the grouped subdomains, while no specification of interfacial conditions is required between neighboring subdomains in the group. Figure 2.3 schematizes all boundaries of a 2D PEM

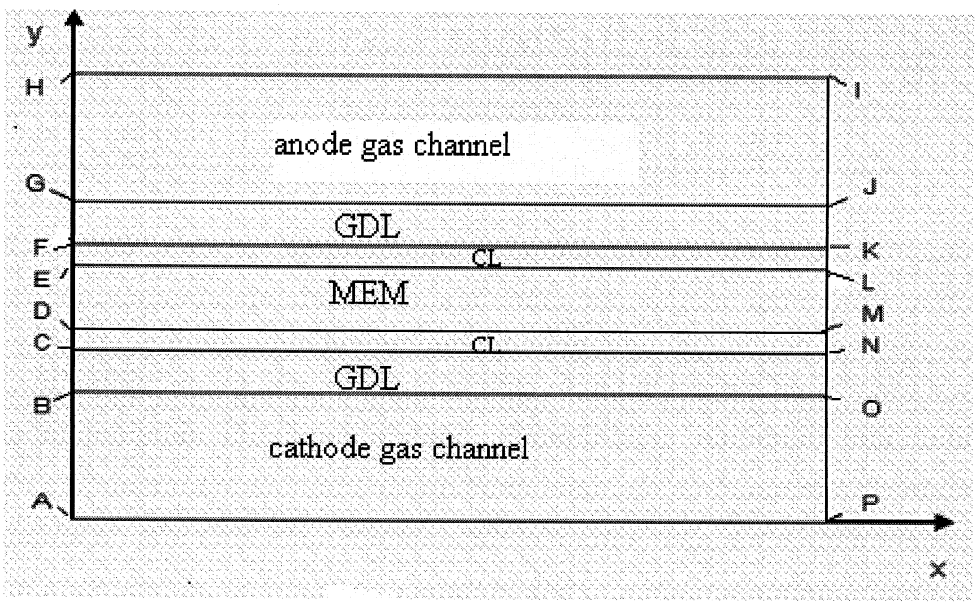

Figure 2.3 Schematic of the computational boundaries

fuel cell model in the *x-y* plane:

2.6.1. Boundary Conditions for Flow Field Model

At the inlets of both flow channels (segments AB, GH in Fig. 2.3), the mass flow rates are prescribed in conjunction with a fully developed laminar flow profiles. The boundary values of the anode/cathode inlet velocities are prescribed from the stoichiometric flow rate and reactant concentration:

$$V_{a,in} = \zeta_a \frac{i_{ref}}{2Fc_{H_2}} \frac{A_{react}}{A_{a,in}} \tag{2.87}$$

$$V_{c,in} = \zeta_c \frac{i_{ref}}{4Fc_{O_2}} \frac{A_{react}}{A_{c,in}} \tag{2.88}$$

where ζ_a and ζ_c are the anode and cathode stoichiometric flow ratios, respectively, which are defined as the ratio of the amount of reactant supplied to the amount of reactant required by the electrochemical reaction to generate the specified reference current density, i_{ref}, and A_{react} is the fully active MEA area. The pressures at both outlet flow channels (segments IJ, OP in Fig. 2.3) also need to be prescribed. All other boundaries (lines HI, FK, CN, AP and segments GF, JK, BC, ON in Fig. 2.3) use the *no slip* condition for the velocity.

Since Darcy's law is applied in the catalyst layers and membrane, the operating pressures need to be imposed at the interfaces between the anode/cathode catalyst layers and gas diffusers, i.e., lines GJ and BO in Fig. 2.3, respectively. Insulation condition is specified at boundary segments CF and KN in Fig. 2.3.

2.6.2. Boundary Conditions for Species Transport Model

The Maxwell-Stephan equations are applied to describe the species transport in the whole fuel cell unit except the membrane. At the anode and cathode inlet gas channels (segments GH, AB in Fig. 2.3), the mass fraction of H_2 and O_2 are prescribed using constant values; the mass fractions of water vapor at the anode and cathode sides are respectively calculated by the equations:

$$\omega_{H_2O,a} = RH \frac{p^{sat} M_{H_2O}}{p_a M} \tag{2.89}$$

and

$$\omega_{H_2O,c} = RH \frac{p^{sat} M_{H_2O}}{p_c M} \tag{2.90}$$

where RH is the relative humidity, p_a and p_c are the operating pressures at the anode and cathode sides; p^{sat} is the saturated water partial pressure calculated using the following empirical equation [12]:

$$\log_{10} p^{sat} = -2.1794 + 0.02953T - 9.1837\times10^{-5}T^2 + 1.4454\times10^{-7}T^3 \tag{2.91}$$

The outlet mass fractions are fully developed, i.e., the gradient of mass fraction of each species is zero. Also, homogeneous Neumann boundary conditions apply along the gas channel walls (lines AP, HI in Fig. 2.3) as well as along the interface between the catalyst layers and the membrane (lines EL, DM in Fig. 2.3), representing the gas-impermeable condition in the membrane.

2.6.3. Boundary Conditions for Energy Equations

For the energy equation, different boundary conditions can be used according to the cooling techniques. In this research work, a constant temperature, i.e., the ambient temperature T_{am}, is applied to the anode and cathode gas inlets (segments AB, GH in Fig. 2.3) as well as along the gas channel outer walls (lines IH, AP in Fig. 2.3).

At anode and cathode gas outlets (segments IJ, OP in Fig. 2.3), convective flux conditions are employed. Otherwise, the thermal insulation conditions are used for the boundary segments BG and JO in Fig. 2.3.

2.6.4. Boundary Conditions for Water Transport in the Membrane

Water can enter the membrane only from the interfaces between the membrane and the catalyst layers on both anode and cathode sides, hence, boundary conditions should be carefully set up along lines EL and DM in Fig. 2.3. In this research work, an equilibrium is assumed between the gas phase and the membrane phase of water in Nafion membrane and the membrane. Therefore, the water content at the interface (lines EL, DM in Fig. 2.3) is determined using [12]:

$$\lambda = 0.043 + 17.8a - 39.85a^2 + 36a^3 \qquad for \qquad 0 < a \leq 1 \tag{2.92}$$

where a is the activity of water vapor defined as:

$$a = \frac{x_{H_2O} p}{p^{sat}} \tag{2.93}$$

As the water mole fraction exceeds saturation, a linear relation is assumed between the water content and water activity [12]:

$$\lambda = 14 + 1.4(a - 1) \qquad for \quad 1 < a \leq 3 \tag{2.94}$$

and, furthermore, the water content is assumed to be a constant [12]:

$$\lambda = 16.8 \qquad for \quad a > 3 \tag{2.95}$$

The above calculated water content is used in conjunction with Eq. (2.57) to determine the concentration of water at the interfaces between the anode/cathode catalyst layers and the membrane. At the left and right boundary sides of the membrane (segments ED, LM in Fig. 2.3), the *Neumann* boundary condition is used:

$$\vec{n} \cdot \vec{\nabla} c_w = 0 \tag{2.96}$$

where $\vec{n}$ denotes the unit vector normal to the boundaries.

2.6.5. Boundary Conditions for Electron and Proton Transport Models

As electrons can not cross the membrane, the electron current density at interface between the catalyst layers and the membrane is set to be zero. Similarly, as protons can not go through the GDL, the proton current density at the interface between the catalyst layers and the GDL is zero as well.

Therefore, the solid-phase potential equation is applied in the anode and cathode GDLs and catalyst layers. In the present model, the boundary conditions are assigned as: nil ϕ_s along the anode GDL edge (line GJ in Fig. 2.3); along the cathode GDL edge (line BO in Fig.

2.3), the solid-phase potential ϕ_s is the cell voltage; the *Neumann* boundary conditions are applied at the other side boundaries (lines EL, DM and segment GE, LJ, BD,MO in Fig. 2.3).

Similarly, membrane-phase potential boundary conditions are required at the edges of MEA, i.e : a zero value of proton potential is specified at the interface between the cathode catalyst layer and membrane (line FL in Fig. 2.3); *Neumann* boundary conditions are applied at the other side boundaries (line CN and segments FC, KN in Fig. 2.3).

2.7. Modeling Parameters

To fully implement the developed PEM fuel cell computational model for numerical simulation, appropriate properties and parameters for the model need to be properly specified. In this research, the physical parameters and base operation conditions are mainly taken from the modeling work of Gurau et al. [19] or Zhou et al. [26] unless otherwise indicated.

The basic physical dimensions of the computational domain are shown in Table 2.1. Only half length of a PEM fuel cell unit is taken due to the limitation of available computation devices. All parameters refer to both anode and cathode sides. Also, Table 2.2 groups the basic parameters corresponding to the operating conditions for the base case study in this research, as detailed in Chpaters 3 and 4.

Table 2.1 Physical dimension of the PEM fuel cell [19]

Parameter	Value	Unit
Gas channel length (half) (x-direction)	0.025	m
Gas channel height (y-direction)	8.0×10^{-4}	m
Gas channel width (z-direction)	10×10^{-4}	m
Gas diffuser height (y-direction)	2.0×10^{-4}	m
Catalyst layer thickness	0.3×10^{-4}	m
Membrane thickness (y-direction)	2.3×10^{-4}	m

Table 2.2 Operating parameters for a PEM fuel cell under a base case computation [19]

Description	Value	Unit
T : fuel cell (ambient) temperature	333	K
ζ_a : stoichiometric ratio at anode	1.3	-
ζ_c : stoichiometric ratio at cathode	3	-
p_a : fuel inlet pressure at anode	1	atm
p_c : air inlet pressure at cathode	3	atm
RH : relative humidity of inlet gas mixture	100	%

The values of the binary diffusivities involved in the Maxwell-Stephan equations(2.6) are listed in Table 2.3. These are determined experimentally under the specific reference temperature and 1 atm pressure and should be converted to actual operating conditions used in our research by Eq.(2.5).

Table 2.3 Binary diffusivities at 1atm and reference temperatures [22]

Gas Pair	Reference Temperature $T_0[K]$	Binary Diffusivity $D_{ij}(T_0, p_0)[m^2 s^{-1}]$
$D^0_{H_2-H_2O}$	307.1	9.15×10^{-5}
$D^0_{H_2-CO_2}$	298.0	6.46×10^{-5}
$D^0_{H_2O-CO_2}$	307.5	2.02×10^{-5}
$D^0_{O_2-H_2O}$	308.1	2.8×10^{-5}
$D^0_{O_2-N_2}$	293.2	2.2×10^{-5}
$D^0_{H_2O-N_2}$	307.5	2.56×10^{-5}

Table 2.4 groups the electrode properties for the base case. The choice of electrochemical properties may have impact on the trend of polarization curve of a fuel cell. The electrochemical parameters chosen for this modeling study are organized in Table 2.5.

Table 2.4 Electrode properties

Description	Value	Unit	Ref.
ε_g : gas diffuser porosity	0.17	-	[34]
ε_m : membrane porosity	0.17	-	[34]
θ_{mc} : volume fraction membrane in catalyst layer	0.2	-	[34]
k_p : permeability to air in the gas diffuser	1.76×10^{-11}	m^2	[19]
k_h : hydraulic permeability of the membrane	1.58×10^{-18}	m^2	[19]
k_Φ : electrokinetic permeability of membrane	1.13×10^{-19}	m^2	[19]
k_{air} : air thermal conductivity	3.0×10^{-2}	$W\cdot m^{-1}K^{-1}$	[26]
k_{gr} : thermal conduc. of matrix of gas diffuser	150.6	$W\cdot m^{-1}K^{-1}$	[19]
$k_{m,dry}$: thermal conductivity of dry membrane	100	$W\cdot m^{-1}K^{-1}$	[19]
$c_{p,air}$: air specific heat at constant pressure	1008	$J\cdot kg^{-1}K^{-1}$	[19]
c_f : fixed charged site concentration in memb.	1.2×10^3	$mol\cdot m^{-3}$	[19]
z_f : charge of sulfonate site in memb.	-1	-	[19]
ρ_m^{dry} : membrane solid dry mass density	1980	$kg\cdot m^{-3}$	[19]
EW_m : equivalent membrane weight	1.1	$kg\cdot mol^{-1}$	[12]
f : membrane swelling coefficient	0.0126	-	[12]

Table 2.5 Electrochemical properties of a PEM fuel cell

Description	Value	Unit	Ref.
$aj_{0,a}^{ref}$: reference exchange current density times specific area at the anode	1.0×10^{9}	$A\cdot m^{-3}$	[34]
$aj_{0,a}^{ref}$: reference exchange current density times specific area at the anode	2.5×10^{3}	$A\cdot m^{-3}$	[34]
$c_{H_2,ref}$: H_2 reference molar concentration	40.88	$mol\cdot m^{-3}$	[34]
$c_{O_2,ref}$: O_2 reference molar concentration	40.88	$mol\cdot m^{-3}$	[34]
α_a^c :anodic transfer coefficient at cathode	0	-	[19]
α_c^c :cathodic transfer coefficient at cathode	1.2	-	[19]
α_c^a :cathodic transfer coefficient at anode	1/2	-	[19]
α_a^a :anodic transfer coefficient at anode	1/2	-	[19]

2.8. Computational Framework

As shown in preceding sections of this chapter, the PEM fuel cell modeling equations describing fluid flow, multi-species transport, heat transfer, and electric potentials are strongly nonlinear and coupled with each other. To numerically solve this large set of nonlinear equations, a finite element computational fluid dynamics package, FEMLAB is selected. Some physics application modules in FEMLAB and the FEMLAB Chemical

Engineering Module are employed in different computational subdomains as follows:

- Incompressible Navier-Stokes equations for flow field in gas channels and GDLs;
- Darcy's law for flow field in the catalyst layers and membrane;
- Maxwell-Stefan multi-component diffusion and convection equation for mass fractions of the species in the gas mixture in anode/cathode gas channels, GDLs and catalyst layers;
- Heat conduction and convection for temperature distribution throughout the PEM fuel cell computational domains;
- Poisson's equation for solid-phase and membrane-phase charge balances in GDLs, catalyst layers, and membrane;
- Special PDEs for liquid water and proton transport in the membrane to account for the membrane swelling effect.

FEMLAB uses a triangular mesh for 2D geometries. The rectangular physical domain is divided by a uniform grid along the flow direction (x-direction). Along the y-direction, as different domains have dramatically varying sizes, the element sizes have to be changed accordingly. Numerical tests were performed for the base case geometry to ensure that the solutions were independent of further refinement for the mesh.

In the current computer simulation, a stationary non-linear solver is used together with Direct (UMFPACK) linear system solver. The relative tolerance for the error criteria was

1.0×10^{-6}.

Due to limitation of the computer memory, the entire set of governing equations can not be solved simultaneously. The flow chart as shown in Fig. 2.4 is designed in a Gauss-Seidel like fashion to ensure an efficient decoupling of the flow, species transport, energy, and potentials from each other in the course of computation. Overall, this algorithm features predicting the cell current density distribution (output) from a specified cell operating voltage value (input), which is completely different from the current-to-voltage strategy that inevitably relies on the artificially averaged current value as well as some formulae of empirical nature for cell voltage calculation.

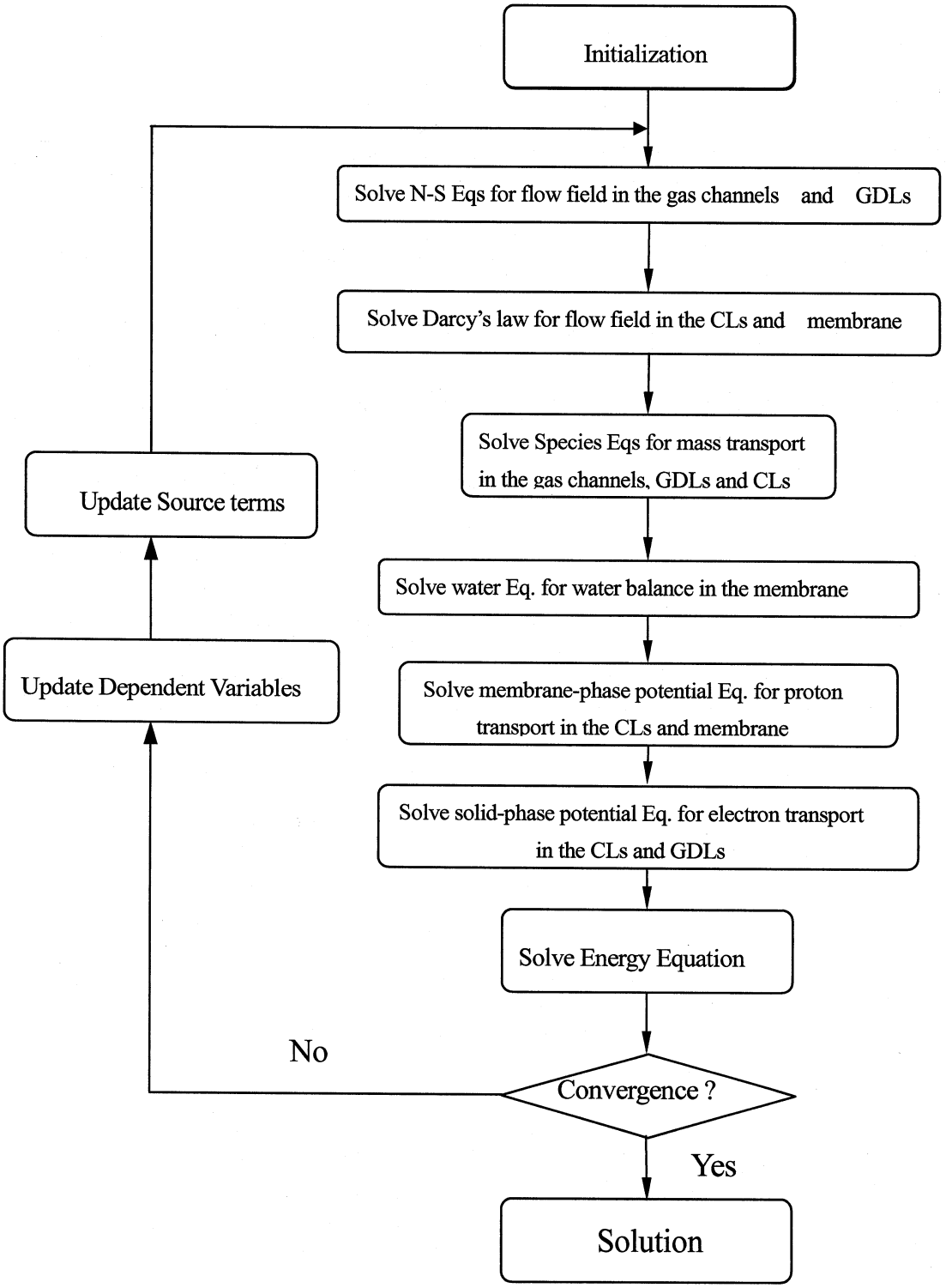

Figure 2.4 Flow chart of the solution procedure

Chapter 3. Base Case Results and Parametric Study

3.1. Model Validation and Cell Performance Illustration

To validate the model established in this study, comparisons have to be made with experimental data, where the output is the polarization curve, i.e., cell voltage vs. current density curves. Polarization curves are highly related to the distributions of the each species in a PEM fuel cell and also can be measured directly and accurately in experiments.

First, the PEM fuel cell model allowing for water variation in the membrane, which is identified as model (A) in the previous chapter, is examined. Figure 3.1 compares the fuel cell performance resulting from the model (A) corresponding to the base case conditions

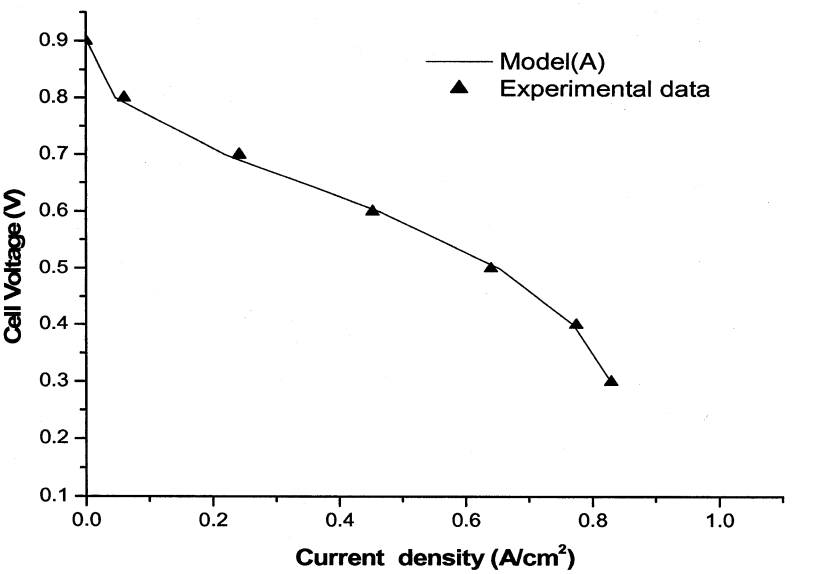

Figure 3.1 Comparison of computational model result with experimental data [34]

(Refer to Table 2.2) with the experimental data acquired by Hyuchul et al. [34]. A very good

agreement is seen between the two sets of results throughout the current density range observed. For the activation region ($0 \le |\vec{i}| \le 0.2 A/cm^2$ in this case), the slope of the polarization curve looks steeper and exhibits a slight nonlinearity. For the ohmic loss region ($0.2 A/cm^2 \le |\vec{i}| \le 0.6 A/cm^2$ in this case), the cell voltages drops clearly in a linear fashion as the current density increases. At higher current densities ($|\vec{i}| > 0.6 A/cm^2$ in this case), which is also called the mass transport limited region, the linear relationship between the cell voltage and the current density in the ohmic loss region can no longer persist; the steep drop of the cell voltage in this region can be explained by the fact that the stronger electrochemical reaction in response to a higher current density consumes almost all oxygen that has migrated to the reaction site, leading to a limitation of cell voltage output.

The post-treatment of the data obtained for depicting the polarization curve may yield other fuel cell performance information. For instance, the curve of power density (product of cell voltage and current density) vs. current density is plotted in Figure 3.2, which provides, from the numerical prediction, the maximum power density that the cell can reach. Below this maximum power point, the same power output may be obtained at either a lower current and a higher potential (on the left side of the maximum) or a higher current density and a lower potential (on the right side of maximum).

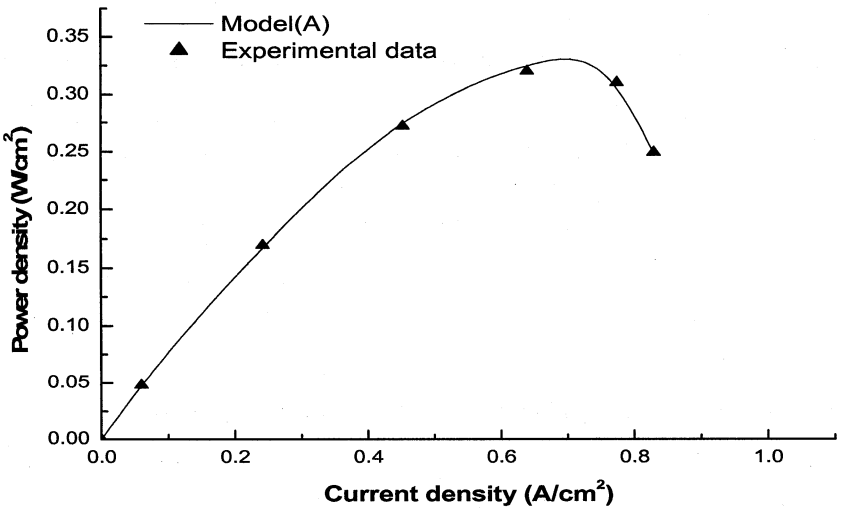

Figure 3.2 Power curve resulting from the fuel cell polarization curve

Also, the potential vs. current density data can be alternatively re-arranged to a curve of fuel cell efficiency, which is calculated by Eq.(1.8), vs. power density as shown in Figure 3.3. Evidently, a higher cell efficiency may be reached at significantly lower power density. This

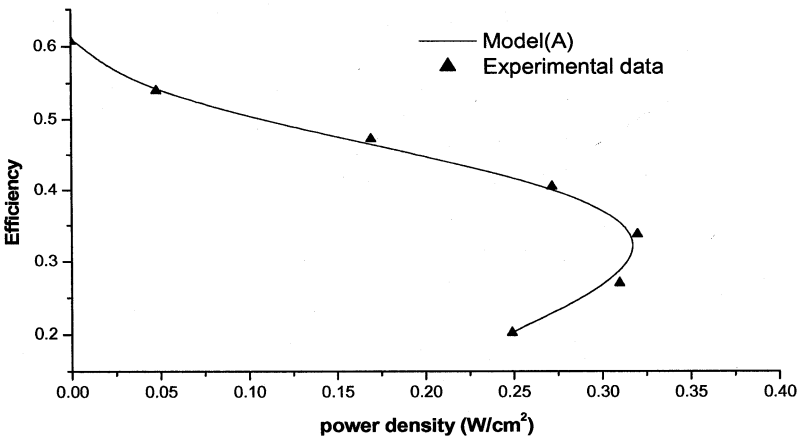

Figure 3.3 Fuel cell efficiency vs. power density

suggests that, for a required power output, a fuel cell may be made more efficient by selecting from the efficiency-power density plot an operating point corresponding to a higher efficiency. In. practice, it is unfeasible to adjust the dimension of fuel cell components for achieving the exact maximum power density output. More commonly, fuel cells are operated at a point in a balance between the maximum power density output and the highest achievable efficiency [35].

3.2. Base Case Study Using Water Transport Model (A)

The comprehensive current model can provide detailed information of transport phenomena in the fuel cell, which cannot be obtained by situ measurements. Numerical results, including the distributions of mole fractions of reactant gases, temperature, local current densities, various potentials, and water concentration in membrane, will be examined in the subsequent sections. The numerical simulation corresponds to the base case operational conditions as described in Table 2.2.

3.2.1. Flow Patterns

Figure 3.4 illustrates the fluid flow behavior in the gas channels and GDLs at both anode and cathode sides. A fully developed field is observed in the channels and keeps a laminar pattern till the end of channel. In this case, the Reynold Number, *Re*, in the channel is around 10 only, where the channel height is employed as the characteristic length .

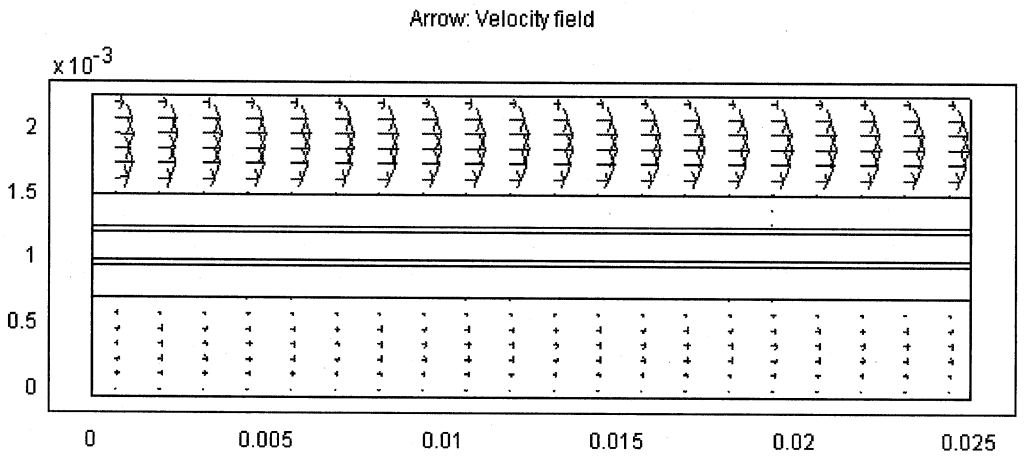

Figure 3.4 Velocity field in the fuel cell

Figure 3.5 demonstrats the velocity profiles at the x=0.01m. A few important flow features can be captured from Figure 3.5. First, inside the channel, the velocity changes

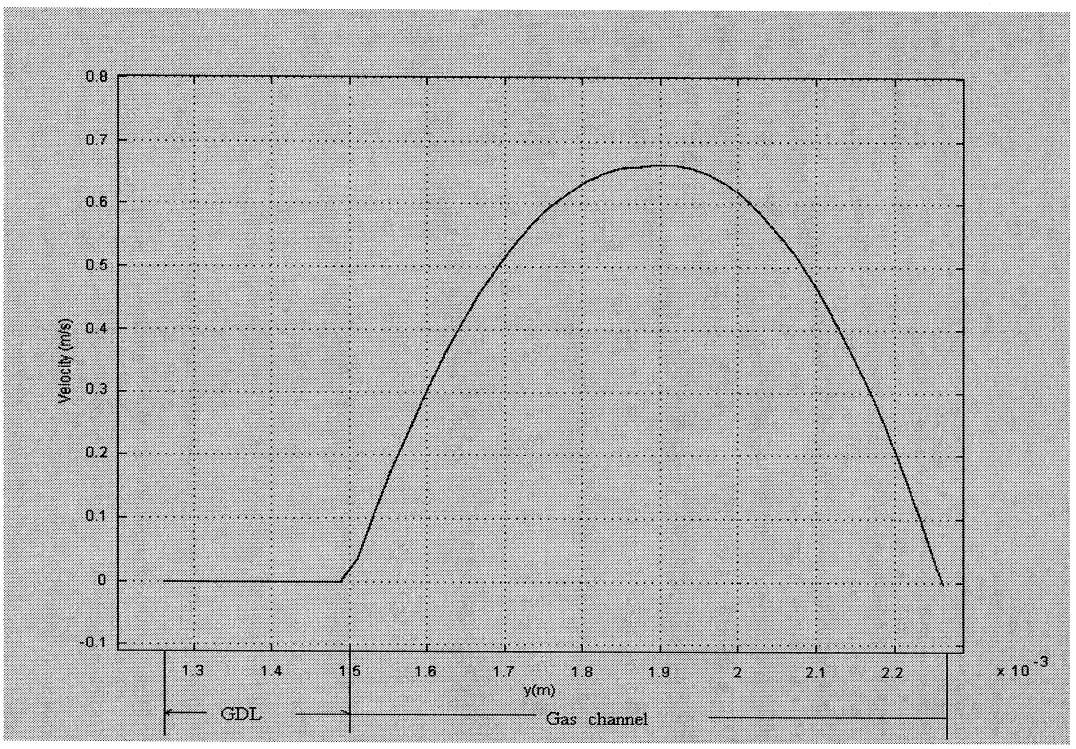

Figure 3.5 Velocity profile across the channel-GDL domain at the anode side

significantly with the radial position, but the velocity profile is asymmetric. This is because the channel is sandwiched by a solid wall and a porous GDL, which does not render to this region the symmetry in terms of material property. At the channel wall, the velocity drops to zero due to the no-slip condition. At the interface of the GDL and the channel corresponding to $y = 0.0015m$ on Figure 3.5, the flow exhibits a velocity of about 2 cm/s owing to the identical type of flow model, i.e., the Navier-Stokes equations, chosen for both the channel and the GDL without needing to artificially set an unrealistic nil-velocity interface condition.

3.2.2. Distributions of Reactants and Products

The transport of reactant and product gases has important effects on the performance of PEM fuel cell. Figure 3.6 - Figure 3.8 use the same display format - on the top is the hydrogen distribution on the anode side; in the middle is the oxygen distribution on the cathode side; and at the bottom is the water product distribution on the cathode side as well; but the three figures correspond to a lower current density ($0.2139\,A/cm^2$), a medium one ($0.6538\,A/cm^2$), and a higher one ($0.8297\,A/cm^2$), respectively. In general, the hydrogen and oxygen concentrations decrease gradually from inlet to outlet due to the consumption of reactant gases through the oxidation reaction in the anodic and cathodic catalyst layers. Also the oxygen and hydrogen mole fractions decrease slowly within the gas channels due to convection, while the decrease rate is higher in GDLs due to lack of convection and lower diffusivity on the sites. Because of the relatively low diffusivity of the oxygen compared to

the hydrogen and the low concentration of oxygen in ambient air, the oxygen depletion is noticeable.

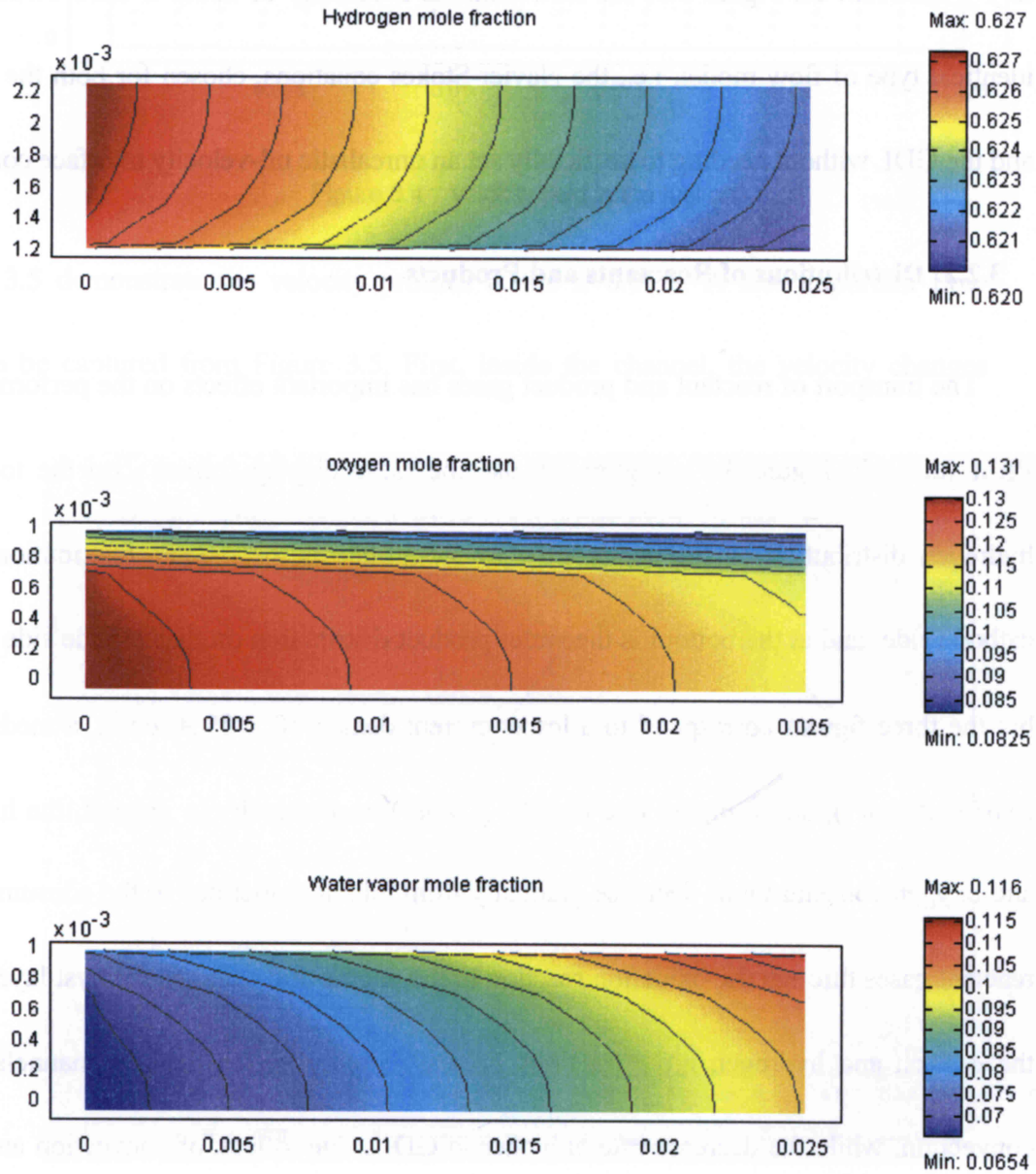

Figure 3.6 Reactant gas and cathode water vapor distribution in x-y plane at current density: 0.2139 A/cm^2

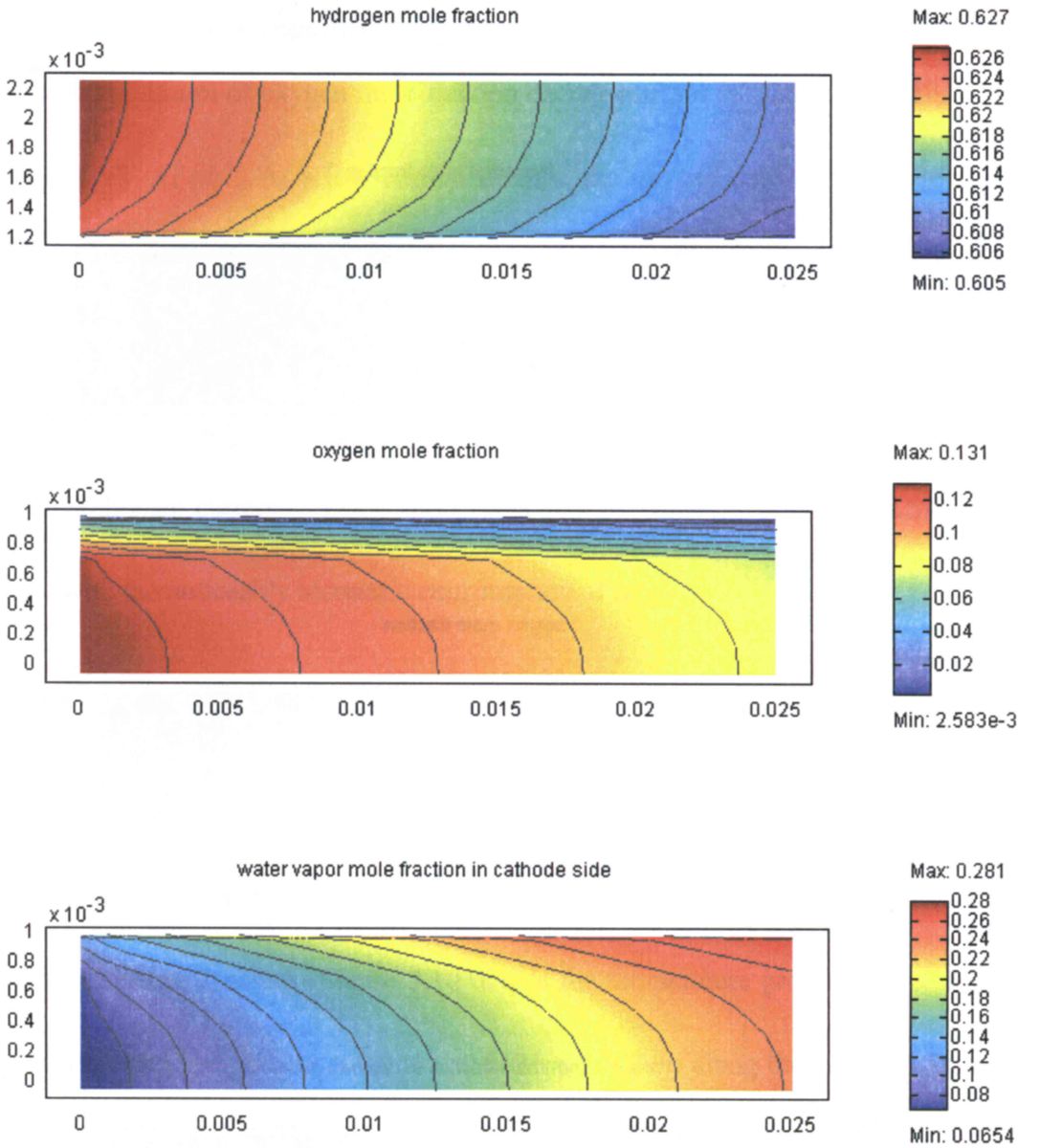

Figure 3.7 Reactant gas and cathode water vapor distribution in x-y plane at current density: 0.6583 A/cm^2

As the loading current density increases, more hydrogen and oxygen are depleted and

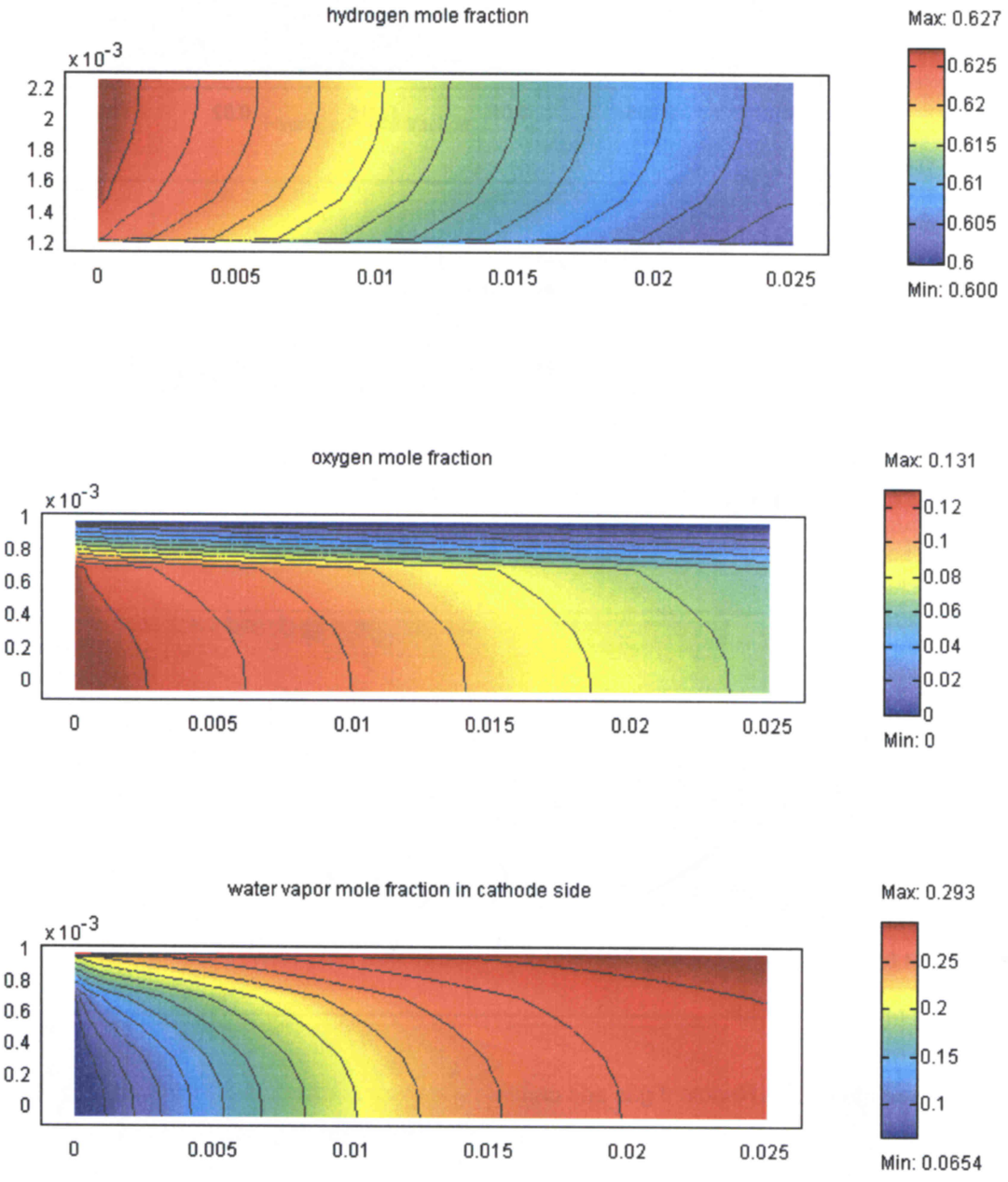

Figure 3.8 Reactant gas and cathode water vapor distribution in x-y plane at current density: 0.8297 A/cm^2

higher water vapor concentration is produced, as a result, the mass transport limitation for the oxygen within GDL and catalyst layer becomes significant as indicated in Figure 3.6 through Figure 3.8: the minimum of oxygen mole fraction decreases from 0.0825 at 0.2139 A/cm^2 to zero at 0.8297 A/cm^2. At a low current density, the oxygen consumption rate is low enough not to cause diffusive limitations, whereas concentration of oxygen within the cathode catalyst layer almost reaches near-zero value and can not further decrease. For the load of 0.8297 A/cm^2, the oxygen in cathode catalyst layer is almost depleted. Also, in response to a higher current density, the production of water is enriched, which is in consistency with the noticeably increased consumption of reactants.

3.2.3. Temperature Distribution

The temperature distribution inside a fuel cell has important effects on all transport phenomena. Figure 3.9 shows the temperature distribution on the *x-y* plane of the fuel cell for three different current densities. Figure 3.10 details the temperature profile across the fuel cell at three different locations (x = 0.004m, 0.0125m, 0.022m) along the channel. The inlet temperature of both sides is assumed to be identically at 333K, as well as the collector temperature.

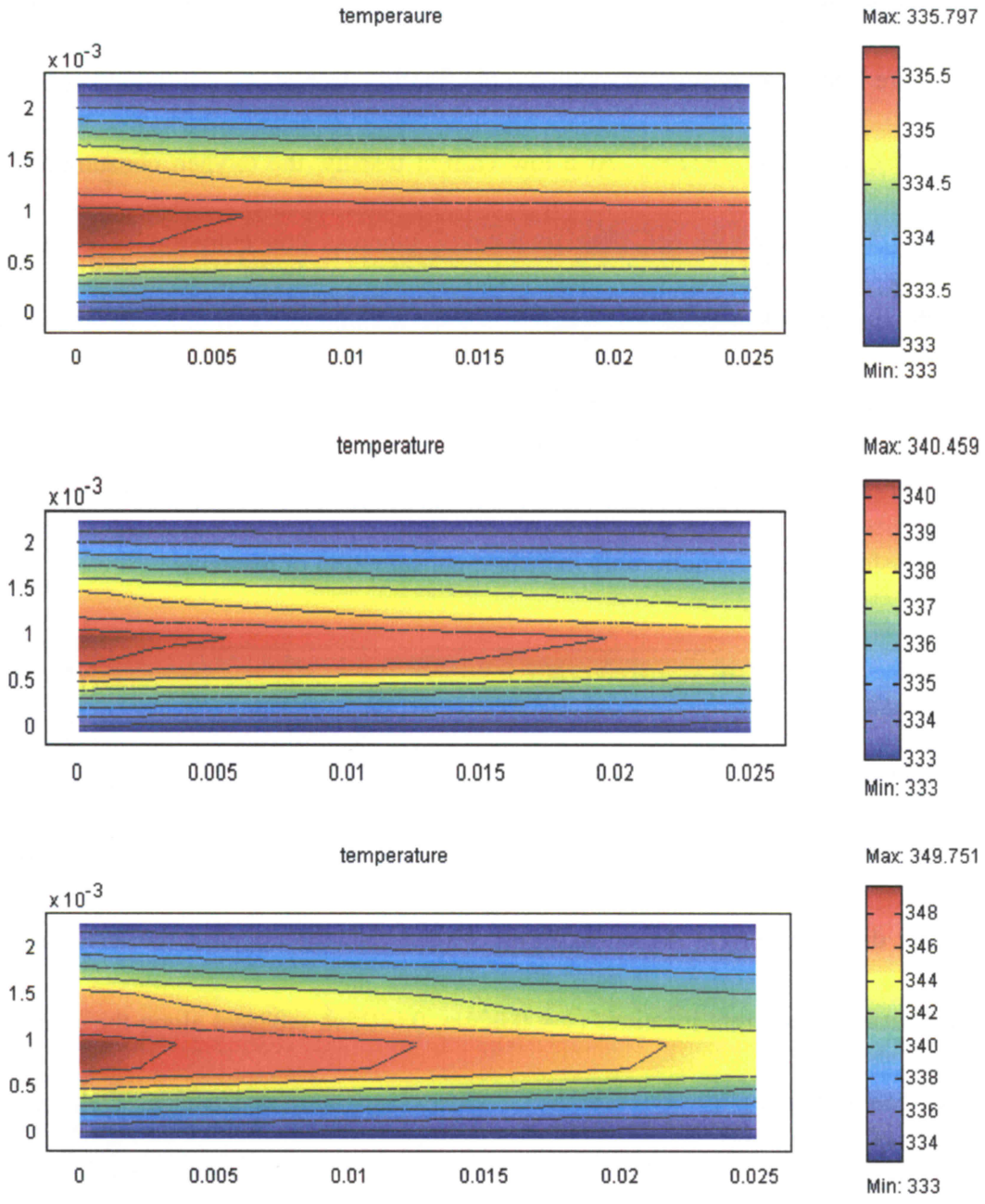

Figure 3.9 Temperature distribution across fuel cell in x-y plane for the three different current densities: 0.2139 A/cm^2 (top), 0.6583 A/cm^2 (middle) and 0.8297 A/cm^2 (bottom)

Since the major heat source is the chemical reaction and Joule heating in the catalyst layers, as shown as Figure 3.9 and Figure 3.10, the peaks of temperature are located within cathode catalyst layer and near the entrance, where the chemical reaction rate is highest. The temperature at the cathode side is slightly higher than at the anode side; this is because air at the cathode side is closer to the major heat source.

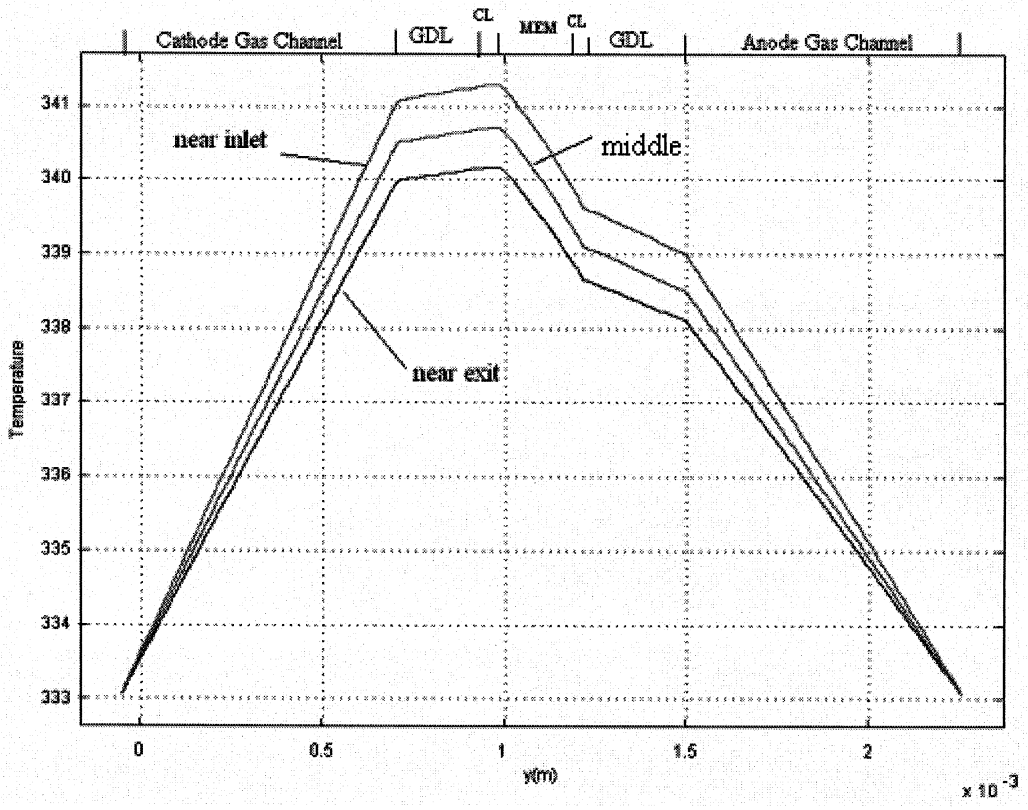

Figure 3.10 Temperature profile across the fuel cell for the current density: 0.6583 A/cm^2

It is also noticed that as the current density increases, the temperature maximum gets increased due to more heat generated from the chemical reaction. Also, corresponding to the

lower current density ($0.2139\,A/cm^2$), the temperature change over the whole cell is as small as about 2.8K; however, at the higher current density ($0.8297\,A/cm^2$), the maximum temperature is 16K above the ambient temperature.

The high degree of temperature non-uniformity along the catalyst layer revealed through the numerical simulation suggests that a redistribution of the catalyst deposition is demanded to reform the current density distribution and, consequently, effectively control the temperature distribution.

3.2.4. Water Content in Membrane

According to the model of water transport in membrane described in chapter 2, water content can be calculated using the liquid water concentration distribution. Figure 3.11 demonstrates the water content in the membrane for the base case at three different average current densities. Across the membrane, the water content at the anode side is lower than that at the cathode side. This is due to the electro-osmotic drag that prevents the water from migrating from the anode to the cathode, and the insufficient back-diffusion to the anode side from the cathode side, where water is produced.

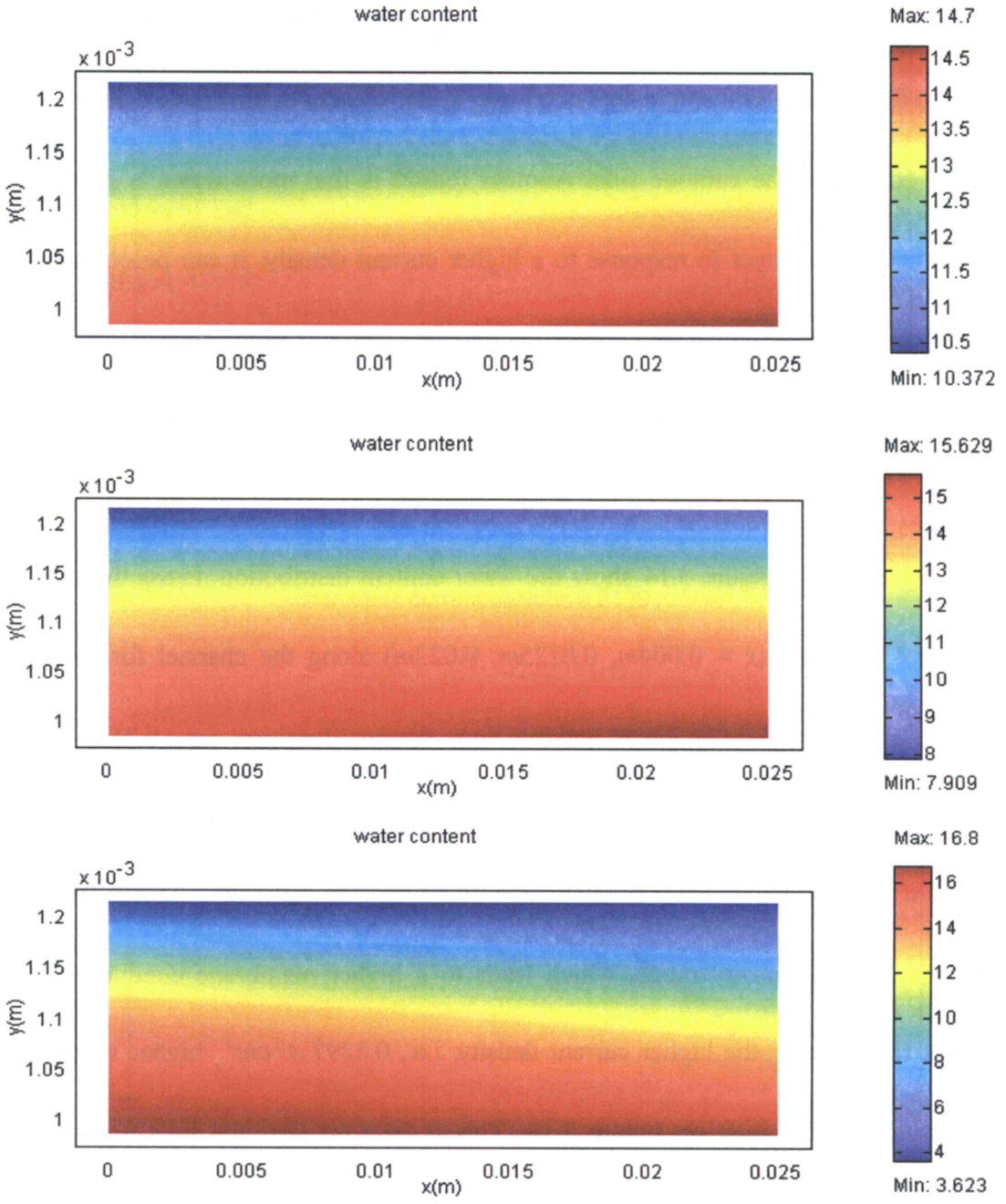

Figure 3.11 Water content distribution in membrane x-y plane for the three different current densities: 0.2139 A/cm^2 (top), 0.6583 A/cm^2 (middle) and 0.8297 A/cm^2 (bottom)

As the current density increases, a higher electro-osmotic drag, which is proportional to the water content as described in the precedent chapter, drives more water from the anode side to the cathode side and results in a lower water content at the anode side while a higher water content at the cathode side. Another reason is that more water is produced at the cathodic catalyst layer in response to a higher current density. It can be observed that the water content at the anode side decreases from 10.37 to 3.37 as the current density increases from 0.2139 A/cm^2 to 0.8297 A/cm^2, while that at the cathode side rises from 14.7 to 16.8.

Figure 3.12 - Figure 3.14 show the water content distribution across the membrane at different locations (x = 0.004m, 0.0125m, 0.022m) along the channel for three different current densities. At the lower and medium current densities, i.e., 0.2139 A/cm^2 and 0.6583 A/cm^2, the closer to the outlet, the more water content remains; this is because the trend of the increase in water accumulation along the channel is dominant in this lower and medium current density range, which leads to a higher membrane conductivity near the outlet. However, at the higher current density, i.e., 0.8297 A/cm^2, higher water content is observed near the inlet on Figure 3.14. This is because near the inlet a more complete reduction reaction occurs, generating a significantly large amount of water that overwhelms the increasing of water accumulation along the channel.

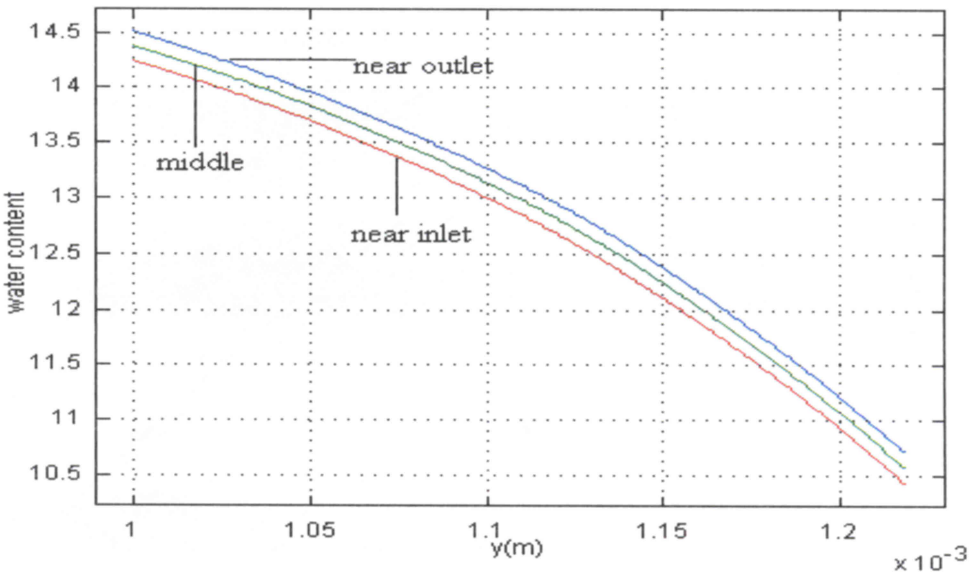

Figure 3.12 Water content distribution across the membrane at different locations along the channel at current density: 0.2139 A/cm^2

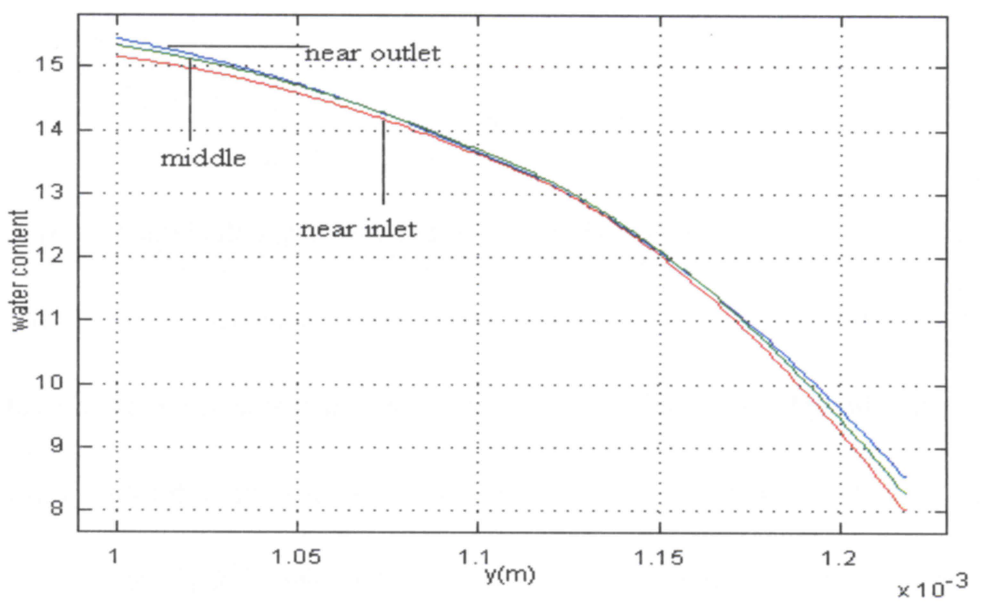

Figure 3.13 Water content distribution across the membrane at different locations along the channel at current density 0.6583 A/cm^2

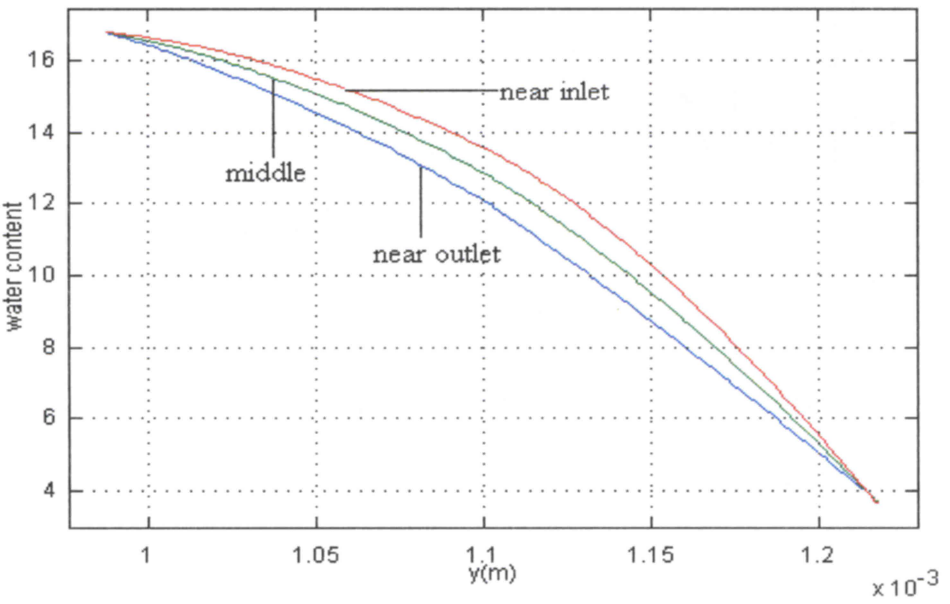

Figure 3.14 Water content distribution across the membrane at different locations along the channel at current density: 0.8297 A/cm^2

3.2.5. Membrane-Phase Potential Loss

The membrane-phase potential loss is due to resistance to the proton transport across the MEA from the anode side to the cathode side. Protons generated within the anodic catalyst layer pass through the membrane and are consumed inside the cathodic catalyst layer. Figure 3.15 shows the membrane-phase potential loss distribution for three different current density loadings. For all the three current densities, the membrane-phase potential is assumed 0 at the anode side for convenience of computational simulation.

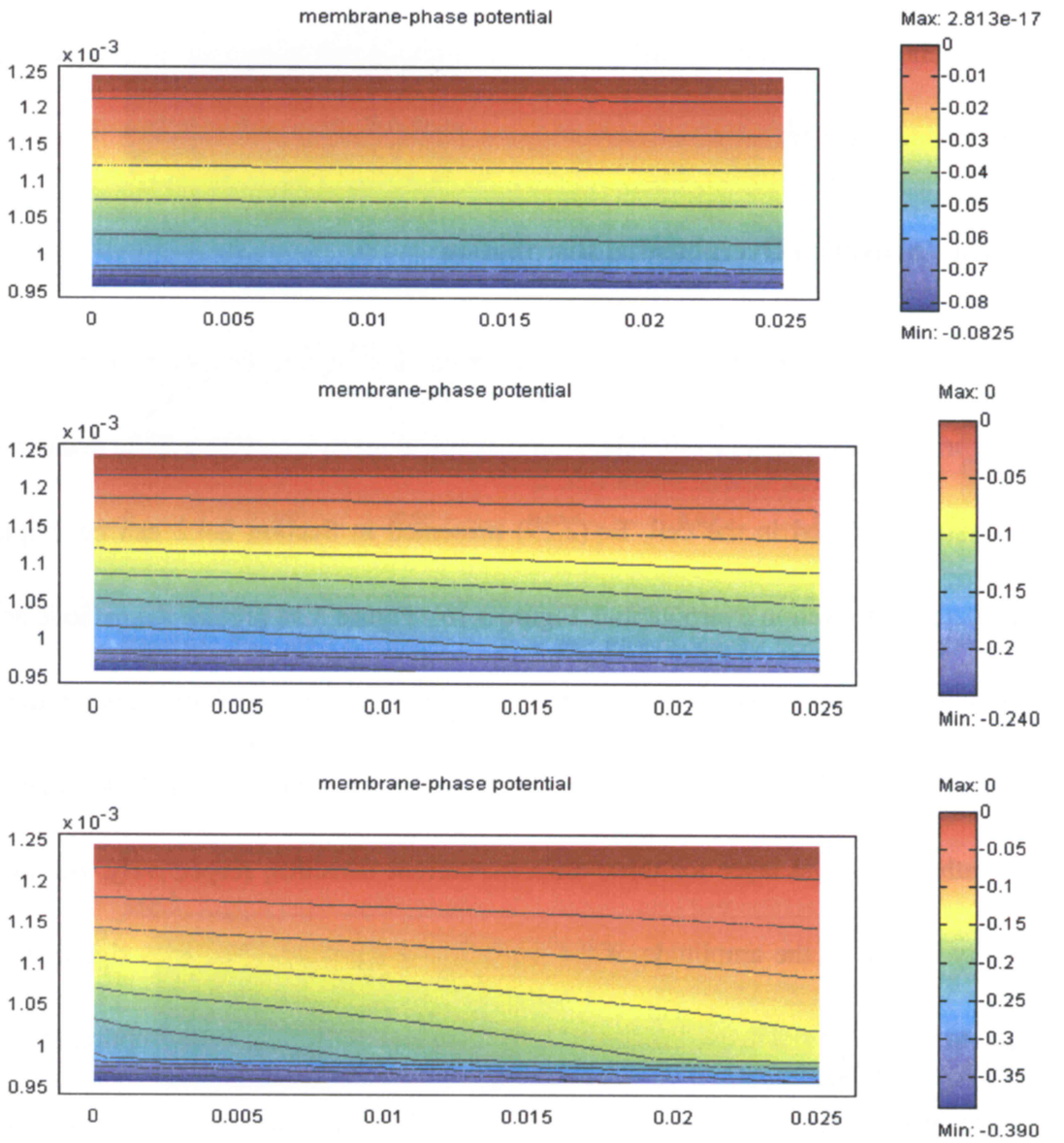

Figure 3.15 Membrane-phase potential distribution in MEA x-y plane for the three different current densities: 0.2139 A/cm^2 (top), 0.6583 A/cm^2 (middle) and 0.8297 A/cm^2 (bottom)

At the lower current density, the membrane-phase potential loss is small due to the small amount of protons flowing through the membrane. As the current density increases, the membrane-phase potential loss becomes significant. The equipotential lines indicate that the

membrane-phase potential loss is not uniform along the longitudinal direction. This potential loss reaches its maximum at the inlet, where protons are consumed fastest, leading to the highest rate of electrochemical reaction.

3.2.6. Activation Overpotential Distribution

The activation overpotential is the potential loss to the deviation from the original equilibrium state in order to start the electrochemical reactions. With a finite thickness set for catalyst layers used in the cell, Eq.(2.29) presented in Section 2.4.2 can be employed to calculate the activation overpotential. Figure 3.16 - Figure 3.18 present the cathode activation overpotential (in absolute values, note that the original activation overpotential in the catalyst layer is negative since it is below the equilibrium potential) and oxygen mole fraction inside the cathode catalyst layer for three different current densities, respectively. As the current density increases, the amplitude of the activation overpotential becomes significant, which leads to a more complete electrochemical reaction and, thus, more consumption of oxygen as shown in the three figures. In particular, Figure 3.18 indicates that the oxygen inside the cathodic catalyst layer is almost all depleted at the higher current density 0.8297 A/cm^2, which demonstrates the mass transport limitation leads to the current density limitation.

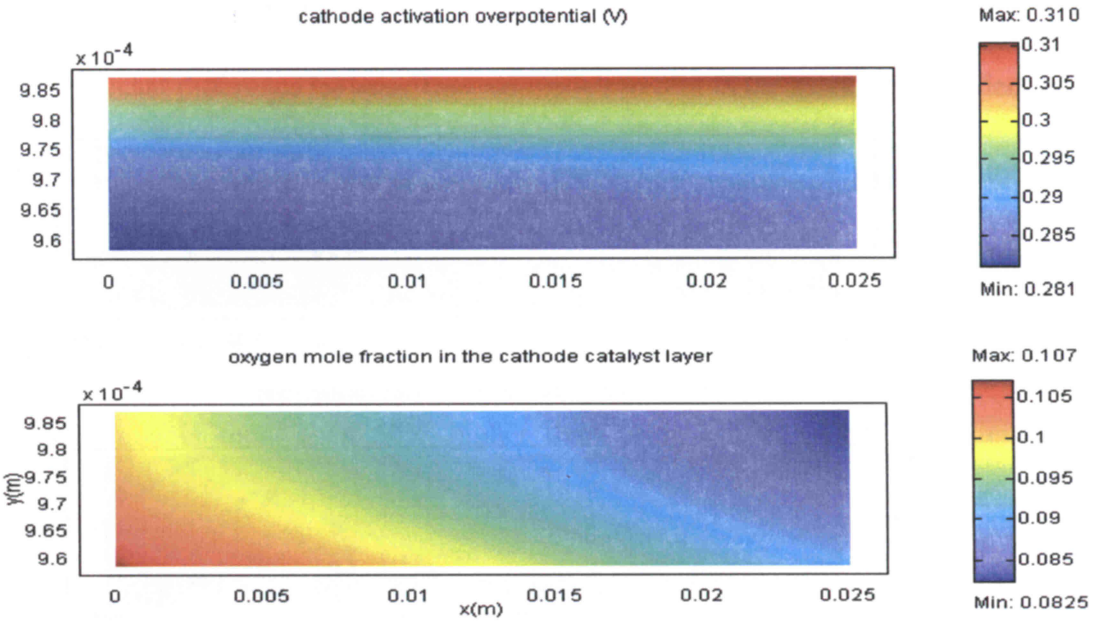

Figure 3.16 Cathode activation overpotential (absolute values) (upper) and oxygen mole fraction (lower) in the cathode catalyst layer for the current density: 0.2139 A/cm^2

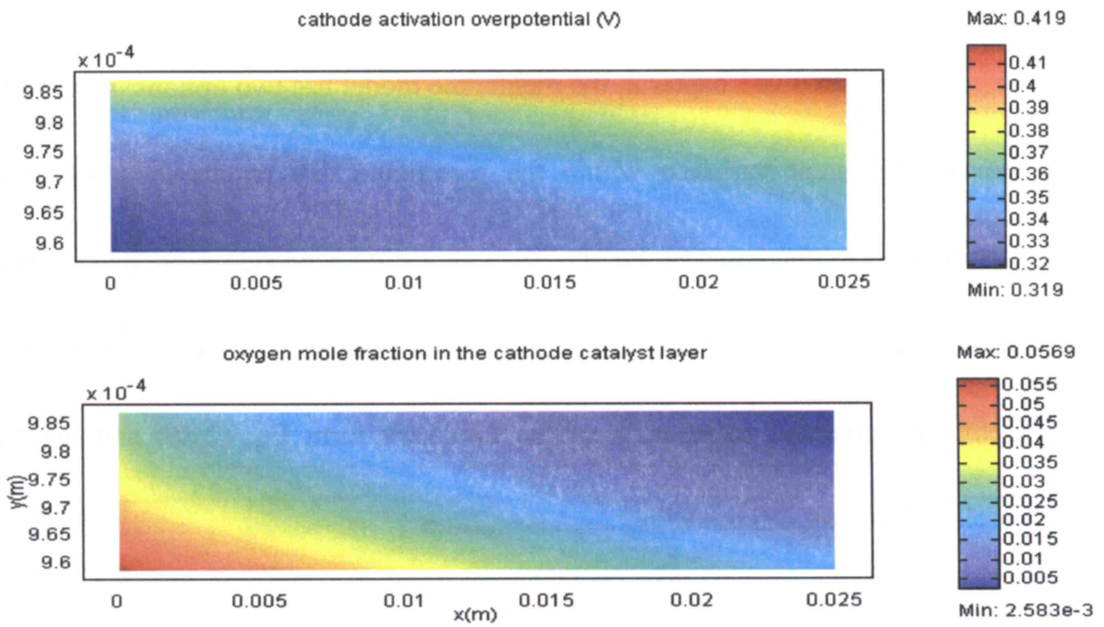

Figure 3.17 Cathode activation overpotential (absolute values) (upper) and oxygen mole fraction (lower) in the cathode catalyst layer for the current density: 0.6583 A/cm^2

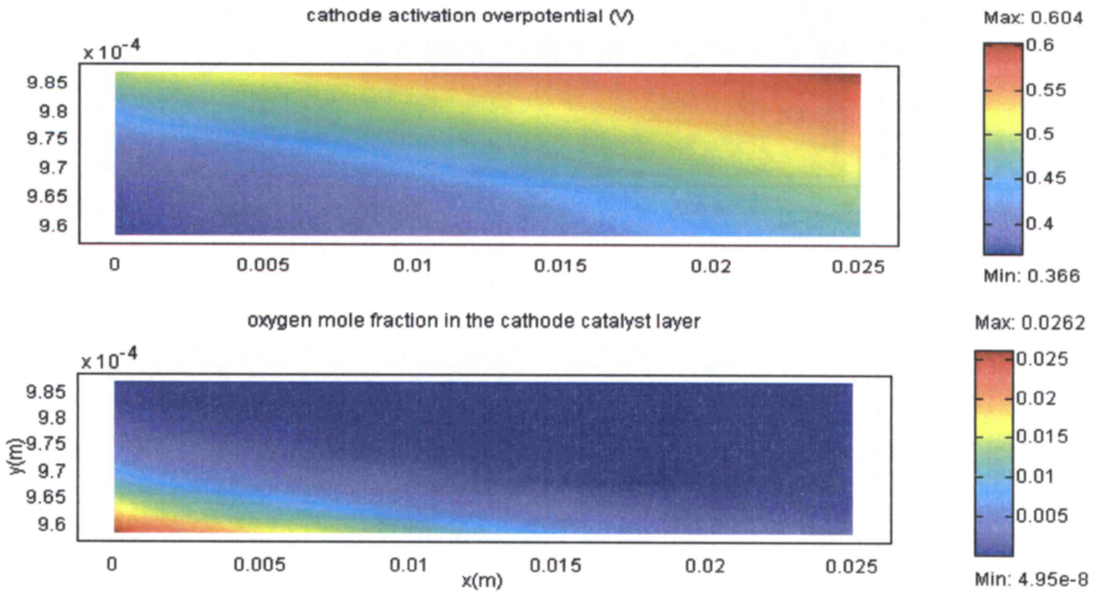

Figure 3.18 Cathode activation overpotential (absolute values) (upper) and oxygen mole fraction (lower) in the cathode catalyst layer for the current density: and 0.8297 A/cm^2

3.3. Comparison between Water Transport Models (A) and (B)

As mentioned in Chapter 2, the membrane model has two options: model (A) considers the water content variation within the membrane that results in a strongly nonlinear membrane potential equation Eq. (2.79) with a right hand side expressed as function of the water content; model (B) does not allow for water variation in the membrane, for which the membrane potential equation is of the Laplace's form Eq. (2.86) and has been widely employed for fuel cell modeling.

Figure 3.19 compares the performance curves for model (A) and model (B). In general, there is no significant difference between the two models except in the higher current density zone approximately staring $0.5\ A/cm^2$. A detailed comparison example is given at a current density of $0.6583\ A/cm^2$. As shown in Figure 3.20, the predicted maximum membrane-phase potential loss is 0.24V for model A, while for model (B) this maximum value can reach 0.37V, which is more than 50% higher than using model (A). This difference corresponding to higher current densities indicates that, when the water content variation is taken into account, model (A) allows the proton conductivity to vary within the membrane as described in Eq.(2.79), which provides the computation of the membrane potential loss with a more accurate proton conductivity distribution.

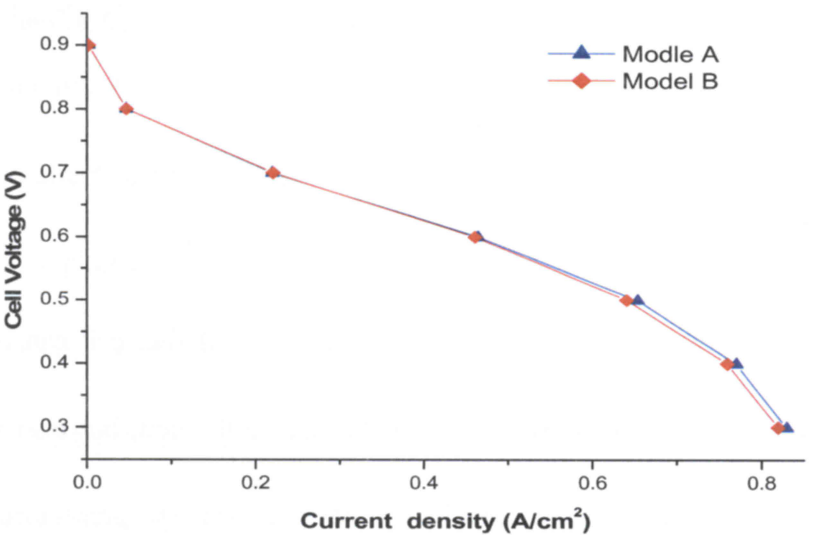

Figure 3.19 Comparison of polarization curves from the results of Model (A) and Model (B)

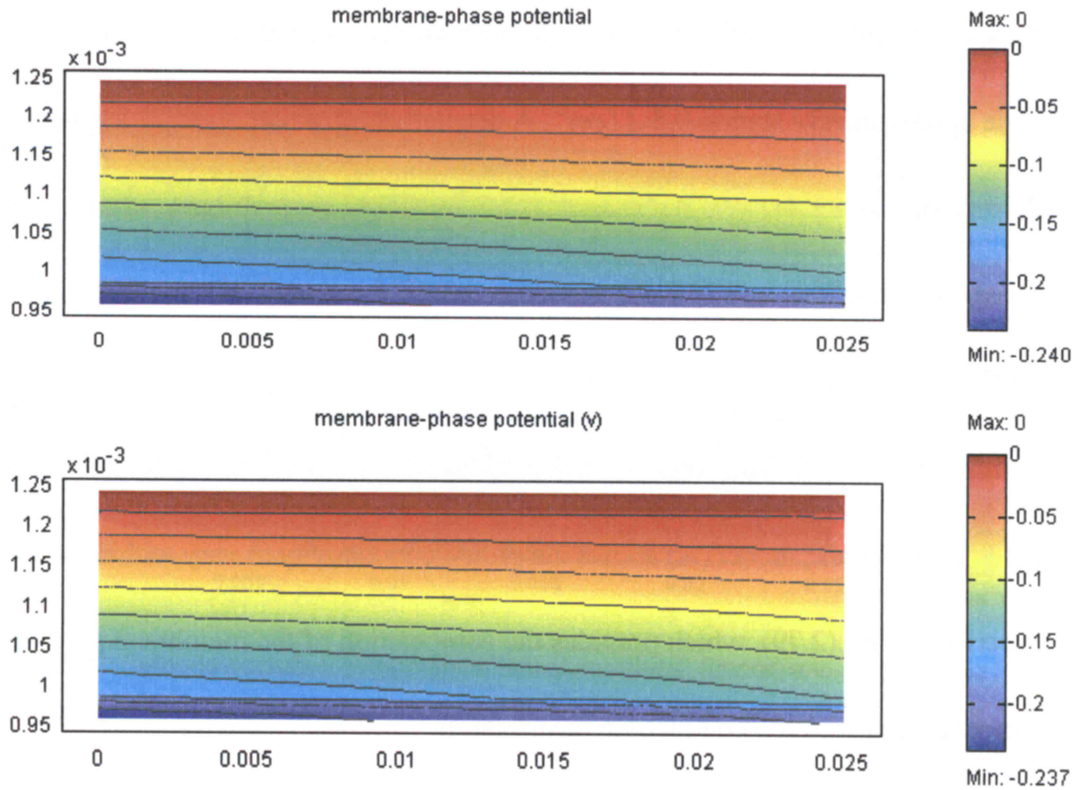

Figure 3.20 Membrane-phase potential distribution for the Model (A) (upper) and Model (B) (lower) at the current density: 0.6583 A/cm^2

3.4. Parametric Study

A comprehensive computational model for a PEM fuel cell can be used not only for revealing the details of transport phenomena inside the cell, but also for investigating the sensitivity of certain parameters on the cell performance. The present mathematical model is now applied to perform a systematic parametric study. A number of operating and design parameters are picked, including the inlet reactant relative humidity, the operating pressure,

and temperature, the porosities of the GDLs and catalyst layers, and the proton conductivity in the membrane. The performance characteristics of the fuel cell based on a selected parameter can be obtained by varying that parameter while keeping the others unaltered.

3.4.1. Effect of Relative Humidity

In the membrane, the presence of water is mandatory to maintain the proton conductivity. Therefore, both reactant gases typically need to be humidified before entering the cell. Relative humidity (RH) is a ratio of the partial pressure of water vapor to the saturation pressure, which physically represents the maximum amount of water vapor that can be present in the gas mixture given.

An additional complication is that the membrane-phase conductivity strongly depends on the temperature and water content inside the membrane as described in Eq.(2.79), which in turn is a function of relative humidity outside the membrane,.

To study the effect of relative humidity, numerical simulations under different relative humidity values ranging from 50% to 100% for both reactant gases are implemented and their polarization curves are given in Figure 3.21. It clearly shows that as the relative humidity decreases, the slope of the polarization curve is steeper, demonstrating the cell performance decline. Consequently, at lower RHs, fuel cell can not work towards a higher current density.

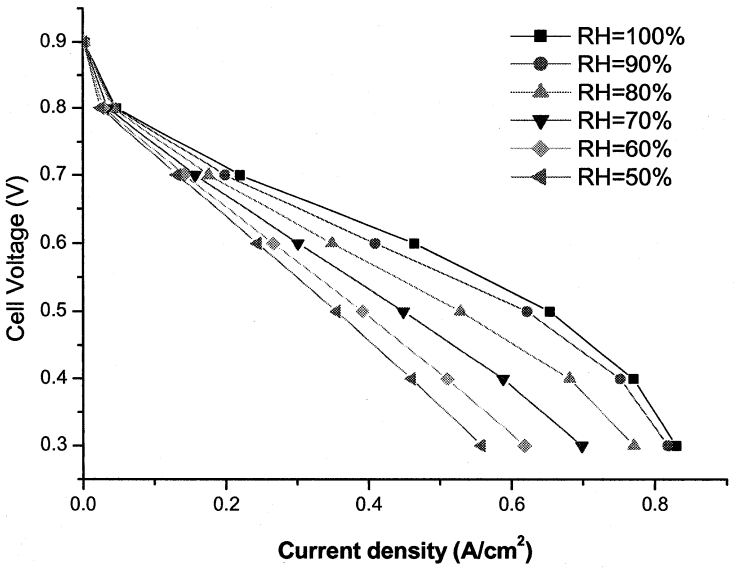

Figure 3.21 Polarization curves corresponding to different relative humidity

Figure 3.22 and Figure 3.23 illustrate the water content and membrane potential loss at a cell voltage of 0.6V for RH at 50% and 80%, respectively. At this cell voltage, it is easily seen that the water content decreases and the membrane-phase potential loss increases in response to the reduction of RH. Consistently, a re-visit can be paid to Figure 3.21, on which the average current density goes up from 0.2444 A/cm^2 to 0.3491 A/cm^2 when the RH is increasing from 50% to 80%. This suggests that maintaining the reactant gases as fully humidified as possible may help reduce the membrane-phase potential loss and increase the current density.

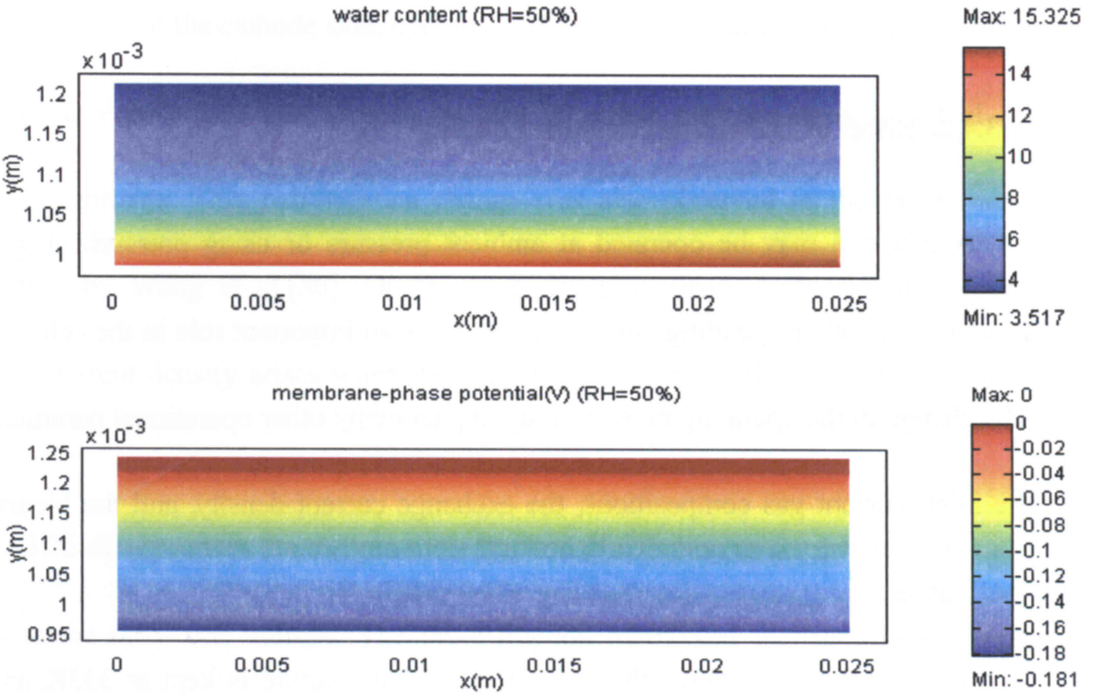

Figure 3.22 Water content and membrane-phase potential loss at cell voltage 0.6V and 50% RH

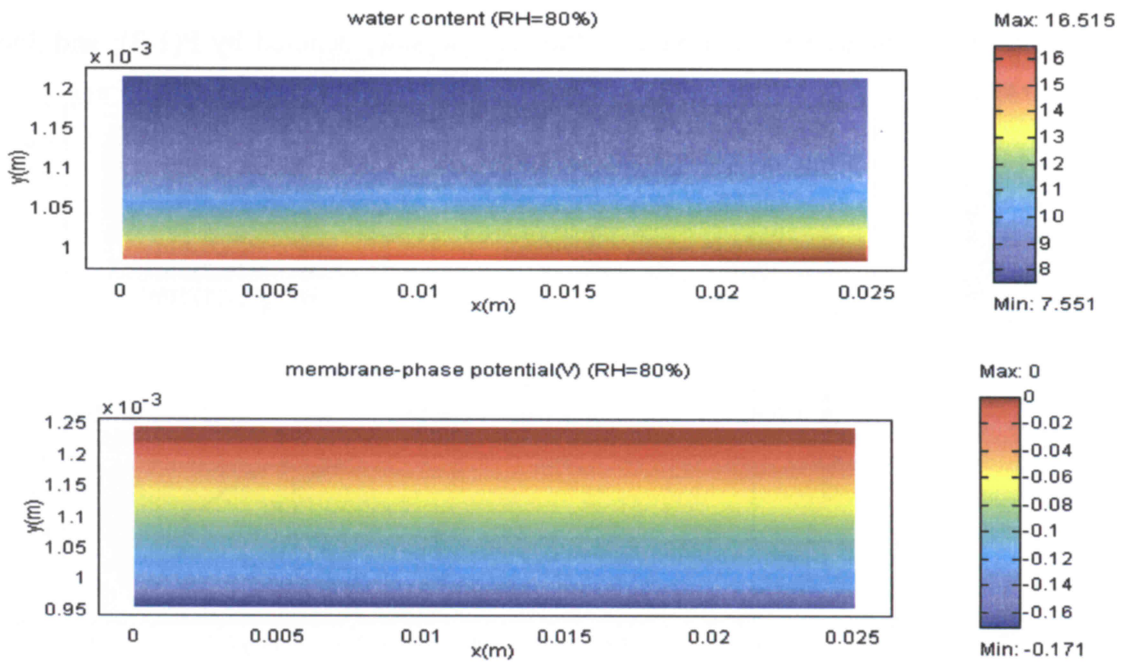

Figure 3.23 Water content and membrane-phase potential loss at cell voltage 0.6V and 80% RH

3.4.2. Effect of Operating Pressure Loading

A fuel cell may be operated at ambient pressure or using pressurized gas supplies. Pressure is another operating parameter that plays an important role in the cell performance. The change in the operating pressure may impact many other operational parameters such as the inlet reactant gas compositions, the exchange current density, and the binary diffusion coefficients.

In this parametric study, the cell operating temperature is kept at 333K and the inlet reactant gases remain fully humidified, while the three different pairs of operating pressure conditions are tested: 1atm at the anode side and 1atm at the cathode side, denoted by P(1-1); 1atm at the anode side and 3atm at the cathode side, denoted by P(1-3); and 3atm at the

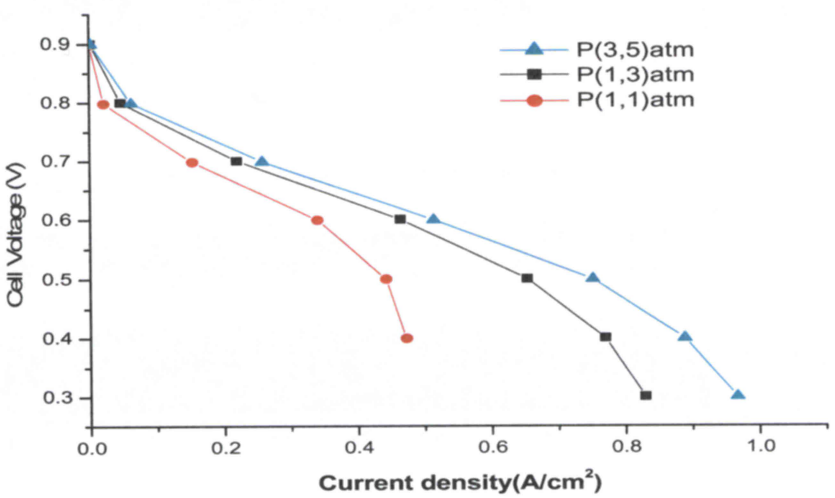

Figure 3.24 Cell performance at different operating pressure loading

anode side and 5atm at the cathode side, denoted by P(3-5). The resulting polarization curves are grouped in Figure 3.24. In general, as the operating pressure rises, the fuel cell performance improves. This performance change was also observed in the experimental study reported by Wang et al.[36]. On the contrary, it is easily noticed that a serious limitation of current density arises when the fuel cell works under the ambient pressure at both sides.

Figure 3.25 demonstrates the oxygen mole fraction distribution under different operating conditions at the 0.6V cell voltage. The mole fraction of oxygen increases under higher operating pressures. Therefore, when highly pressurized oxygen and hydrogen are supplied more reactant gases can be provided to the electrochemical reaction, resulting in a better cell performance.

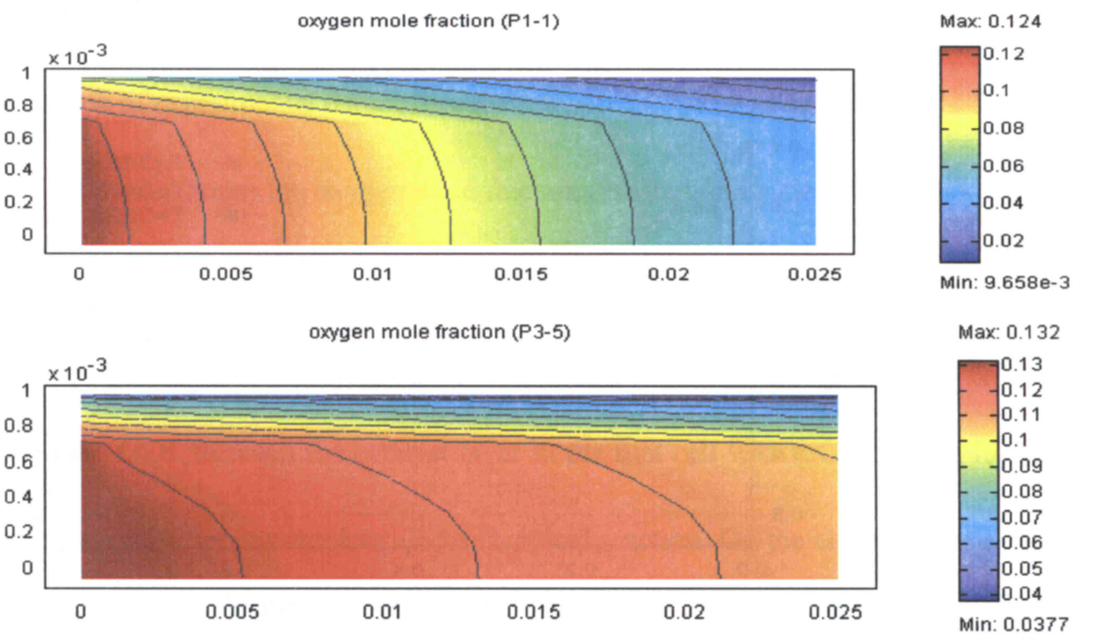

Figure 3.25 Oxygen mole fraction distribution under different operating pressure conditions at the cell voltage 0.6V

3.4.3. Effect of Operating Temperature

Temperature change influences all transport phenomena and, in particular, the electrochemical kinetics inside the fuel cell. In this study, operating temperatures vary from 333K to 353K. The change in temperature will cause in turn the changes in the exchange current density, the proton conductivity, and the gas diffusion coefficients, which can be calculated using Eqs. (2.27), (2.28), (2.81), and (2.5), respectively.

Figure 3.26 compares the polarization curves of the cell at the three different operating temperatures. An improved cell performance can be seen with elevated temperature. This is in agreement with the experimental parametric study [36]. However, the gain is larger in the ohmic loss region (the middle interval of the current density) than the activation overpotential loss region (the starting interval of the current density). This observation could

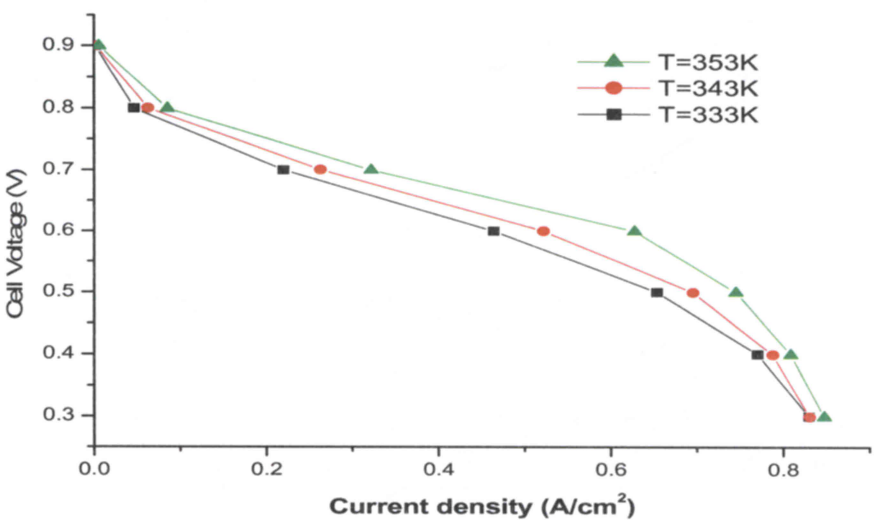

Figure 3.26 Effect of temperature on fuel cell performance

be explained by the increase in gas diffusivity and membrane conductivity at higher temperature.

3.4.4. Effect of GDL Porosity

The porosity of GDL can impact the fuel cell performance in two approaches. First, the porosity of GDL has effect on the mass transport of reactant gases from the channel towards the catalyst layers. Higher volume porosity provides a positive effect on mass transport, especially on oxygen mass transport under a higher current density. In the present model, the porosity affects the gas diffusion coefficients through the Bruggemann correction expressed by Eq. (2.18). Second, the porosity has a side effect on electron conduction, since the solid matrix of the GDL provide the pathways for electron transport and the higher porosity increases resistance to the electron transport in GDL [27]. Here, this effect is not discussed in details due to lack of experimental data.

Figure 3.27 demonstrates the oxygen mole fraction distribution inside at the cathode side with different porosities of GDL, while Figure 3.28 focuses on this reactant distribution inside the cathodic catalyst layer only. It is clearly observed that more oxygen molecules diffuse across the GDL to reach the catalyst layer in the fuel cell with a GDL at the higher porosity, allowing for a more complete electrochemical reaction. On the contrary, for a fuel cell with GDLs at lower porosity, it becomes more difficult for oxygen to diffuse across the GDL; consequently, only an insufficient amount of oxygen can reach the catalyst layer and

then is consumed by the electrochemical reaction.

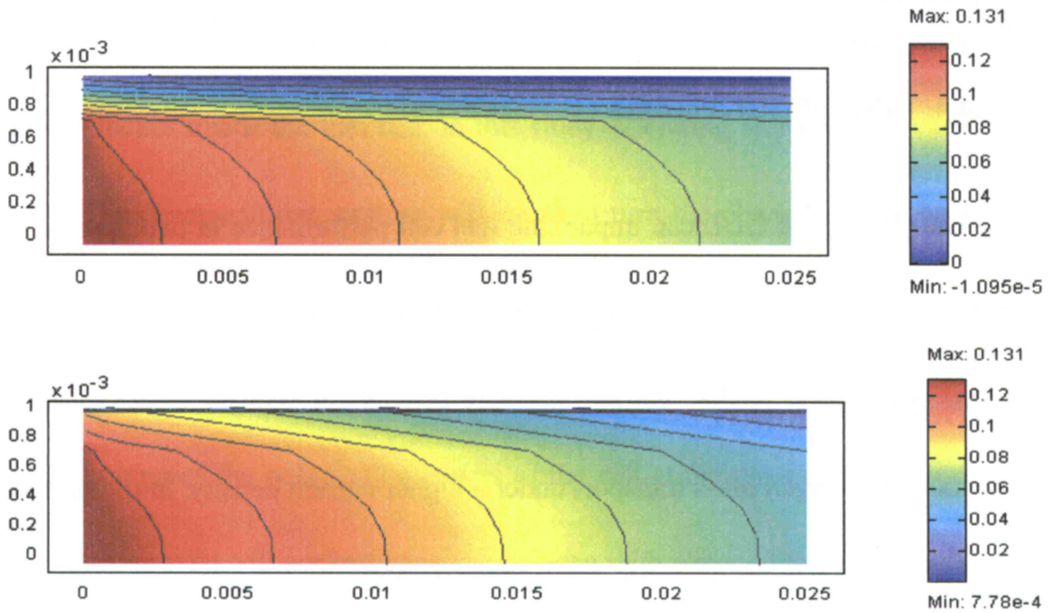

Figure 3.27 Oxygen mole fraction distribution inside fuel cells with different GDL porosities: $\varepsilon_g = 0.17$ (upper) and $\varepsilon_g = 0.4$ (lower) at cell voltage 0.4V

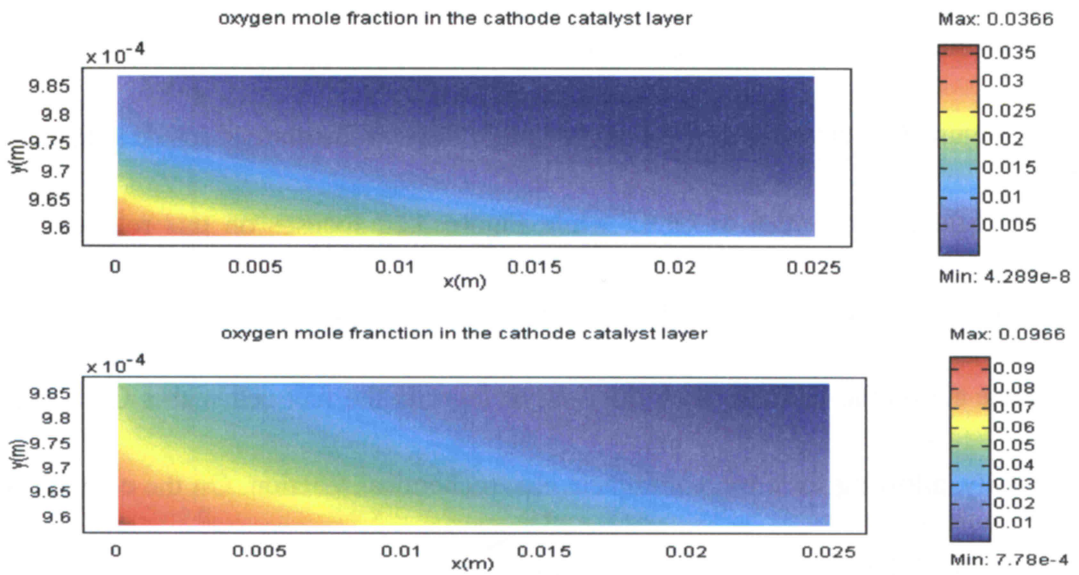

Figure 3.28 Oxygen mole fraction distribution inside cathode catalyst layer with different GDL porosities: $\varepsilon_g = 0.17$ (upper) and $\varepsilon_g = 0.4$ (lower) at cell voltage 0.4V

The effects of GDL porosity on the fuel cell performance are shown in Figure 3.29 using polarization curves. It is evident that the fuel cell with a higher GDL porosity enlarges the limitation of current density though diffusing more reactant gases towards the reactive areas.

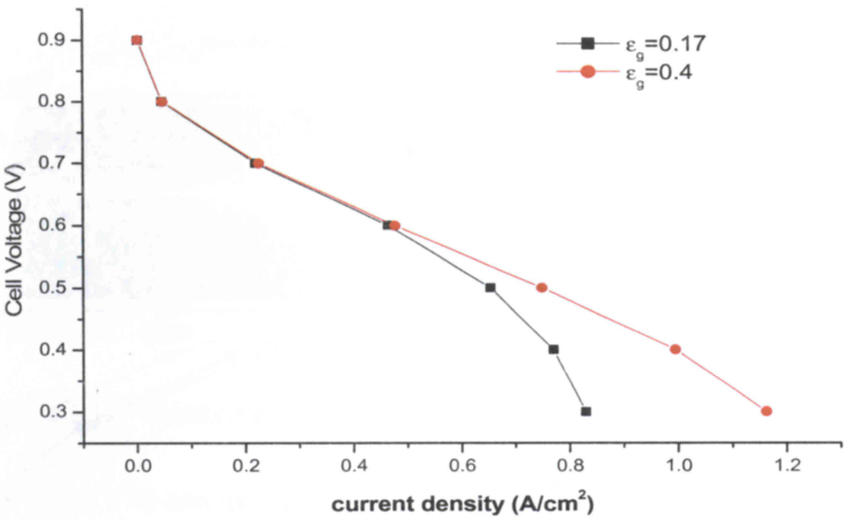

Figure 3.29 Effect of GDL porosity on fuel cell performance

3.4.5. Effect of Proton Conductivity

The proton conductivity is the most important electrolyte property and plays the most important role of in the membrane used for a PEM fuel cell. Although water and proton transport in the polymer electrolyte occurs concurrently, a simple effect of proton conductivity is studied assuming the proton conductivity to be constant inside MEA.

The polarization curves, corresponding to two constant proton conductivities, 10

$\Omega^{-1}m^{-1}$ and 14 $\Omega^{-1}m^{-1}$, and a varying proton conductivity based on Eq. (2.81), are plotted in Figure 3.30. Obviously, the fuel cell performs better at higher proton conductivity. The gain in performance is larger in the ohmic loss region rather than in the activation overpotential loss region.

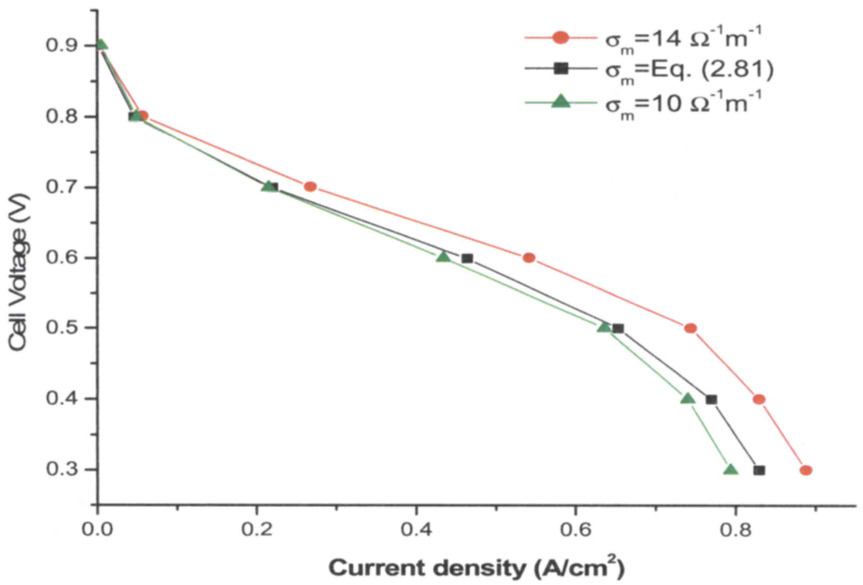

Figure 3.30 Effect of proton conductivity on fuel cell performance

Because of the ohmc resistance, there is a potential loss inside the MEA from the anode catalyst layer/diffuser interface to the cathode catalyst layer/diffuser interface. Figure 3.31 shows the membrane-phase potential loss in membrane for two proton conductivities at 10 S/m to 14 S/m, respectively. As the proton conductivity increases from 10 S/m to 14 S/m, the membrane-phase potential loss is reduced from 0.172V to 0.153V, which indicates that higher proton conductivity can reduce the proton resistance in the membrane.

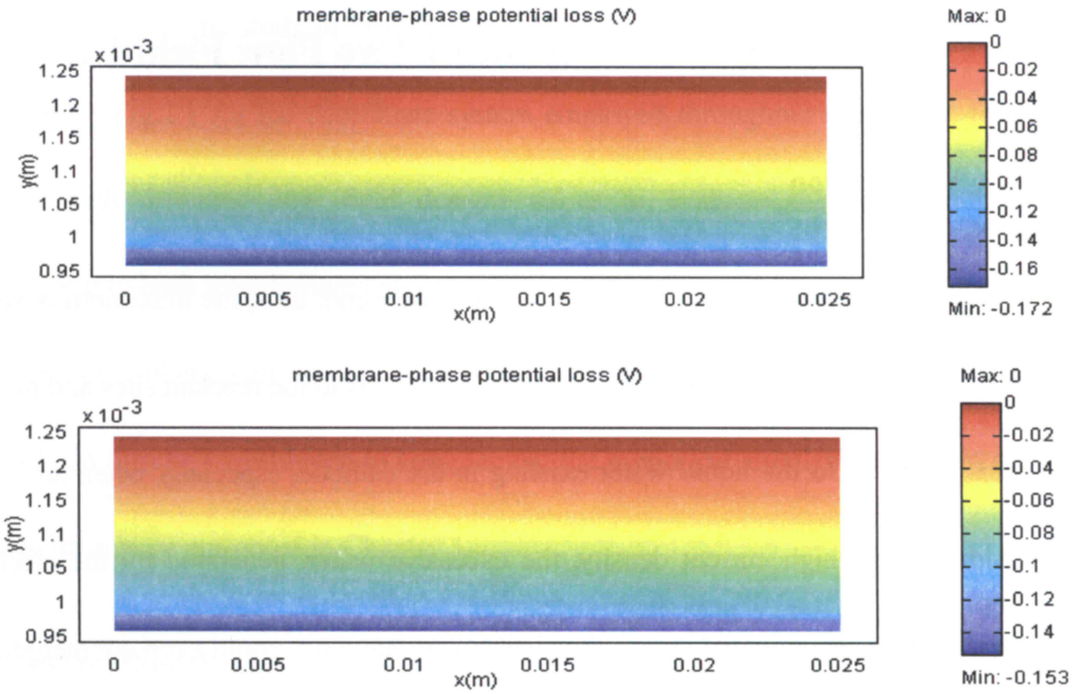

Figure 3.31 Membrane-phase potential loss for different proton conductivities:

10 S/m (upper) and 14 S/m (lower) at cell voltage 0.6V

Chapter 4. Evaluation of Two Flow Field Designs

4.1. Introduction

In a PEM fuel cell, the limiting current density and, thus, the maximum power are often determined by the mass transport rates of the reactants to the reactant sites and mass transport resistance due to the liquid water existing in the cathode, especially when air is used as an oxidant. At a high current density, the excessive water, generated by the electrochemical reaction and accumulated due to the electro-osmotic drag, could even submerge the catalyst particles, resulting in great reduction of the effective reaction surface. As reported by Yi and Nguyen [38], when a fuel cell accumulates too much water at high current densities, about a third of the electrodes surface area is not utilized.

To solve this problem, new flow field designs have been developed. One of them is called interdigitated flow field, which consists of inlet and outlet dead-end gas channels that force the reactant gases to diffuse through the porous electrodes for exit. This design in effect has converted the transport of reactant/product gases to/from the catalyst layers from a diffusion mechanism to a convection mechanism. Since convection is much faster than diffusion, the reaction rates at the catalyst sites can be significantly enhanced if using the interdigitated flow field design. Furthermore, the shear force of this gas flow helps remove most of the liquid water that is entrapped in the inner layers of the GDL, therefore, significantly reducing the electrode flooding possibility.

The objective of the study in this chapter is to develop a mathematical model in the y-z plane (refer to Fig.2.1 for the coordinate system employed throughout this study) for PEM fuel cells with different flow field designs so as to evaluate the cell performances corresponding to both interdigitated and conventional flow field designs. On the other hand, detailed physical phenomena in the y-z plane for the PEM fuel cell with the conventional flow field can also be investigated to complement the numerical simulations only in the x-y plane that have been presented in Chapter 3.

4.2. Modeling Domain and Geometry

Figure 4.1 depicts the schematic drawings in the y-z plane for two PEM fuel cells with conventional (parallel) and interdigitated flow field designs, respectively. As depicted in Figure 4.1(a), in the cathodic gas channel of a parallel flow field, air flows parallelly towards the GDL. The predominant mechanism of oxygen transport towards the catalyst layer is diffusion as presented in the previous chapter. In the interdigitated flow field shown in Figure 4.1(b), flow channels are dead-ended, forcing the air to flow through the porous GDL. The diffusive mass transport mechanism is now changed to a forced convective mass transport in the interdigitated flow field design.

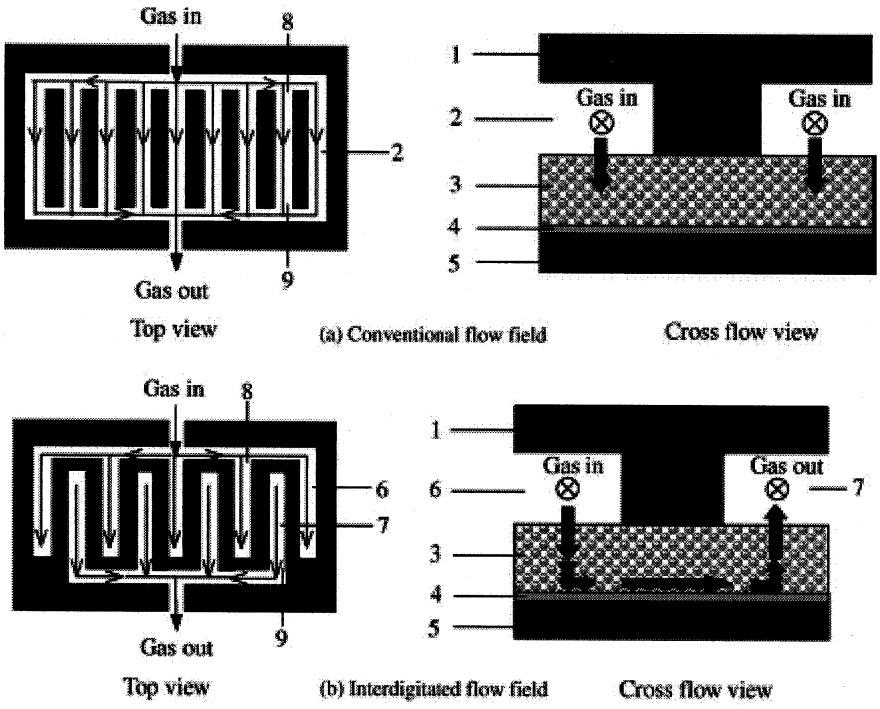

Figure 4.1 Schematic diagram of PEM fuel cell with conventional flow field (a) and interdigitated flow field (b)

In Chapter 2, the two-dimensional model of a PEM fuel cell in the x-y plane is comprised of the anode/cathode gas channels, GDLs, catalyst layers and membrane. In the y-z plane, additional components, the current plate/current collectors, are involved in the two-dimensional model, while the anode/cathode gas channels may be extracted from the computational domains since the cross flow within the channels is insignificant. Hence, in the two-dimensional model of a PEM fuel cell in the y-z plane, there are seven computational subdomains including the anode/cathode current plates, GDLs, catalyst layers,

and membrane, as shown in Figure 4.2.

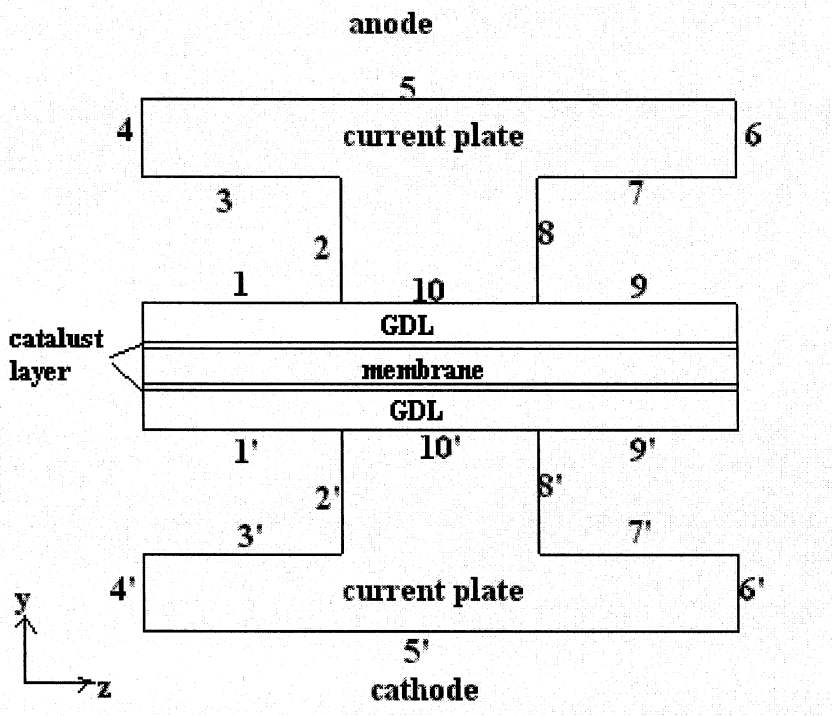

Figure 4.2 Schematic diagram of computation model of a PEM fuel cell in y-z plane

4.3. Governing Equations

In the y-z plane, the governing equations corresponding to different computational domains are mostly similar to those presented in Chapter 2 except for two aspects that are presented here in alternative approaches. First since the gas channels, in which the flow fields were governed by the Navier-Stokes equations, are not involved in the y-z plane model, Darcy's law can be chosen for the GDLs to replace the Navier-Stokes flow modele. Secondly, the solid-phase potential equations accounting for the electron transport in the current plates

have to be added:

$$\vec{\nabla}\cdot(-\sigma^{e}_{plate}\vec{\nabla}\phi_s)=0 \tag{4.1}$$

where σ^{e}_{plate} is the electrical conductivity of current plates. In the present model, the value of σ^{e}_{plate} is assumed to be 20000 S/m [27].

4.4. Boundary Conditions

The governing equations are identical for both conventional and interdigitated flow field designs. The difference exists in boundary conditions for the interfaces between the gas channels and the GDLs. Note that the cross section at the inlet, i.e., x = 0, is selected to simulate transport phenomena in the y-z plane of a PEM fuel cell, and all additional boundaries are demonstrated and numbered in Figure 4.2.

4.4.1. Conventional Flow Field Design

Most boundary conditions are the same as described in section 0, except the following:

4.4.1.1 Darcy's Law

As Darcy's law is used within the entire GDL-catalyst layers-membrane domain, the pressure boundary values are prescribed at the operating pressures for the interfaces between the gas channels and GDLs for both anode and cathode sides. That is:

at Boundaries #1,#9: $p = p_a$ (4.2)

at Boundaries #1', #9', $p = p_c$ (4.3)

where p is the local pressure, p_a and p_c are the operating pressures at the anode and cathode sides, respectively.

4.4.1.2 Species Equations

Similar to Darcy's law, for the anodic and cathodic interfaces between the gas channels and GDLs, i.e., boundaries #1,#1', #9, and #9' (refer to Figure 4.2), each of the mass fractions of H_2, O_2 and $(H_2O)_g$ is prescribed using a constant inlet value.

4.4.1.3 Solid-Phase Potential Equation

To account for electron transport in current plates, the value of solid-phase potential along the anode current plate edge, i.e., Boundary #5, is assumed to be 0, while the value of the cell voltage is prescribed along the cathode current plate edge, i.e., Boundary #5'. Homogeneous *Neumann* boundary conditions are applied at other boundaries, i.e., Boundaries #1,#2,#3,#4,#6,#7,#8,#9 and Boundaries #1',#2',#3',#4', #6',#7',#8',#9' to represent that no electron current passes through the boundaries.

4.4.2. Interdigitated Flow Field Design

In contrast with the conventional flow field design, the different boundary conditions for the interdigitated flow field design are stated as follows:

4.4.2.1 Darcy's Law

According to [40], the pressure drops across a 1 mm shoulder of a current plate were measured at 2.4kPa for the anode side and 1.4kPa for the cathode side. These small pressure

drops are attributed to the highly porous structure of the diffusion layer. Therefore, the pressure boundary values at the exits are different from the value at the entrances:

at Boundary #1: $$p = p_a \tag{4.4}$$

at Boundary #9: $$p = p_a - 2.4kPa \tag{4.5}$$

at Boundary #1': $$p = p_c \tag{4.6}$$

at Boundary #9': $$p = p_c - 1.4kPa \tag{4.7}$$

4.4.2.2 Species Equations

Different from the conventional flow field design, the fully developed conditions are applied to the mass fraction at the exit interfaces between the gas channels and GDLs, i.e. the gradient of each species mass fraction is zero along Boundary #9 and #9'. While the inlet values of mass fraction are prescribed at the entrance interfaces, Boundary #1 and #1'.

4.4.2.3 Energy Equation

The different constant temperature values are prescribed at the entrance interfaces between the gas channels and GDLs, i.e. Boundaries #1 and #1'. The homogeneous *Neumann* boundary conditions are applied along the exit interfaces, i.e., Boundaries #9 and #9'.

4.5. Results and Discussions

In accordance with the simulations in the x-y plane, the results presented below are obtained using the parameters and base conditions described in Chapter 2 if not otherwise

specified in the previous section. This will allow for discussions of the numerical results obtained here in the y-z plane in conjunction with those obtained in the x-y plane from the previous chapter.

4.5.1. Flow Structures

Figure 4.3 demonstrates the pressure distribution within the anodic GDL for

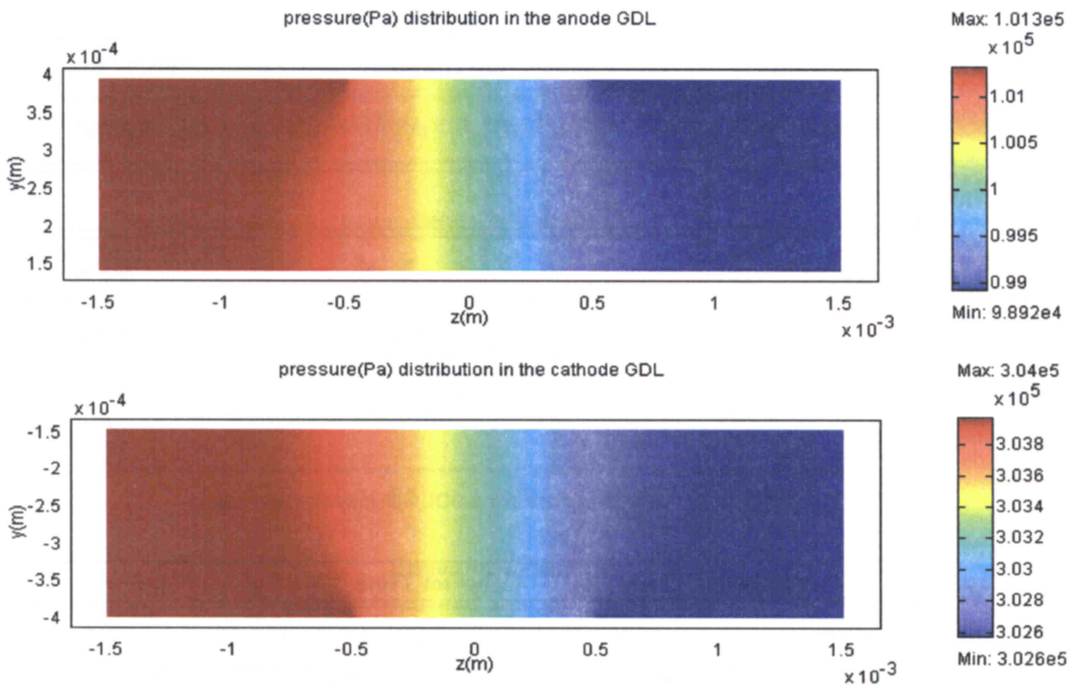

Figure 4.3 Pressure distribution in the y-z plane of the GDL of a PEM fuel cell with interdigitated flow field design (Refer to Figure 4.2 for coordinate system)

interdigitated flow field. It is noticed that the pressure drops much more evidently in the z-direction than in the y-direction.

Figure 4.4 illustrates two-dimensional flow fields in the anode/cathode GDLs in the y-z plane for both conventional and interdigitated flow channel patterns. It can be clearly observed that the magnitude of velocity in the interdigitated flow field is larger than that in the conventional flow field. As supported by the pressure-drop profiles, in the interdigitated flow field, the velocities are highest near the entrance/plate and exit/plate corners because the

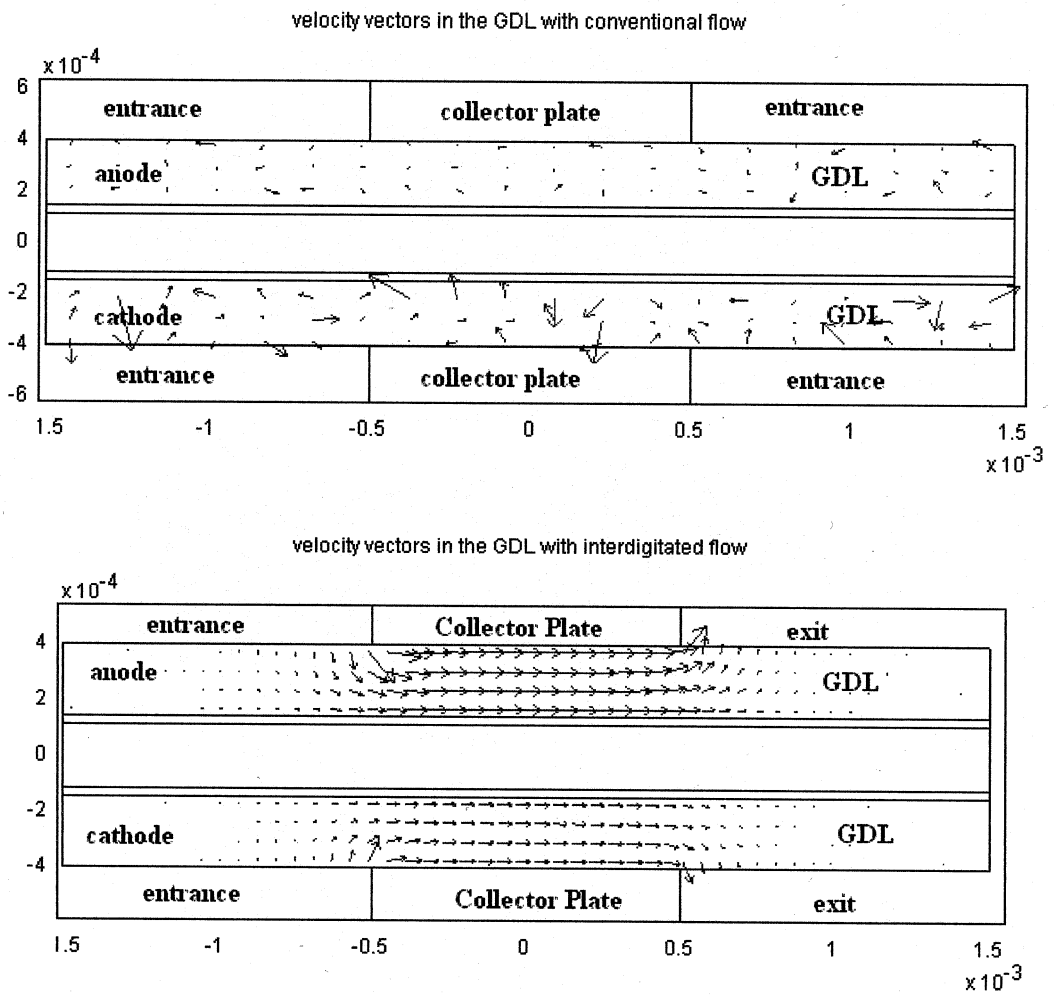

Figure 4.4 Velocity distribution in the GDL for PEM fuel cells with conventional flow field design (top) and interdigitated flow field design (lower) (Refer to Figure 4.2 for coordinate system)

flow is induced by the pressure driving force. The y-direction velocity components are

smaller than those in the z-direction. This forced convection mechanism in the GDLs enhances the mass transport near the reaction surface and thus improves the cell performance as shown in subsequent sections.

4.5.2. Oxygen Distribution

Figure 4.5 shows the oxygen mole fraction contours in the y-z plane for PEM fuel cells with both conventional and interdigitated flow field designs. For the conventional flow field, since diffusion is the only mass transport mechanism, the oxygen decreases linearly in the

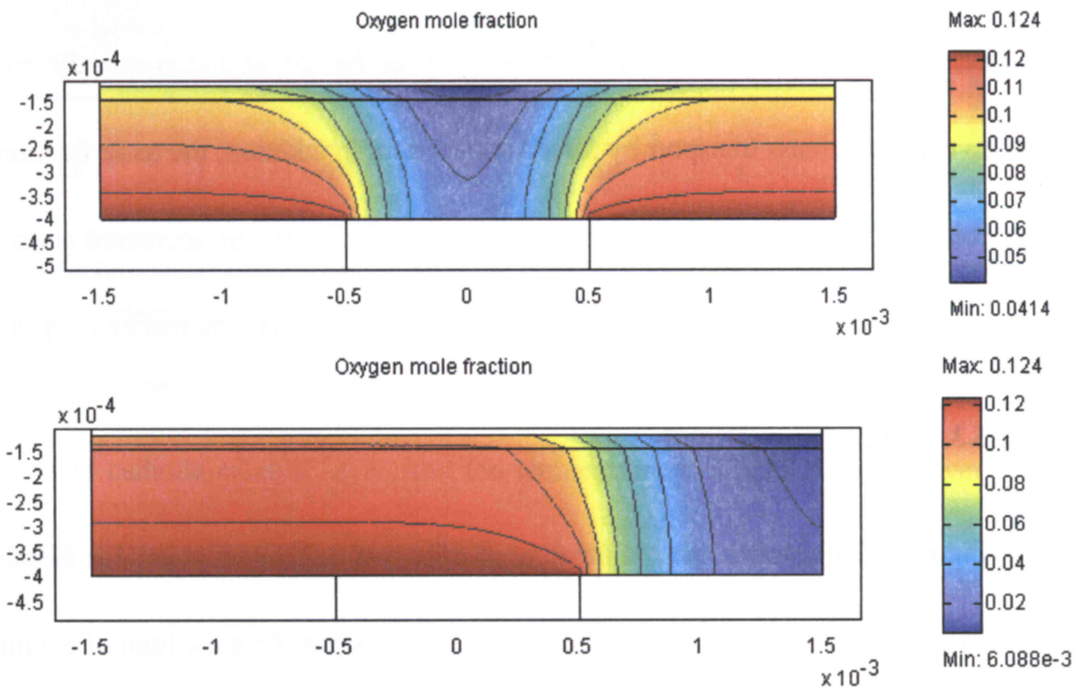

Figure 4.5 Oxygen mole fraction in y-z plane for cell voltage 0.7V: conventional flow field (top) and interdigitated flow field (bottom) (Refer to Figure 4.2 for coordinate system)

direction toward the reaction surface and the profile is symmetrical about its vertical central line due to the symmetrical geometry and flow employed. Furthermore, as expected, due to

the presence of the current plate in the gas channel, there exits a concentration gradient in the z-direction within the GDL and catalyst layer, which could not be observed in the x-y plane simulation results, and low oxygen concentrations can be obtained at the location far from the entrances. In the interdigitated flow, where the air is forced to enter the GDL through Boundary #1' (see Fig. 4.2) and then leave the GDL through Boundary #9' (see Fig. 4.2), the resulting oxygen distribution shown on the bottom of Figure 4.5 is very different from the case of the conventional flow field design shown on the top of Figure 4.5. A higher oxygen concentration is observed near the air entrance; however, the lowest is close to the dead end. Hence, the oxygen mole fraction becomes larger in the region underneath the current plate due to enhanced mass transport by forced convection. In addition, the mole fraction at the air outlet is smaller than in the conventional flow case, indicating an increased consumption of the oxygen due to improvements in the oxygen distribution over the reacting region.

4.5.3. Temperature Distribution

Figure 4.6 illustrates the temperature distribution in the y-z plane for PEM fuel cells with both conventional and interdigitated flow field designs. As a medium of cooling, current plates make the temperature gradient along the z-direction, which can not be observed in the x-y plane simulation results. Also, the peaks of temperature are observed within the cathode catalyst layer. It can be clearly seen that the temperature distribution in the conventional flow flied design is symmetric about its vertical central line due to the symmetry of flow field. For

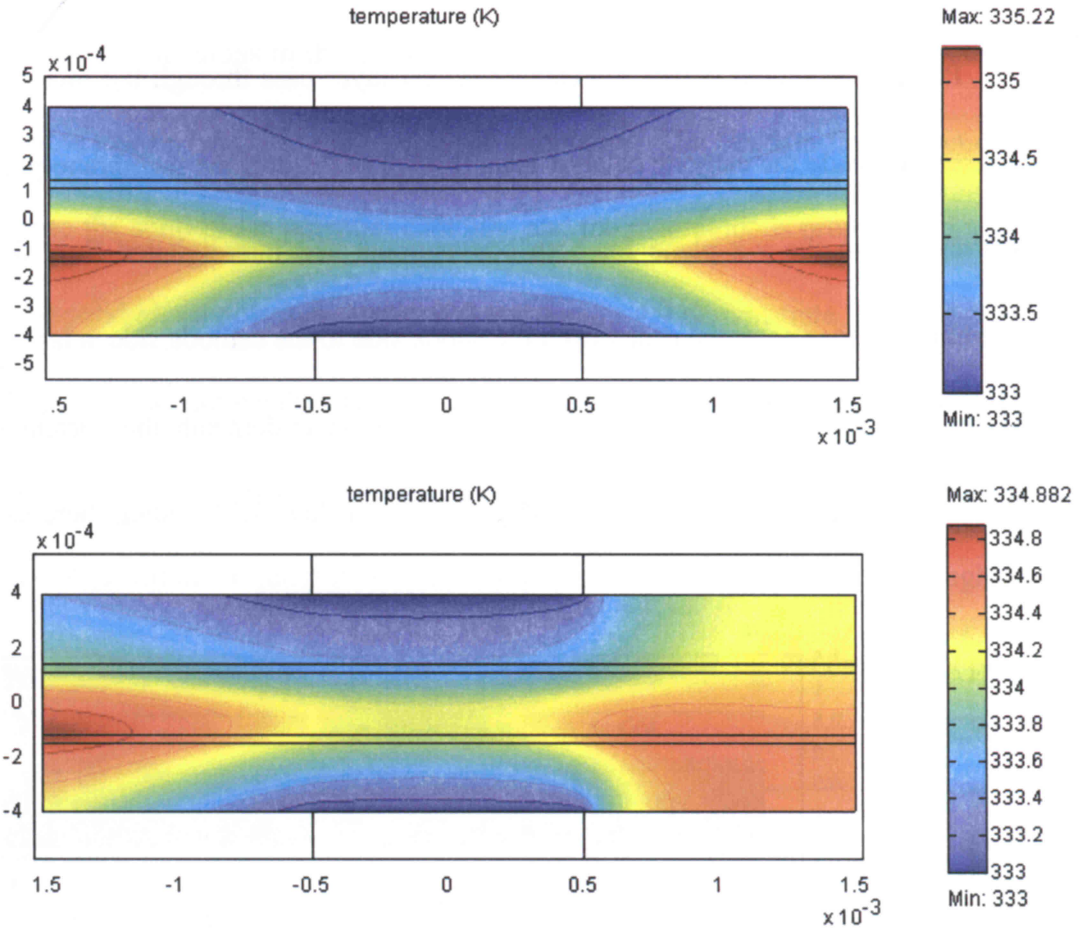

Figure 4.6 Temperature distribution in y-z plane for cell voltage 0.7V: conventional flow field (top) and interdigitated flow field (bottom) (Refer to Figure 4.2 for coordinate system)

the interdigitated flow field design, the highest temperature is asymmetrically obtained only in the inlet-side cathode catalyst layer, and the temperature in the GDLs is not very low because the forced convection helps heat transfer in the GDLs.

4.5.4. Potential Distribution

Protons generated within the anode catalyst layer pass through the membrane and are consumed inside the cathode catalyst layer. Figure 4.7 shows the membrane-phase potential distribution in the y-z plane for both conventional and interdigitated flow fields. As the membrane-phase potential drops from the anode side to the cathode side, a larger gradient of membrane-phase potential can be seen in the region underneath the current plate in the conventional flow field design. For the interdigitated flow field design, there exists a lower

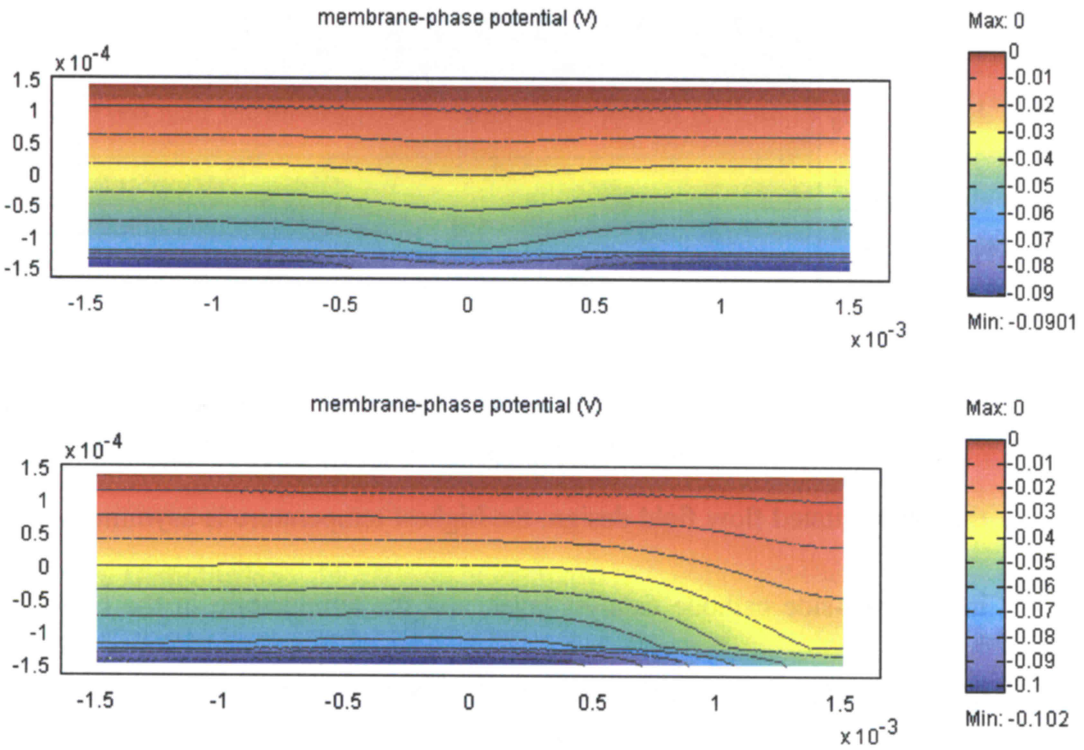

Figure 4.7 Membrane-phase potential within MEA for cell voltage 0.7V: conventional flow field (top) and interdigitated flow field (bottom) (Refer to Figure 4.2 for coordinate system)

membrane-phase potential loss near the outlet region due to weak electrochemical reaction on the site.

Unlike the 2D simulations in the x-y plane, the solid-phase potential directly related to the electron flow can be detailed in the y-z plane simulation. The electron flow direction is perpendicular to the solid-phase potential contours, and the magnitude is proportional to the gradient of the solid-phase potential. Figure 4.8 and Figure 4.9 demonstrate the solid-phase potential distribution within catalyst layer, GDL, and current plate across the y-z plane for the conventional and interdigitated flow field designs, respectively. At the anode side (tops), electrons generated within the catalyst layer pass through GDL, and are collected through the current plate. At the cathode side (bottoms), electrons enter the cathode via the current plate,

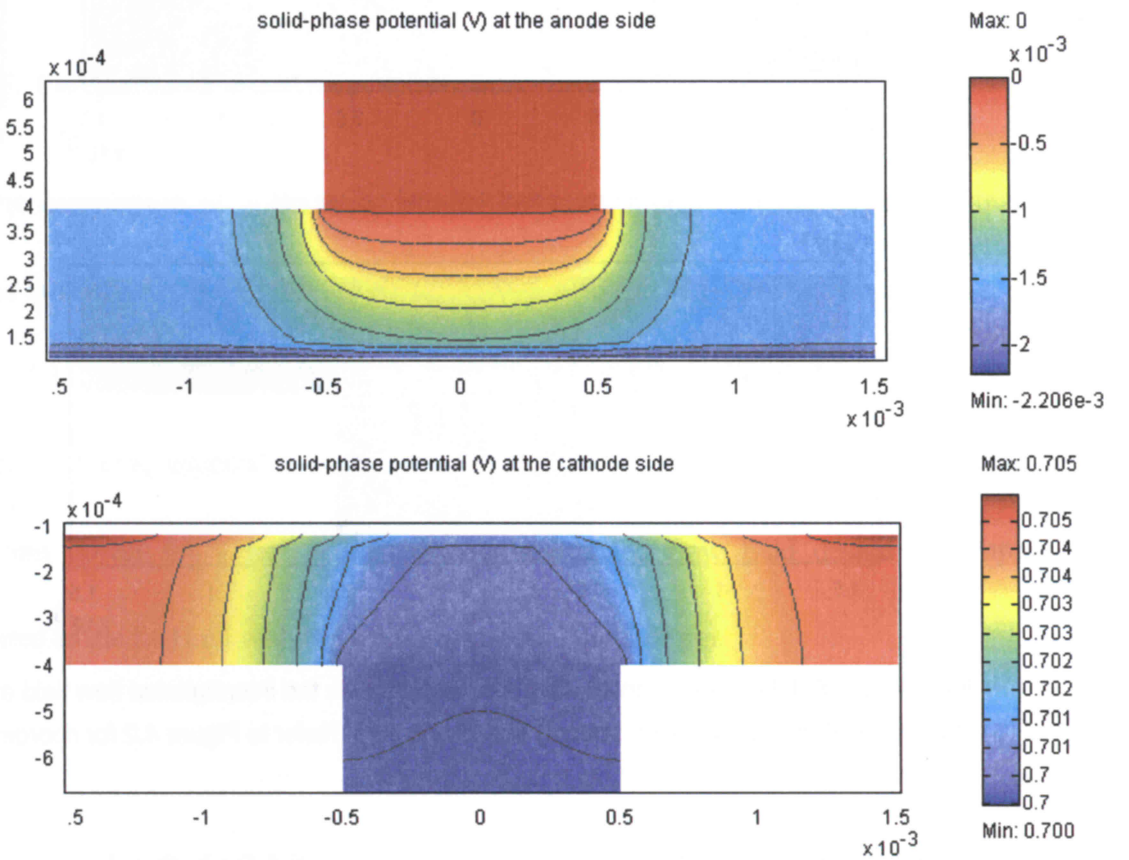

Figure 4.8 Solid-phase potential within the fuel cell with the conventional flow field at cell voltage 0.7V, (top) at anode side and (bottom) at cathode side (Refer to Figure 4.2 for coordinate system)

and are consumed within the catalyst layer by electrochemical reaction.

In general, at the anode side the solid-phase potential drops from the plate to the GDL (see the top of Fig. 4.8 and Fig. 4.9), while at the cathode side from the plate to the GDL an increase of this potential can be clearly noticed (see the bottom of Fig. 4.8 and Fig. 4.9).The

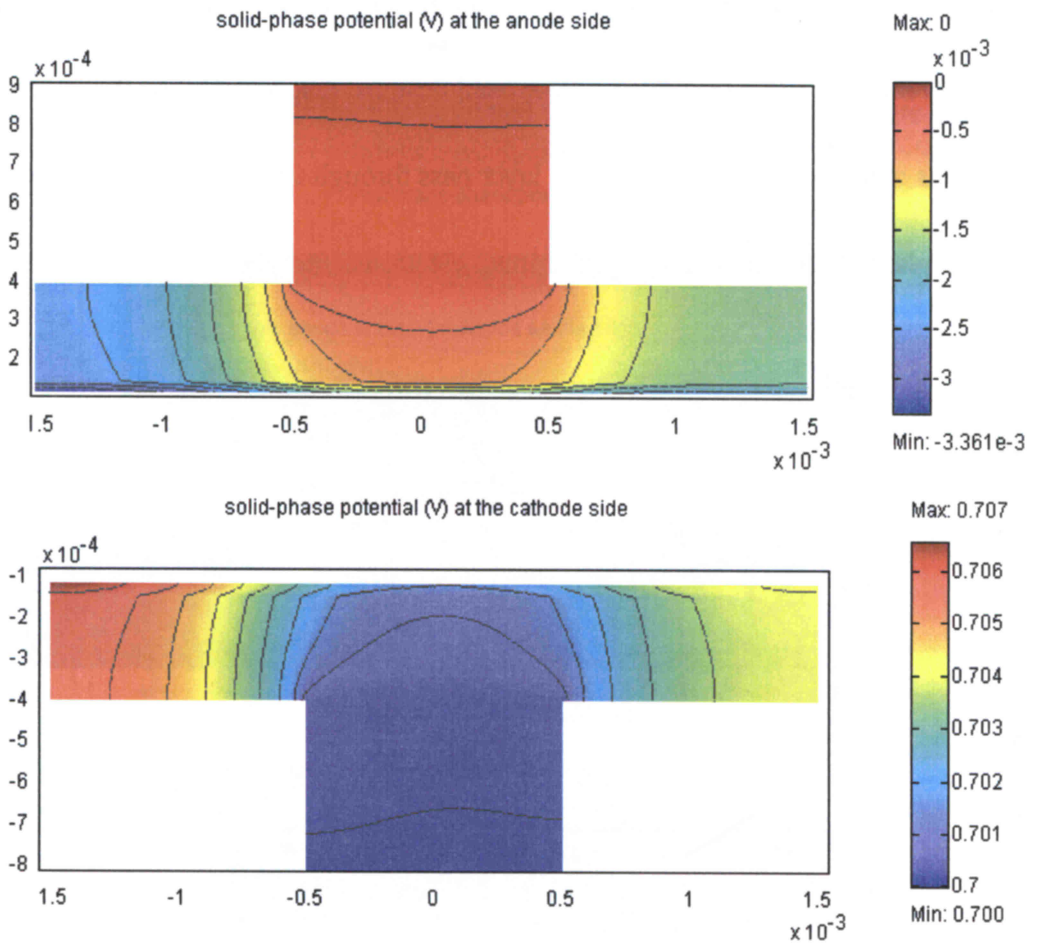

Figure 4.9 Solid-phase potential within the fuel cell with the interdigitated flow field at cell voltage 0.7V, (top) at anode side and (bottom) at cathode side (Refer to Figure 4.2 for coordinate system)

pattern of the change in solid-phase potential appears radial for both sides, which indicates the direction of the electron flow. These observations reveal that, on the anode side, the

electron current starts from the anode catalyst layer; gathers towards the anode current collector, passes through an external circuit to the cathode, gathers again in the cathode current plate, then heads for the cathode catalyst layer and gets consumed in the electrochemical reaction. In the conventional flow field design, the symmetry about its vertical central line can be easily seen in the solid-phase potential distribution, i.e., electron flow in symmetrical path. For the interdigitated flow field, higher solid-phase potential losses and more contours are observed near the inlet region, which implies that there exist stronger electron flows and electrochemical reaction in this region.

4.5.5. Cell performance

The comparison of polarization curves for conventional and interdigitated flow field designs is illustrated in Figure 4.10. The corresponding power density curves are shown in Figure 4.11. It is obvious that the interdigitated flow field design outperforms the conventional one, especially at high current densities. The limiting current density and maximum power for a fuel cell with an interdigitated flow field design are improved compared to the fuel cell with the conventional flow field design.

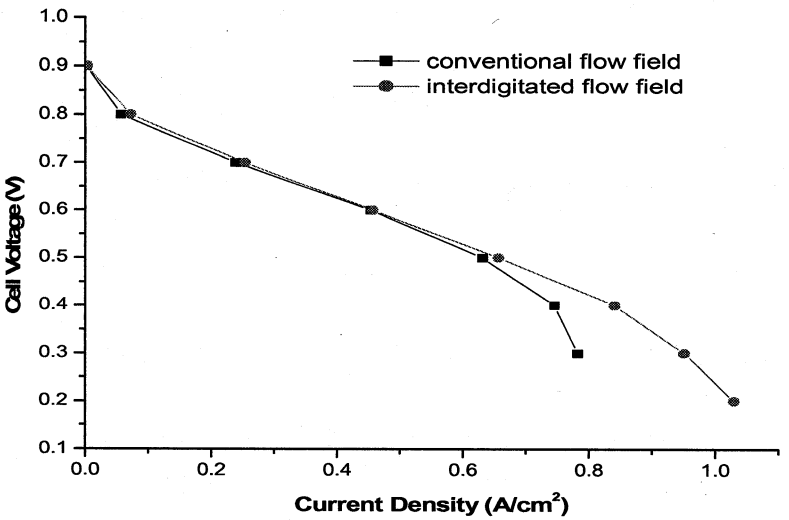

Figure 4.10 Comparison of performance of fuel cell with conventional and interdigitated flow field designs

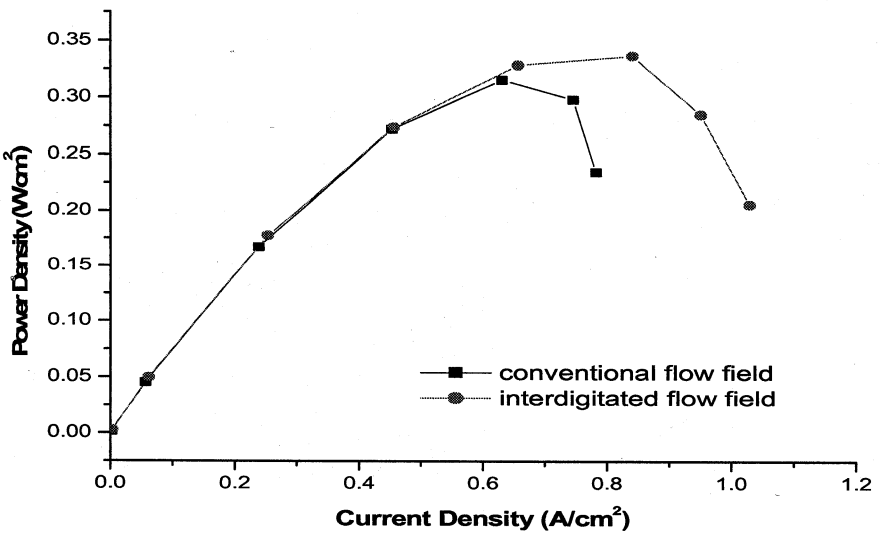

Figure 4.11 Power density curves of fuel cells with conventional and interdigitated flow field designs

As mentioned before, a higher rate of oxygen transport is required to produce high current densities, which can not be fulfilled by the conventional flow field design due to diffusion limitations. To demonstrate the limitation of mass transport, Figure 4.12 shows

oxygen mole fraction distribution inside the cathode catalyst layer at low cell voltage 0.3V, corresponding to a high current density. In the conventional flow field, the transport of oxygen to the reactive sites in the porous GDL is totally achieved by diffusion and the maximum oxygen mole fraction inside the cathode catalyst layer is 0.0245. However, by switching from a diffusion-driven to a convection-and-diffusion-driven mass transport process, the interdigitated flow field can provide a higher rate of oxygen transport and, thus further enhance the cathodic electrochemical reaction rate. It is noticed that more oxygen reaches the cathode catalyst layer as the maximum oxygen mole fraction inside the reactive sites is 0.0454 for the interdigitated flow field design.

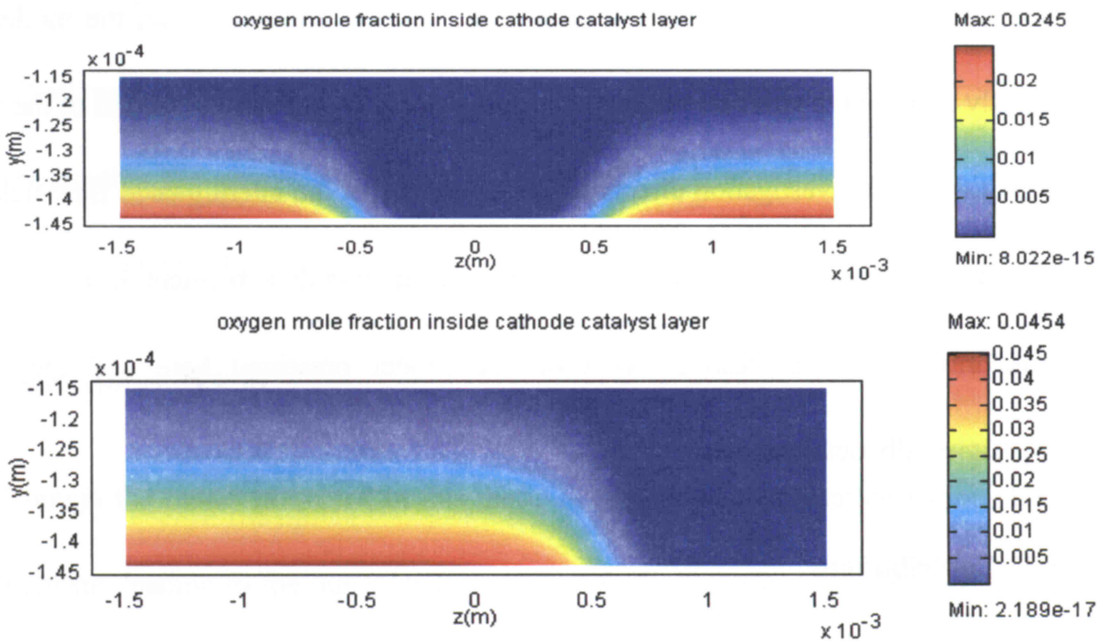

Figure 4.12 Oxygen mole fraction distribution inside cathode catalyst layer at cell voltage 0.3V for conventional (top) and intertditated (bottom) flow field designs

Chapter 5. Conclusions and Outlook

5.1. Conclusions

A two-dimensional non-isothermal model for PEM fuel cells with both conventional and interdigitated flow field design has been developed. Utilizing the CFD methods, the simulation based on this model provides valuable information about the transport phenomena inside the PEM fuel cell such as the flow field, reactant gases distribution, temperature distribution, water content distribution, as well as the membrane-phase and solid-phase potential distributions. A parametric study is also performed that reveals the effect of various operation and property parameters on the fuel cell performance. Also, the model can be slightly modified to simulate various transport process within a cross section of the fuel cell. Along this new investigation direction, the superiority of the interdigitated flow field design is demonstrated over the conventional one. Good overall agreement is achieved when comparing numerical results based on the model presented here and the available experimentally obtained data.

5.2. Contributions

The key contributions in this study are summarized below

i. Improving a single-phase non-isothermal two-dimensional PEM fuel cell model. The model that has been described in Chapter 2 was based on the work by Dr. J. Cao and Dr.

N. Djilali [28]. During this thesis work, this model has been refined by:

- Treating the catalyst layers as independent computation domains instead of nil thickness interfaces;
- Incorporating the electrochemical reaction kinetics within the catalyst layers in finite thickness into the fuel cell model;
- Adding the solid-phase potential equations for electron transport in the bipolar plates, GDLs, and catalyst layers;
- Accounting for the electronic resistant in the GDLs and bipolar plates.

ii. Implementing the voltage-to-current algorithm. This approach is capable of predicting the accurate current density through the coupling of varying activation overpotential and local reactant concentrations.

iii. Evaluating the superiority of the PEM fuel cells with interdigitated flow field design over the conventional (parallel) one.

5.3. Recommendations

Though the model presented in this thesis is capable of investigating various transport phenomena, leading to the numerically predicted fuel cell performance in good agreement with experimental results, some extensions of this thesis work are recommended in order to enhance the present model towards a more accurate and complete representation of all major physically realistic phenomena in PEM fuel cells.

i. Expand the present two-dimensional model to a comprehensive three-dimensional model that can account for 3D effects by using a similar approach to the one presented in this work.

ii. Develop a two-phase model to investigate the mechanism of phase change in the porous layers and possible effects of the phase change on the porosity of the GDL. At higher current densities, liquid water as the by-product of the electrochemical reaction must be transported through GDL to the channel outlet; some water may plug the pores and thus decrease the porosity of the GDL during its transport through the GDL, altering the performance of the cell. These phenomena cannot be revealed through numerical simulation unless a phase change model is well established and successfully incorporated into the PEM fuel cell model.

iii. Develop a dynamic model. In the present work, the steady-state behavior of the fuel cell is captured by estimating the equilibrium voltage for a particular set of operating conditions. In practical applications of a fuel cell for a dynamic system, such as a power system, the investigation of crucial transient dynamic mechanisms will rely on a dynamic model.

iv. Explore some strategies to predict the performance of an industrial-scale fuel cell stack.

References

1. P.D. Beattie, F.P. Orfino, V.I. Basura, K. Zychowska, J.F. Ding, C. Chuy, J. Schmeisser and S. Holdcroft. "Ionic conductivity of proton exchange membranes", *J. Electroanalytical Chemistry*, 503:45-56, 2001.
2. N. Sammes Editor. *Fuel Cell Technology*. Springer Press, 2006.
3. M. Eikerling, and A.A. Kornyshev. "Proton Transfer in a Single Pore of a Polymer Electrolyte Membrane", *J. Electroanalytical Chemistry*, 502: 1-14, 2001.
4. T. D. Gierke, G. E. Munn, and F. C. Wilson. "The Morphology in Nafion Perluorinated Membrane Products, as Determined by Wide- and Small-Angle X-Ray Studies", *J. Polymer Science*, Polymer physics edition, 19:1687-1704, 1981.
5. M. Mehta, and J.S. Cooper. "Review and Analysis of PEM Fuel Cell Design and Manufacturing", *J. of Power Sources,* 114: 32-53, 2003.
6. E. A. Ticianelli, J. G. Beery, and S. Srinivasan. "Dependence of Performance of Solid Polymer Electrolyte Fuel Cells with Low Platinum Loading on Morphologic Characteristics of the Electrodes", *J. Electroanal. Chem.*, 251:275-295, 1988.
7. M. Mehta, J. S. Cooper, "Review and Analysis of PEM Fuel Cell Design and Manufacturing", *J. Power Sources*, 114:32-53, 2003.
8. A. Hermann, T. Chaudhuri and P. Spagnol. "Bipolar Plates for PEM Fuel Cells: A Review", *J. of Hydrogen Energy,* 30: 1297-1302, 2005.
9. A. Parthasarathy, S. Srinivasan, A. J. Appleby, and C. R. Martin. "Pressure Dependence of the Oxygen Reduction Reaction at the Platinum Microelectrode/Nafion Interface: Electrode Kinetics and Mass Transport", *J. Electrochem. Soc.*, 139(10):2856-2862, 1992.
10. D. M. Bernadi and M. W. Verbrugge. "A Mathematical Model of the Solid Polymer Electrolyte Fuel Cell". *J. Electrochem. Soc.*, 139(9):2477-2491, 1992.
11. D. M. Bernardi and M. W. Verbrugge. "Mathematical Model of a Gas Diffusion Electrode Bonded to a Polymer Electrolyte". *AIChE J.*, 37(8):1151-1162, 1991.
12. T. E. Springer, T. A. Zawordzinski, and S. Gottesfeld, "Polymer Electrolyte Fuel Cell Model", *J. Electrochem. Soc.*, 138(8):2334-2342, 1991.
13. T. F. Fuller, J. Newman, "Water and Thermal Management in Solid Polymer Electrolyte Fuel Cells", *J. Electrochem. Soc.,* 140(5):1218-1225, 1993.
14. T. V. Nguyen, R. E. White, "A Water and Heat Management Modle ofr Proton Exchange Membrane Fuel Cells", *J. Electrochem. Soc.*, 140(8):2178-2186, 1993
15. J. S. Yi, T. V. Nguyen, "An Along-the Channel Model for Proton Exchange Membrane Fuel Cells", *J. Electrochem. Soc.*, 145(4):1149-1159, 1998.
16. J. S. Yi, T. V. Nguyen, "Multicomponent Transport in Porous Electrodes of Proton Exchange Membrane Fuel Cells Using the Interdigitated Gas Distributors", *J.*

Electrochem. Soc., 146(1):38-45, 1999.

17. J.C. Amphlett, R.M. Baumert, R.F. Mann, B.A. Peppley, P.R. Roberge, "Performance Modeling of Ballard Mark IV Fuel Cell", *J. Electorchem. Soc.*, 142(1):1-15, 1995.
18. J.Kim, S.M. Lee, S. Srinivasan, "Modeling of Proton Exchange Membrane Fuel Cell Performance with an Empirical Equation", *J. Electorchem. Soc.*, 142(8):2670-2674, 1995.
19. V. Gurau, H. Liu, and S. Kakac. "Two-Dimensional Model for Proton Exchange Membrane Fuel Cells", *AIChE J*, 44(11):2410-2422, 1998.
20. S. Um, C. Y. Wang, and K. S. Chen, "Computational Fluid Dynamics Modeling of Proton Exchange Membrane Fuel Cells", *J. Electrochem. Soc.*, 147(12):4485-4493, 2000.
21. Z. H. Wang, C. Y. Wang, K. S. Chen, "Two Phase Flow and Transport in the Air Cathode of Proton Exchange Membrane Fuel Cells", *J. Power Sources*, 94(1):40-50, 2001.
22. T. Berning, D. M. Lu, N. Djilali, "Three-Dimensional Computational Analysis of Transport Phenomena in a PEM Fuel Cell", *J. Power Sources*, 106(1-2):284-292, 2002.
23. S. Dutta, S. Shimpalee, J. W. Van zee, "Three-dimensional Numerical Simulation of Straight Channel PEM Fuel Cells", *J. Appl. Electrochem.*, 30:135-146, 2000.
24. S. Dutta, S. Shimpalee, J. W. Van zee, "Numerical Prediction of Mass Exchange between Anode and Cathode Channels in a PEM Fuel Cell", *Int. J. Heat Mass Transfer*, 44:29-40, 2001.
25. S. Um, C.Y. Wang, "Three-Dimensional Analysis of Transport and Electrochemical Reactions in Polymer Electrolyte Fuel Cells", *J. Power Sources,* 125:40-51, 2004.
26. T. Zhou, H. Liu, "A General Three-Dimensional Model for Proton Exchange Membrane Fuel Cells", *Int. J. Transport Phenom.*, 3:177-198, 2001.
27. T. Zhou, and H. Liu, "Effects of the electrical resistance of the GDL in the a PEM fuel cell", *J. Power Sources*, 151(11):A1954-A1960, 2006.
28. J. Cao and N. Djilali, "Numerical Modeling of PEM Fuel Cells Under Partially Hydrated Membrane Conditions", *ASME J. Energy Resources Technology*, 127:26-36, 2005.
29. H. Meng, C. Y. Wang, "Electron Transport in PEMFCs", *J. Electrochem. Soc.*, 151(3):A358-A367, 2004
30. B.R. Sivertsen, N. Djilali, "CFD-based Modeling of Proton Exchange Membrane Fuel Cells", *J. Power Sources*, 141:65-78, 2005
31. T. E. Springer, M. S. Wilson, S. Gottesfeld, "Modeling and Experimental Diagnostics in Polymer Electrolyte Fuel Cells", *J. Electorchem. Soc.*, 140(12):3513-3526, 1993.
32. G. H. Guvelioglu, H. G. Stenger, "Computational Fluid Dynamics Modeling of Polymer Electrolyte Membrane Fuel Cells", *J. Power Sources.* , 147:95-106, 2005.
33. G. Gagan, "Flow and Transport in Porous Formation", *Springer-Verlag, Berling,* 1989.
34. H. Ju, and C.Y. Wang, "Experimental Validation of a PEM Fuel Cell Model by Current Distribution Data", *J. Electrochem. Soc.*, 151(11):A1954-A1960, 2004.

35. F. Barbir, "PEM Fuel Cells: Theory and Practice", *ELSEVIER ACADEMIC, ,* 2005.
36. L. Wang, A. Husar, T. Zhou, H.Liu. "A Parametric Study of PEM Fuel Cell Performances". International Journal of Hydrogen Energy, 28:1263-1272, 2003.
37. L. You, H, Liu, "A Parametric Study of the Cathode Catalyst Layer of PEM Fuel Cells Using a Pseudo-homogeneous Model". International Journal of Hydrogen Energy, 26:990-999, 2001.
38. J.S. Yi and T.V. Nguyen, "Proton Conducting Membrane Fuel Cells I". The Electrochemical Society Proceeding Series, 23: 66-75, 1995.
39. T.E. Springer, T.A. Zawodzinski and S. Gottesfeld, "Characterization of Polymer Electrolyte Fuel Cells Using AC Impedance Spectroscopy". Journal of Electrochemical Society 143(2): 587-599, 1996.
40. T.V. Nguyen, "A Gas Distributor Design for Proton-exchange-membrane Fuel Cells". Journal of Electrochemical Society 143(5): L103-5, 1996.
41. W. K. Lee, S. Shimpalee, J. W. Van Zee, "Verifying Predictions of Water and Current Distributions in a Serpentine Flow Field PEMFC", *J. Electrochem. Soc.*, 150(3):A341-A348, 2003.
42. S. Mazumder, J. V. Cole, "Rigorous Three Dimensional Mathematical Modeling of Proton Exchange Membrane Fuel Cells. Part 1: Model Predictions without Liquid Water Transport", *J. Electrochem. Soc.*, 150:A1503-A1509, 2003.
43. .W. He, J. S. Yi, T. V. Nguyen, "Two-Phase Flow Model of the Cathode of PEM Fuel Cells Using Interdigitated Flow Fields", *AIChE J.*, 46(10): 2053-2064, 2000.
44. D. Natarajan, T. V. Nguyen, "A Two-Dimensional, Two-Phase, Multi-Component, Transient Model for the Cathode of a PEM Fuel Cell Using Conventional Gas Distributors", *J. Electrochem. Soc.*, 148:1324-1335, 2001.
45. D. Natarajan, T. V. Nguyen, "Three-Dimensional Effects of Liquid Water Flooding in the Cathode of PEM Fuel Cell Using Conventional Gas Distributors," *J. Power Sources*, 115:66-80, 2003.
46. L. You, H. Liu, "A Two-Phase Flow and Transport Model for the Cathode of PEM Fuel Cells", *Int. J. Heat Mass Transfer*, 45(11):2277-2287, 2002.
47. S. Mazumder, J. V. Cole, "Rigorous Three Dimensional Mathematical Modeling of Proton Exchange Membrane Fuel Cells. Part 2: Model Predictions with Liquid Water Transport", *J. Electrochem. Soc.*, 150:A1510-A1517, 2003.
48. T. Berning, N. Djilali, "A 3D, Multi-Phase, Multicomponent Model of the Cathode and Anode of a PEM Fuel Cell", *J. Electrochem. Soc.*, 150(12):A1598-A1598, 2003.
49. C. Y. Wang, "Fundamental Models for Fuel Cell Engineering", *Chemical Reviews*, 2004, in press.
50. R. B. Bird, W. Steward, and E. N. Lightfood. *Transport Phenomena*. Wiley, New York, 1960.
51. R. E. De La Rue and C. W. Tobias. "On the Conductivity of Dispersions", *J.*

Electrochem. Soc., 106:827-836, 1959.

52. J. S. Newman. *Electrochemical Systems*. Prentice Hall, Englewood Cliffs, New Jersey, 1991.
53. D. Singh, D. M. Lu, and N. Djilali, "A Two-Dimensional Analysis of Mass Transport in Proton Exchange Membrane Fuel Cells", *Inter. J. of Eng. Sci.,* 37:431–452, 1999.
54. M. W. Verbrugge, R. F. Hill, "Ion and Solvent Transport in Ion-Exchange Membranes", *J. Electrochem. Soc.*, 140(5):1218-1225, 1993.
55. Online support of Femlab, COMSOL Inc.
56. E. A. Ticianelli, C. R. Derouin, A. Redondo, and S. Srinivasan. "Methodes to Advance Technology of Proton Exchange Membrane Fuel Cells", *J. Electrochem. Soc.*, 135(9):2209-2214, 1988.
57. P. T. Nguyen, "A Three Dimensional Computational Model of PEM Fuel Cell with Serpentine Gas Channels", Master thesis, University of Victoria, 2003.
58. A. Parthasarathy, B. Dave, S. Srinivasan, J. A. Appleby, and C. R. Martin. "The Platinum Microelectrode/Nafion Interface: An Electrochemical Impedance Spectroscopic Analysis of Oxygen Reduction Kinetics and Nafion Characteristics". *J. Electrochem. Soc.*, 139(6):1634-1641, 1992.
59. M. J. Lampinen and M. Fomino. "Analysis of Free Energy and Entropy Changes for Half-Cell Reactions", *J. Electrochem. Soc.*, 140(12):3537-3546, 1993.
60. J. L. Fales and N. E. Vandeborough, "The Influence of Ionomer Channel Geometry on Ionomer Transport", *Electorchem. Soc. Proceedings*, 86(13):179-191, 1986.
61. F. M. White, *Fluid Mechanics* (3rd edition), McGraw Hill, New Jersey, 1994.